BRILLOUIN SPECTROSCOPIC STUDIES OF THE ELASTIC PROPERTIES OF ICE UP TO 10 KBAR

ROBERT E. GAGNON

NOTICE

The quality of this microform is heavily dependent upon the quality of the original thesis submitted for microfilming. Every effort has been made to ensure the highest quality of reproduction possible.

If pages are missing, contact the university which granted the degree.

Some pages may have indistinct print especially if the original pages were typed with a poor typewriter ribbon or if the university sent us an inferior photocopy.

Previously copyrighted materials (journal articles, published tests, etc.) are not filmed.

Reproduction in full or in part of this microform is governed by the Canadian Copyright Act, R.S.C. 1970, c. C-30.

AVIS

La qualité de cette microforme dépend grandement de la qualité de la thèse soumise au microfilmage. Nous avons tout fait pour assurer une qualité supérieure de reproduction.

S'il manque des pages, veuillez communiquer avec l'université qui a conféré le grade.

La qualité d'impression de certaines pages peut laisser à désirer, surtout si les pages originales ont été dactylographiées à l'aide d'un ruban usé ou si l'université nous a fait parvenir une photocopie de qualité inférieure.

Les documents qui font déjà l'objet d'un droit d'auteur (articles de revue, tests publiés, etc.) ne sont pas microfilmés.

La reproduction, même partielle, de cette microforme est soumise à la Loi canadienne sur le droit d'auteur, SRC 1970, c. C-30.

BRILLOUIN SPECTROSCOPIC STUDIES OF THE ELASTIC PROPERTIES OF ICE UP TO 10 KBAR

by

© Robert E. Gagnon, B.Sc. (Hons.), M.Sc.

A Thesis submitted in partial fulfillment
of the requirements for the degree of
Doctor of Philosophy

Department of Physics
Memorial University of Newfoundland

November 1986

St. John's Newfoundland

ISBN 0-315-39463-3

ABSTRACT

The technique of high resolution Brillouin spectroscopy has been used to determine accurately, and for the first time, the hydrostatic pressure dependence of the elastic constants of ice Ih in the full pressure range of phase stability and metastability, 0 - 2.8 kbar, at -35.5°C. The temperature dependence of the elastic constants has also been determined in the temperature range -4°C to -35°C.

A thermoelectrically cooled cryostat and a 10 kbar optical cell were constructed to house rotatable cylindrical specimens. Samples were prepared from large single crystals of Mendenhall glacial ice. Prior to the laser scattering experiments, the c-axis orientations of the monocrystalline specimens were determined to within 0.5° by a unique optical birefringence device.

The elastic constants were determined by analyzing the Brillouin frequency shifts as a function of crystal orientation. The absolute zero pressure values agreed to about 1% with other Brillouin spectroscopic studies of ice Ih. The percentage changes in the elastic constants c_{11}, c_{12}, c_{13}, c_{33}, c_{44} and bulk modulus, over the full pressure range, are 3.0, 7.4, 8.0, 2.8, -1.5 and 5.1 percent per kbar respectively. The negative pressure dependence of c_{44}, which is softening of the shear modes, indicates decreasing crystal stability as the phase transition to ice III (at ~3 kbar) is approached.

Longitudinal and transverse acoustic velocities have also been determined for isotropic, finely polycrystalline, aggregates of four

high pressure ice phases. The bulk moduli (±5%) derived from the velocity data, for ice II, III, V and VI are 138.9, 98.7, 141.9 and 181.4 kbar respectively.

To obtain ice densities, so that refractive indices could be calculated for use in the Brillouin equation, a technique has been developed whereby the variation of sample volume with pressure has been measured directly in the pressure range 0 - 10 kbar. Isothermal bulk moduli derived from this data agree to within 5% with the adiabatic values calculated from the velocity data.

A scheme has been worked out to classify the various ice phases, based on knowledge of the hydrogen bonds, which can qualitatively explain the observed velocity data and can furthermore be used to predict approximate velocities for phases for which no velocity data presently exist.

There is excellent agreement between the present longitudinal velocity results and other published data. There are discrepancies between previous and present shear wave velocity results, however. The present values appear to be more accurate, at the pressures of the midpoints of the phases at least, as indicated by the consistency of the values for the bulk moduli derived using the present density data and the present velocity data.

ACKNOWLEDGEMENTS

I am indebted to several individuals and institutions whose assistance made the completion of this work possible.

First and foremost I must gratefully acknowledge the wise supervision of this research by my supervisors, Dr. H. Kiefte and Dr. M.J. Clouter, which assured a steady and well directed path throughout its whole course.

I wish to thank Dr. E. Whalley, at NRC in Ottawa, whose collaboration on the construction of the high pressure apparatus and keen interest during the experiments were invaluable. Also, thanks go to Aurèle Lavergne for useful suggestions related to the installation of the high pressure cell and instructions on the use of the various high pressure components. His significant contributions during the design and construction stages of the high pressure cell were also appreciated. I am also grateful to Dr. D. Klug, at NRC, for his time and assistance during my visit to his lab.

I would like to express my appreciation to Terry White and Mike Ryan for their fine workmanship on various components of the apparatus. Also, thanks go to Roger Guest for the careful drafting of many figures.

I am grateful to Dr. C.W. Cho for his translation of parts of a Japanese paper.

The provision of large single crystals of Mendenhall glacial ice by the U.S. Army Cold Regions Research and Engineering Laboratory,

Hanover, New Hampshire, is sincerely appreciated.

The financial assistance, in the form of a scholarship and bursary, from the Government of Newfoundland and Memorial University are gratefully acknowledged.

Finally I am indebted to my wife, Elizabeth, without whose practical assistance I would not have been able to present the results of this work at the VIIth International Symposium on the Physics and Chemistry of Ice held in Grenoble, France, in Sept. 1986.

TABLE OF CONTENTS

CHAPTER Page

LIST OF TABLES

LIST OF FIGURES

CHAPTER 1

LITERATURE REVIEW AND INTRODUCTION TO THE BRILLOUIN TECHNIQUE

1.1 The Importance of Ice Studies

Water, a substance which has several hydrogen-bonded crystalline polymorphs (at least 13), is fascinatingly complex. The hydrogen bond is essentially electrostatic and is comprised, in solid water and other substances, of a hydrogen atom situated between two electronegative atoms. In the case of water the electronegative atom is oxygen, while other examples include nitrogen and fluorine. The pervasive role which hydrogen bonding plays in our physical surroundings ranks this interaction as one of the most important of all molecular interactions. The action of glues and adhesives, the structure of proteins, and the adhesion of dirt to human skin are primarily the result of hydrogen bonding. Our own bodies are constructed of mainly hydrogen-bonded materials. Much effort has therefore gone into modelling this interaction potential.

Since the most complete hydrogen-bonded materials are probably the various solid crystalline phases of water, these substances are ideally suited to studies which provide information which can be used to refine hydrogen-binding models of the water-water interaction. A number of these models have been proposed and studied.[1-28] Theoretical investigations, some involving computer simulations, of phase transitions in ice have also been conducted.[29-36] Experiments on the solid phases of water which determine atomic positions and angular

relationships, characteristic lattice mode spectra, the pressure-temperature conditions and modes of phase transitions and elastic behaviour[37-39], all provide useful data to stringently test models of the water-water potential, much more so than the relatively imprecise method of requiring that a potential predict radial distributions for the liquid.

In the engineering context, the study of the elastic properties of ice and their pressure dependence is important for understanding the mechanics of ice impacts, e.g. icebergs with offshore structures, for analysing the dynamics of glaciers, for interpreting seismic probes of the interiors of glaciers[40] and ice caps, and for understanding the role of polymorphism in the demolition of ice masses by explosives.

In recent years the discovery of extraterrestrial H_2O, which exists in low temperature and/or high pressure environments elsewhere in the solar system, has given added importance to the study of ice. Mishima et al.[41] used data on the infrared absorptivity of sound waves in ice Ih, coupled with the measured thermal component of brightness, to estimate the thickness of the icy rings of Saturn. Whalley and McLaurin[42] have suggested that cubic crystals of various substances, including water ice, present in the atmospheres of planets and satellites, could be detected by their characteristic refraction halos.

Comet nuclei are known to contain large amounts of water ice (Whipple[43]). Klinger[44] and Patashnick et al.[45] proposed that a phase transition from amorphous to cubic ice, induced by solar heating of comet nuclei, may explain the asymmetry in gas production with respect to perihelion exhibited by some comets. As an aside, Whipple's description of comets as 'dirty snowballs' might be refined a little by

referring to them as dirty icebergs instead, given the results of recent encounters of various space probes with Halley's Comet, which indicate that some comet nuclei, at least, are large irregular shaped chunks of dirty ice.

Many planetary satellites throughout the solar system consist to a substantial degree of water and other ices (>40%, Consolmagno[46]), such as CO, CH_4, etc. Hepburn[47] proposed that the six inner satellites of Saturn were largely made up of water ice. This conclusion was based on the low densities which he had estimated for these bodies. Recent infrared photometry and infrared reflection spectroscopy have been used by Clark and Owensby[48], Morrison et al.[49] and Fink et al.[50] to identify ice on satellites of Jupiter and Saturn. Models of the internal structure and evolution of these bodies (Squyres[51], Consolmagno and Lewis[52], Reynolds and Cassen[53], Parmentier and Head[54,55]) require P-V-T data and information on the elastic properties of the polymorphs of ice. Also, the elastic properties have an important application related to the tidal dissipation of energy, which determines the rate of orbital evolution, of these satellites (Cassen et al.[56,57], Yoder[58] and Peale et al.[59]). A critical parameter in the calculation of the tidal energy dissipation is the rigidity of the icy part of the moon in question.

Gaffney and Matson[60], and Gaffney[61] have determined that it is likely that phase transformations produce important amounts of high pressure ices when objects impact the surfaces of cold icy satellites, such as those of Saturn and more remote planets. Poirier[62] has reviewed the rheology of ices and how they influence the tectonic behaviour of icy satellites.

The processes behind the considerable surface and internal geological evolution which these moons experience can be understood only when the physical properties of ice at low temperature and/or high pressure are known. The not unlikely prospect of a space probe mission to land on one of these icy satellites, or a comet, some time in the near future lends particular importance to the pursuit of such information.

For an excellent review of the work on extraterrestrial ice see Klinger.[63]

1.2 The Discovery of the Polymorphs of Ice and Their Crystal Structures

The water substance, though chemically quite simple, has many solid phases. Structurally it is perhaps one of the most complex crystalline compounds. The free water molecule consists of two hydrogen atoms and one oxygen atom which form a triangular shaped molecule with an H-O-H angle of ~105° and O-H bond length of .97Å. Distortions of the bond angle and length account for the variety of crystalline water structures. In the solid form each molecule is hydrogen bonded to four neighbouring molecules in a roughly tetrahedral shape, depending on which polymorph is considered. In ordinary hexagonal ice Ih the shape is nearly exact and the H-O-H bond angle deviates only slightly from its free molecular value because of its proximity to the tetrahedral O-O-O angle of 109.5°. Considerable variation exists for the O-O-O angles in the other phases, from 76° in ice VI (Kamb[64]) to the extraordinarily large value of 143° for ice III (Kamb and Prakash[65]).

The phase diagram for H_2O, Figure 1.1 (Hobbs[66]), and the structures of the various polymorphs have been studied intensively since the turn

Figure 1.1. Phase diagram for the solid phases of water. ——— measured stable lines. — — — measured metastable lines. - - - - extrapolated or estimated stable lines. ····· extrapolated or estimated metastable lines. Hobbs[66] (1974). The thick solid horizontal line corresponds to the temperature (-35.5°C) and range of pressures at which most of the present experiments were performed.

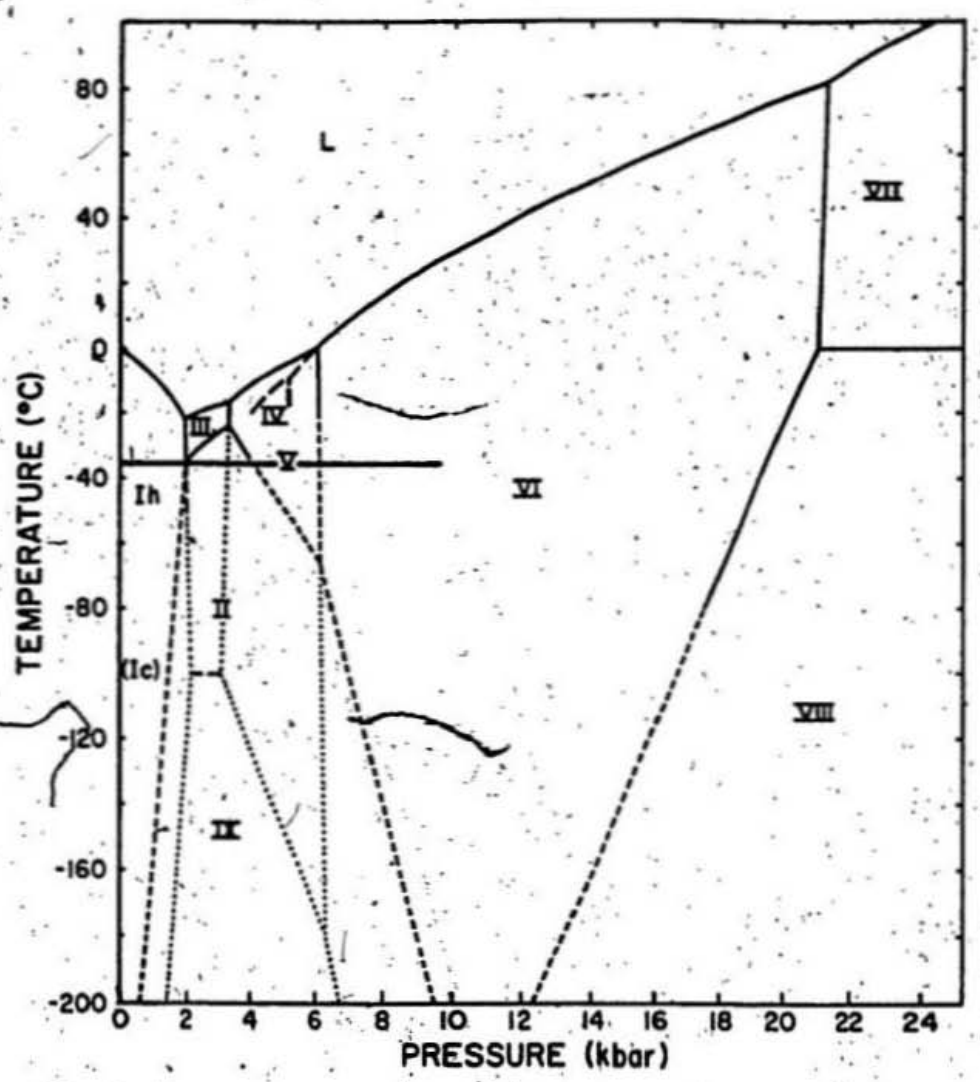
TEMPERATURE (°C)
PRESSURE (kbar)
80
40
0
-40
-80
-120
-160
-200
0
2
4
6
8
10
12
14
16
18
20
22
24
L
VII
III
IV
V
Ih
VI
II
(Ic)
VIII
IX

Figure 1.1

of the century. X-ray diffraction experiments were used by Rinne,[67] St.John[68] and Dennison[69] to determine the structure of ice Ih. The crystallographic symmetries were shown to be represented by the $P6_3/mmc$ space group. Later the positions of protons in ice Ih were determined using nuclear magnetic resonance (NMR) by Kume[70], Kume and Hoshima[71], Korst et al.,[72] Barnaal and Lowe,[73] Rabideau and Denison[74] and Siegle and Wiethase.[75] One proton was shown to lie approximately on the line between each pair of oxygen atoms at a position dividing the O-O length in the ratio of about 2:1. The unit cell contains 4 molecules.

At atmospheric pressure and low temperature, water has two solid phases, amorphous ice, first observed by Burton and Oliver[76] using x-ray diffraction, and a cubic phase, ice Ic, represented by the space group $Fd\bar{3}m$, observed by König[77] using electron diffraction techniques. The unit cell in ice Ic contains 8 molecules.

Tammann[78] was the first to investigate the high pressure regions of the phase diagram. At approximately 2.2 kbar and between -30°C and -50°C he found that ice Ih transformed into a denser solid, later termed ice III by Bridgman.[79] Using x-ray data from powdered and single crystal samples Kamb and Datta[80] and Kamb and Prakash[65] determined that it has a tetragonal structure. The space group is $P4_12_12$ and the unit cell contains 12 molecules.

At a temperature between -70°C and -80°C Tammann[78] discovered the formation of a denser phase, ice II, at a pressure just below 2 kbar. Kamb,[81] using x-ray diffraction data, determined that the structure is rhombohedral with unit cells containing 12 water molecules. The space group is $R\bar{3}$.

Bridgman[79] found that at 3.7 kbar ice III transformed to the denser

solid ice V. Bertie et al.[82] and Kamb and Knobler[83] determined the structure of ice V using x-ray powder patterns. Monoclinic cells contain 28 water molecules and the space group is A2/a. Bridgman[84] discovered another polymorph, ice IV, which sometimes formed in the region of phase stability of ice V and which was completely unstable with respect to ice V. Its structure has been determined by Engelhardt and Kamb[85] by use of x-ray diffraction. The unit cell is rhombohedral and contains 16 molecules. The space group is $R\bar{3}c$.

Bridgman[79] found that ice V transformed to the denser ice VI at 6.3 kbar. Kamb[64] used x-ray diffraction data to show that the structure consisted of tetragonal unit cells which contain 10 water molecules and that the space group is $P4_2/nmc$. Later Bridgman[86] observed that ice VI transformed to ice VII between 20 kbar and 25 kbar. X-ray powder diffraction patterns for this phase were obtained by Kamb and Davis[87] and the structure was subsequently found to be body-centered cubic with crystallographic symmetries represented by the space group Pn3m. Each cell contains 2 molecules.

The first indication of another phase in this pressure region came from Bridgman,[86] who noted that the P-T phase boundary between ice VI and ice VII changed shape near 0°C. The existence of ice VIII was clearly demonstrated by Whalley et al.[88] using dielectric methods. The structure of ice VIII is the same as that of ice VII except that the entropy is lower because the protons are ordered in ice VIII, that is, they remain at one site, whereas in ice VII there are a large number of likely proton configurations.

Ice IX was discovered by Whalley et al.[89] using dielectric methods. It has the same structure as ice III but is partially proton ordered,

whereas ice III is disordered.

The existence of another phase, ice X, has been reported by Polian and Grimsditch.[90] The phase transition from ice VII to ice X at 44 GPa, was detected through the analysis of Brillouin frequency shifts of light scattered from longitudinal sound waves propagating in the ice. This transition was also observed in the Raman scattering experiments of Hirsch and Holzapfel.[91] The structure of this polymorph has not yet been determined experimentally, though the authors suggest that it may be the 'symmetric-ice' predicted by Holzapfel.[92] In this centrosymmetric model the H_2O molecule is not the basic building block. Instead of having hydrogen bonds the model has an ionic structure in which hydrogen atoms are shared between neighbouring oxygen atoms.

Most recently a new low temperature water polymorph, ice XI, has been reported by Suga.[93a] The structure, according to neutron diffraction experiments by Leadbetter et al.,[93b] appears to be orthorhombic with space group $Cmc2_1$. No other experimental studies have yet been reported which would shed light on its properties.

For a more detailed history of the discovery of most of the different ices and an in depth discussion of their structures see Hobbs.[66]

1.3 Theory of Elasticity

A solid is said to deform elastically if it returns to its exact shape after the removal of the stress which caused the deformation. The rapid material deformations associated with the propagation of low amplitude acoustic waves are elastic phenomena. The stresses and

strains in a deformed elastic solid are related according to Hooke's Law.

$$\sigma_{ij} = \sum_{k=1}^{3} \sum_{l=1}^{3} c_{ijkl} e_{kl} \qquad (1\text{-}1)$$

In this expression the element of the stress tensor, σ_{ij}, is the j'th component of force, with units of pressure, acting on the unit element of surface area normal to coordinate i. The strain tensor elements, e_{kl}'s, are dimensionless and specify the spatial rate of change of the displacement of an infinitesimal volume of material from its original (unstrained) position. The linear coefficients, c_{ijkl}, known as the elastic stiffness constants, comprise a 4th rank Cartesian tensor with 3 x 3 x 3 x 3 elements. These constants completely specify the strain behaviour of a crystalline solid subject to any small stress configuration.

In the case of ice Ih, the 81 elastic constants can be greatly simplified and expressed in terms of only 5 independent constants when general crystallographic symmetries, along with specific conditions of hexagonal symmetry, are imposed. The elastic constants are given by c_{11}, c_{12}, c_{13}, c_{33} and c_{44}, where a two subscript notation has been adopted according to the following correspondences,

$$\begin{array}{ll} 11 \rightarrow 1 & 23 \text{ or } 32 \rightarrow 4 \\ 22 \rightarrow 2 & 13 \text{ or } 31 \rightarrow 5 \\ 33 \rightarrow 3 & 12 \text{ or } 21 \rightarrow 6 \end{array} \qquad (1\text{-}2)$$

which are associated with a choice of Cartesian coordinates which places the z axis parallel with the 6-fold axis (c-axis) of the hexagonal single crystal. With this choice of coordinates the 6 x 6

matrix of c_{ij}'s has the form (Musgrave[94]),

$$\begin{bmatrix} c_{11} & c_{12} & c_{13} & 0 & 0 & 0 \\ c_{12} & c_{11} & c_{13} & 0 & 0 & 0 \\ c_{13} & c_{13} & c_{33} & 0 & 0 & 0 \\ 0 & 0 & 0 & c_{44} & 0 & 0 \\ 0 & 0 & 0 & 0 & c_{44} & 0 \\ 0 & 0 & 0 & 0 & 0 & \frac{c_{11}-c_{12}}{2} \end{bmatrix} \qquad (1\text{-}3)$$

Due to the cylindrical isotropy of hexagonal crystals about the c-axis, the elastic properties will vary as a function of crystallographic direction, which need only be defined in terms of the orientation relative to the c-axis. Thus the velocity of acoustic waves depends only on the angle γ, the angle between the propagation vector of the elastic wave and the axis of symmetry of the crystal.

Matrices similar to (1-3) exist for the crystallographic structures of the other ice polymorphs studied here, however, they are not included in this discussion because the experiments on the high pressure phases were performed on polycrystalline samples, and yielded data which were uncorrelated with crystallographic direction. Thus, the full set of elastic constants could not be determined for those phases. The rest of this discussion refers specifically to ice Ih.

In the experiments described in the chapter on single crystals of ice Ih the propagation direction of the acoustic waves is fixed in the laboratory coordinate system. The c-axis orientation is altered in this system, by rotation of the ice sample, so that a range of gamma angles can be investigated. The angle γ is given by the following expression,

$$\gamma = \cos^{-1}\left((\cos\Phi \sin\theta + \cos\theta) / \sqrt{2} \right) \qquad (1\text{-}4)$$

where θ is the angle which the c-axis makes with the vertical laboratory z axis and Φ is the angle which the projection of the c-axis makes on the lab x-y plane in standard Euler angle notation.

If acoustic velocities are known for a variety of crystallographic directions, then the equations which describe elastic wave propagation in single crystals can be used to determine the elastic constants of the medium. The equations which link density, elastic constants, wave speed and direction are derived by application of Newton's second law to an infinitesimal element of volume in the crystal, where the force applied to the element is determined according to Hooke's Law. The procedure produces a 3 x 3 dynamical matrix with a vanishing determinant. The elements of the matrix are linear combinations of the elastic constants and the product of the density with the square of the sound velocity. Three solutions result from this and yield distinct velocities corresponding to three acoustic modes, one longitudinal and two transverse. A detailed derivation is given in the thesis of Gammon.[95] The equations are given below (Musgrave[94]).

$$V_L = (2\rho)^{-1/2} \Big[c_{11} \sin^2\gamma + c_{33} \cos^2\gamma + c_{44} + [(c_{11} \sin^2\gamma + c_{33} \cos^2\gamma - c_{44})^2 - 4 \sin^2\gamma \cos^2\gamma \times ((c_{11} - c_{44})(c_{33} - c_{44}) - (c_{13} + c_{44})^2)]^{1/2} \Big]^{1/2} \qquad (1\text{-}5)$$

$$V_{T1} = (2\rho)^{-1/2} \left[(c_{11} - c_{12}) \sin^2\gamma + 2 c_{44} \cos^2\gamma \right]^{1/2} \qquad (1\text{-}6)$$

$$V_{T2} = (2\rho)^{-1/2} \Big[c_{11} \sin^2\gamma + c_{33} \cos^2\gamma + c_{44} - [(c_{11} \sin^2\gamma + c_{33} \cos^2\gamma - c_{44})^2 - 4 \sin^2\gamma \cos^2\gamma \times ((c_{11} - c_{44})(c_{33} - c_{44}) - (c_{13} + c_{44})^2)]^{1/2} \Big]^{1/2} \qquad (1\text{-}7)$$

In the above expressions ρ denotes density, V_L and V_{T2} are velocities for predominantly longitudinal and transverse acoustic modes respectively and V_{T1} is the velocity of a purely transverse mode with polarization orthogonal to the other transverse mode.

1.4 The Elastic Properties of Ice

Most of the work on the elastic properties of solid H_2O has been carried out on ice Ih because of the relative ease of experimentation compared with studies of the other polymorphs.

Dorsey[96] has reviewed the work on ice Ih up until 1940. Most of these experiments, which were subject to error arising from plastic creep, involved static techniques applied to polycrystalline samples. The results exhibited considerable scatter. The few dynamic determinations, which involved sound velocity measurements on polycrystals, yielded values for Young's modulus and Poisson's ratio which were reasonably consistent. The main source of error in these experiments was probably due to preferred crystal orientation. Dynamic techniques, up until that time, were not sufficiently precise to determine a full set of elastic constants for single crystals of ice Ih.

The first complete set of elastic constants for ice Ih was derived by Penny[97] in 1948 using the ordinary theory of lattice dynamics coupled with the experimentally determined values of Young's modulus and Poisson's ratio for polycrystalline ice obtained by Northwood.[98] The polycrystalline data were linked to the elastic constants of single crystals by use of the averaging procedure of Voigt.[99] In spite of Penny's erroneous assumption that protons in ice Ih were situated

midway between oxygen atoms, her values for the elastic constants would have agreed remarkably well with those of more recent experiments had the uncertainties inherent in Voigt's averaging procedure, and in the results of Northwood, not been present.

In 1952 Jona and Scherrer[100] reported the first experimental determination of the full set of elastic moduli for single crystal ice Ih. The Schaefer-Bergmann method, which makes use of the diffraction of monochromatic light by acoustically induced periodic spatial variations of refractive index in transparent solids, was used for these determinations. The artificially grown samples were held at a temperature of -16°C during these experiments. The diffraction patterns were used to obtain the acoustic wavelength of the sound in the ice and the velocity was then deduced from the known resonant frequency of the quartz transducer which was used to generate the acoustic waves. The results of these experiments agreed to within experimental uncertainty with those of Penny.[97]

In 1956 Green and Mackinnon[101] conducted experiments on single crystals of ice Ih using the pulse transmission method. Transit times were determined for compressional and shear waves travelling along the c-axis, from which the elastic constants c_{11} and c_{44} were calculated. Penny's[97] three theoretical relations were then used to determine the other three elastic moduli. There was approximate agreement between these results and those of Jona and Scherrer.[100]

The resonant bar technique was used to determine the complete set of elastic compliance constants for monocrystalline ice by Bass et al.[102] in 1957. The matrix of compliance constants $[s_{ij}]$ is the inverse of the matrix of stiffness constants $[c_{ij}]$. The method involved setting

up acoustic resonant vibrations in bars and plates of ice and observing the induced nodal patterns. The temperature dependence of the compliance moduli was also determined in the range -2°C to -30°C.

Bogorodskii,[103] in 1964, was the first to determine the full set of elastic moduli for natural ice. Acoustic travel times were measured in lake ice single crystals for three different crystallographic directions. However, the elastic constants calculated from these measurements had a fairly high degree of uncertainty (10%) because of imprecision in the velocity results.

In 1964 Brockamp and Querfurth[104] used the ultrasonic pulse transmission technique to determine the elastic moduli for artificially grown ice in the temperature range -20°C to near 0°C. Results agreed well with those of Jona and Scherrer.[100] Very near the melting point, however, there was an unexpected 5% drop in the elastic moduli.

Also in 1964 Zarembovitch and Kahane[105] used the Schaefer-Bergmann method to investigate the temperature dependence of two of the elastic constants, c_{11} and c_{33}. Their measurements at -16°C were in excellent agreement with those of Jona and Scherrer.[100]

In 1966 Proctor[106] used an ultrasonic interference technique to investigate the elastic properties of ice Ih in the temperature range -223°C to -23°C. Consecutive acoustic pulses were transmitted through the single crystals and the separation of the pulses was then adjusted so that their reflections within the samples cancelled each other. The separation was then used to calculate the ultrasonic velocity. The full set of elastic constants, and their temperature dependences, were determined throughout the temperature range, -213°C to -163°C.

Dantl[107,108,109] conducted a comprehensive series of ultrasonic

experiments to determine the elastic moduli of ice Ih over the temperature range, -140°C to -.7°C, and to also investigate their frequency dependence over the range 5 MHz to 140 MHz. A pulse echo technique, which involved the measurement of round trip transit times of acoustic pulses emitted and received by a quartz transducer bonded to the ice specimens, was employed to measure relative velocities. A double pulse interference technique, similar to the method of Proctor, was used to determine the absolute velocities. The most striking aspect of the results was that the elastic constants were approximately 5% lower than previously accepted values, notably Jona and Scherrer,[100] which Dantl attributed to an aging process caused by the relaxation of the electric potential which develops along a growing ice crystal as it freezes. The monocrystalline ice used by Dantl had been aged for eight months at a temperature near the melting point, prior to the experiments, and this supposedly explained the difference in the elastic contants obtained from other experiments.

In 1969 Mitzdorf and Helmreich[110] used the pulse echo method to determine the full set of elastic constants, and their temperature dependence, for D_2O ice in the range 0°C to -140°C. From these data the molecular force constants for change in bond length, and change of O-O-O angle, were calculated. With the exception of c_{13}, the elastic constants of deuterated ice were found to be higher than those for ordinary ice. The force constants were also higher in the deuterated ice and they exhibited a temperature dependence similar to the elastic constants.

The first determination of elastic constants for ordinary ice and deuterated ice using Brillouin spectroscopy (described in Section 1.5)

was by Ermolieff[111] in 1975. The main purpose of these experiments was to investigate an anomaly in the temperature dependence of the elastic moduli in the temperature range 70 K to 130 K. Only the moduli c_{11}, c_{33}, and c_{44} were determined for ordinary ice, and c_{11} for deuterated ice.

Until recently Dantl's[108] results have been accepted as the standard values for the elastic moduli of ice Ih. Gammon et al.,[112,113] however, have used Brillouin spectroscopy to determine the complete set of elastic constants of glacial ice, lake ice, sea ice and artificially grown ice. For reasons discussed in Section 1.5 this optical technique probably yielded the best values for the elastic constants to date. Nowhere in the experimental results was there any evidence of an aging process, suggested by Dantl.[107,108,109] Glacial ice, which was very old, yielded essentially the same values for the elastic moduli as did fresh lake ice and artificially grown ice.

The first investigation of the pressure dependence of the elastic constants of single crystals of ice Ih, in the pressure range 0 bar to 400 bar, was reported by Brockamp and Rüter[114] using the ultrasonic pulse transmission method. A linear increase of about 3 m/s per 100 bars was observed in the velocity of longitudinal sound waves, and a decrease of about 2.2 m/s was reported for transverse waves. The pressure dependences of the full set of elastic constants were also determined. Using the averaging techniques of Voigt[99] and Reuss,[115] the authors were able to calculate the elastic constants for polycrystalline nonporous ice Ih. The pressure dependence of the longitudinal wave velocity for porous aggregates of ice Ih was also calculated.

The first determination of longitudinal sound wave velocities in high pressure ice polymorphs was by Polian and Grimsditch,[116] using Brillouin spectroscopy. A diamond-anvil cell was used to pressurize liquid H_2O, at room temperature, until it froze into solid ice VI at approximately 1.5 GPa. Further application of pressure precipitated another phase transformation to ice VII at about 2.5 GPa. Most experiments were carried out on polycrystalline samples, though in some cases it was possible to grow single crystals of ice VI through careful adjustment of the pressure. The authors employed the Brillouin equation ((1-9) of the following section), in conjunction with refractive indices calculated from an expression which related Eulerian strains to refractive indices (using the density data of Bridgman[117] and Munro et al.[118]) to determine velocities based on the measured frequency shifts. The Eulerian strain expression relates the density to the refractive index of the scattering medium. Velocities were obtained in the pressure ranges 1 GPa to 3 GPa; and 2 GPa to 30 GPa for ice VI and ice VII respectively, and discontinuities were observed at phase transformations. Effective elastic moduli were calculated and compared with other bulk moduli.[117,118] The pressure dependence of the effective elastic modulus was about the same for both ices. Ice VI appeared to be elastically fairly isotropic whereas ice VII exhibited elastic anisotropy which decreased with increasing pressure. The density dependence of the velocities in both ices was approximately the same, and close to that of ice Ih.

Brillouin spectroscopy was again used by Polian and Grimsditch[90] to study ice pressurized in a diamond-anvil cell up to 67 GPa at room temperature. At approximately 44 GPa a discontinuity appeared in the

curve of frequency shift versus pressure. This indicated a phase transition to a previously unknown polymorph, ice X, which the authors suggested was the 'symmetric' phase predicted by Holzapfel.[92]

Apart from the present work, the most recent report of elastic wave velocities in high pressure polymorphs was by Shaw.[119] Longitudinal and transverse wave velocities were obtained from polycrystalline aggregates of ice Ih, III, V and VII, using the ultrasonic pulse transmission method, at -25°C. The ice was pressurized in an evacuated-cylinder apparatus. Bulk and shear moduli were calculated for each polymorph. An unexpected decrease in longitudinal wave velocity when ice Ih transformed to ice III was also reported. Shaw's results will be discussed in considerable detail in relationship to the present results in Chapter 4.

1.5 Brillouin Spectroscopy

Brillouin spectroscopy is an optical technique which has been used to investigate the acoustic properties of a variety of condensed materials. These include, for example, liquid crystals, metals, layered compounds, semiconductors and molecular crystals.[90,111-113,116,120-128] Unlike ultrasonic techniques which require piezoelectric transducers to generate and receive acoustic signals, the Brillouin method is used to measure the velocity of spontaneous thermally induced sound waves or, in quantum mechanical terms, phonons.

Acoustic waves are comprised of regions of compression and rarefaction within the medium, which cause fluctuations in the refractive index. In a transparent medium, such as ice, a light beam impinging on such an acoustic wavefront is partially reflected because

of the change in the index of refraction. Furthermore, since the wave is moving, the light frequency is Doppler shifted. The Brillouin method employs a highly collimated and highly monochromatic light source, a laser, to accurately measure the degree of Doppler shift. Then the Brillouin equation, derived below, is used to determine the velocity of the scattering sound wave. The Bragg interference condition is satisfied so that the optical wavelength is equal to the path difference between light reflected from two adjacent wavefronts. Hence, for a fixed geometry, only one acoustic wavelength is selected out of a broad range. The phonon dispersion curve is essentially linear in this region, however, so that the measured phonon velocity is repesentative of the broader range. Figure 1.2 is a classical representation of what is essentially a quantum mechanical phenomenon of photon-phonon scattering, however, it is adequate to explain what is physically observed.

A reflecting wavefront, moving with uniform velocity as it deflects light to an observer, is depicted at time t_0 and t_1. According to Figure 1.2 the optical path difference between path 1 and path 2 in a medium with refractive index n is as given below.

$$\begin{aligned} n\,(x - y) &= n\,(x - x\sin(\pi/2 - \alpha)) \\ &= nx\,(1 - \cos\alpha) \\ &= nd/\sin(\alpha/2)\,(2\sin^2(\alpha/2)) \\ &= 2nd\sin(\alpha/2) \end{aligned} \tag{1-8}$$

Since the difference in optical path due to the moving plane at time t_0 and t_1 is given by (1-8), the light source will appear to have velocity $2Vn\sin(\alpha/2)$ relative to the observer. This gives rise to a

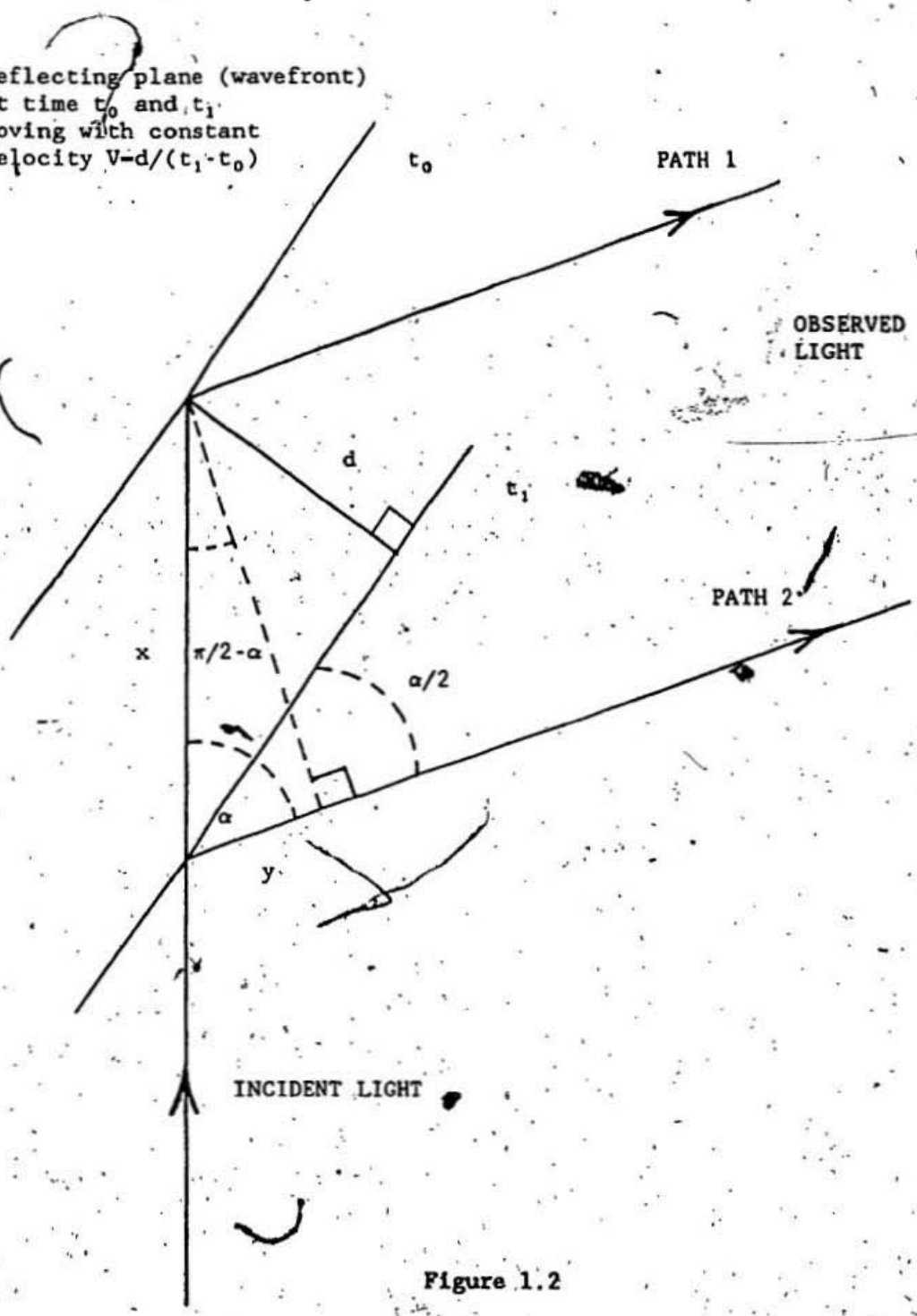
Reflecting plane (wavefront)
at time t_0 and t_1
moving with constant
velocity $V=d/(t_1-t_0)$
t_0
PATH 1
OBSERVED
LIGHT
d
t_1
PATH 2
x
$\pi/2-\alpha$
$\alpha/2$
α
y
INCIDENT LIGHT

Figure 1.2

Doppler shift in the frequency of the light (Jenkins and White[129]),

$$\Omega = (\nu/c)\ 2nV \sin(\alpha/2)$$
$$= (2nV/\lambda) \sin(\alpha/2) \qquad (1\text{-}9)$$

where ν and λ are the frequency and wavelength of the incident light and Ω is the frequency shift. Expression (1-9) is known as the Brillouin equation. The frequency shift may be positive or negative depending on whether the velocity of the acoustic wavefront tends to increase or decrease the optical path.

A rigorous theoretical treatment of the quantum mechanical processes underlying Brillouin spectroscopy can be found in the article of Benedek and Fritsch.[130]

The elastic constants of crystalline media can be found by using acoustic velocity information obtained from the Brillouin equation in conjunction with the dynamic equations which link the elastic constants to the velocities. In particular, the elastic constants of ice Ih can be found using velocity data and equations (1-5), (1-6) and (1-7). The full procedure is described in detail in Section 3.4.

The Brillouin method is highly suited to the present study for a number of reasons. First of all, the sample orientation can be easily altered without having to remove the specimen from the cell, or even changing the confining pressure. Obtaining data for different sample orientations is much more difficult in ultrasonic experiments because the transducers have to be in contact with the specimens and hence must be remounted. Single crystals of ice Ih were produced in such a way that the full range of gamma angle was accessible. Secondly the method is very precise, and systematic errors associated with the parameters

in the Brillouin equation are easy to analyze (Section 3.4). Also the overall uncertainty is independent of the hydrostatic pressure in the cell, whereas ultrasonic techniques suffer from the fact that the quality of acoustic coupling between transducers and specimens changes as the pressure changes, so that it is often difficult to calibrate travel time offsets, especially for shear waves. Finally, the region of observation within the samples is quite tiny ($< 1\ mm^3$) so that specimens can be small and therefore easy to manufacture, and the pressure chamber can be of modest proportions.

The main criteria for the present work are that the samples be relatively clear for laser beam transmission and that their geometry be well defined so that the scattering angle α can be accurately determined.

CHAPTER 2

HIGH PRESSURE, OPTICAL AND ELECTRONIC APPARATUS

2.1 High Pressure Brillouin Cell

The high pressure cell used for the light scattering and density experiments was designed in collaboration with E. Whalley of the High Pressure Section of the National Research Council of Canada. The cell was constructed in Ottawa and then shipped to Memorial University.

Essentially the cell (Figure 2.1) was a solid rectangular block of heat-treated 300 maraging steel with two orthogonal intersecting channels, one drilled down through the center of the top of the block and the other drilled through the lower midsection of one side. The lower opening and two side openings were machined to allow for the insertion of optical ports (I). These consisted of glass windows (J) which were seated on the polished heads of hardened steel mounts. The contact between the smooth surfaces of the glass and the polished steel provided the seal which prevented oil leakage when the cell was pressurized. The glass windows were held in place by annular threaded caps which fitted over the windows and screwed onto the heads of the mounts. The window mounts fitted snuggly into the channels in the cell and were sealed against the walls of the openings with O-rings and beryllium copper backing rings (K). The backing rings were necessary to prevent extrusion of the O-rings at high pressures. The mounts were kept in place by heat-treated gland nuts. The top opening of the cell

Figure 2.1. High pressure cell: A, rotation stem coupler; B, bearing assembly; C, rotation stem; D, cooling fluid circulation for thermal modules; E, thermoelectric modules; F, O-ring and backing rings; G, sample holder; H, single crystal specimen of ice Ih; I, viewing port; J, thick glass window and retaining cap; K, O-ring and backing ring; L, laser beam.

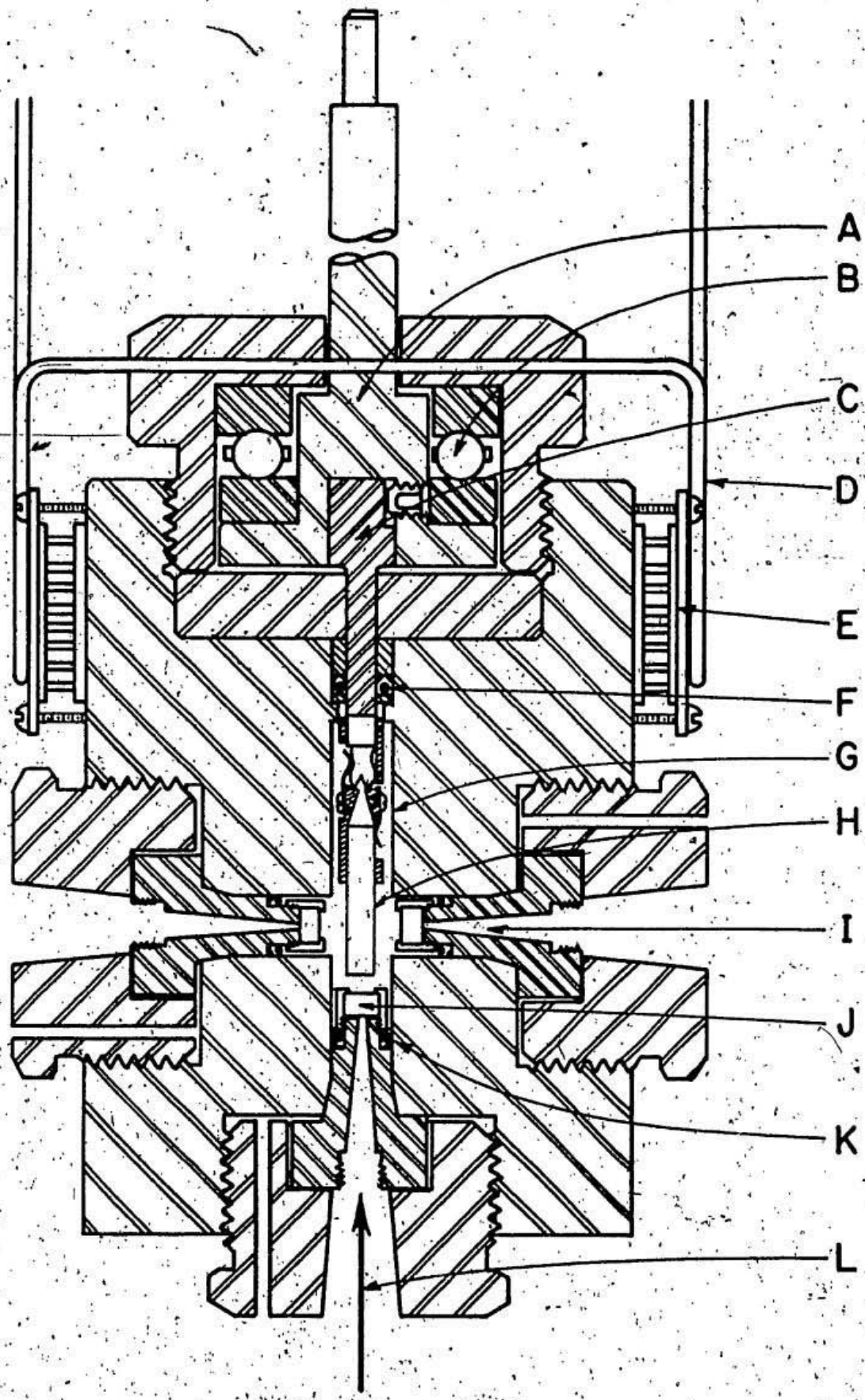

Figure 2.1

was machined so that a rotating stem assembly could be inserted. This consisted of the stem itself (C) which extended from just outside of the small pressurization space in the cell to the inside, where it would be attached to the sample holder (G) and sealed against the wall of the opening with an O-ring and backing rings (F). This stem was secured, by means of a set screw, to a shaft (A) which protruded through the top of the assembly and which was used to externally rotate the stem and sample holder. When the cell was pressurized the rotation stem pushed against this shaft so that the lower flanged portion of the shaft butted against a grooved circular steel ring which served as a track underneath a set of bearings (B). Another track was situated on top of the bearings. This upper track made contact with a gland nut which screwed into the top of the cell and kept the whole assembly in place. This unique stem arrangement made it possible to rotate samples, by hand, even when the cell pressure was elevated to 10 kbar. Without the bearings, friction between metallic surfaces would make sample rotation impossible even at moderate pressures.

One other hole was drilled halfway through the side of the cell until it connected with the channel which had been machined through the top. This was used as the port for the high pressure tubing which ran from the internal-external coupler (B of Figure 2.2) at the top of the cryostat to the cell. The tubing was threaded on both ends and cone shaped to match similar shaped depressions in the coupler and around the hole in the cell. Thick annular threaded steel discs were screwed onto the ends of the tubing and backed by gland nuts which were used to secure the tubing to the coupler and the cell.

Inside the cell, an ice sample (H of Figure 2.1) would be firmly

Figure 2.2. Cryostat housing for high pressure cell: A, precision rotation device; B, high pressure tubing and internal-external coupler; C, rotation coupler; D, circular brass top of cryostat; E, gas outlet for evacuating cryostat; F, port and electrical connections for thermal modules and silicon-diode thermistor; G, O-ring assembly for vacuum sealing the rotation coupler; H, thermally insulating plexiglass plate; I, brass support columns for high pressure cell; J, plexiglass wall of cryostat; K, plane glass window bonded to plexiglass wall; L, silicon-diode thermistor; M, O-ring vacuum seals; N, annular brass bottom of cryostat; O, removable brass plate to facilitate sample transfer; P, quartz window attached to removable plate for laser beam entry.

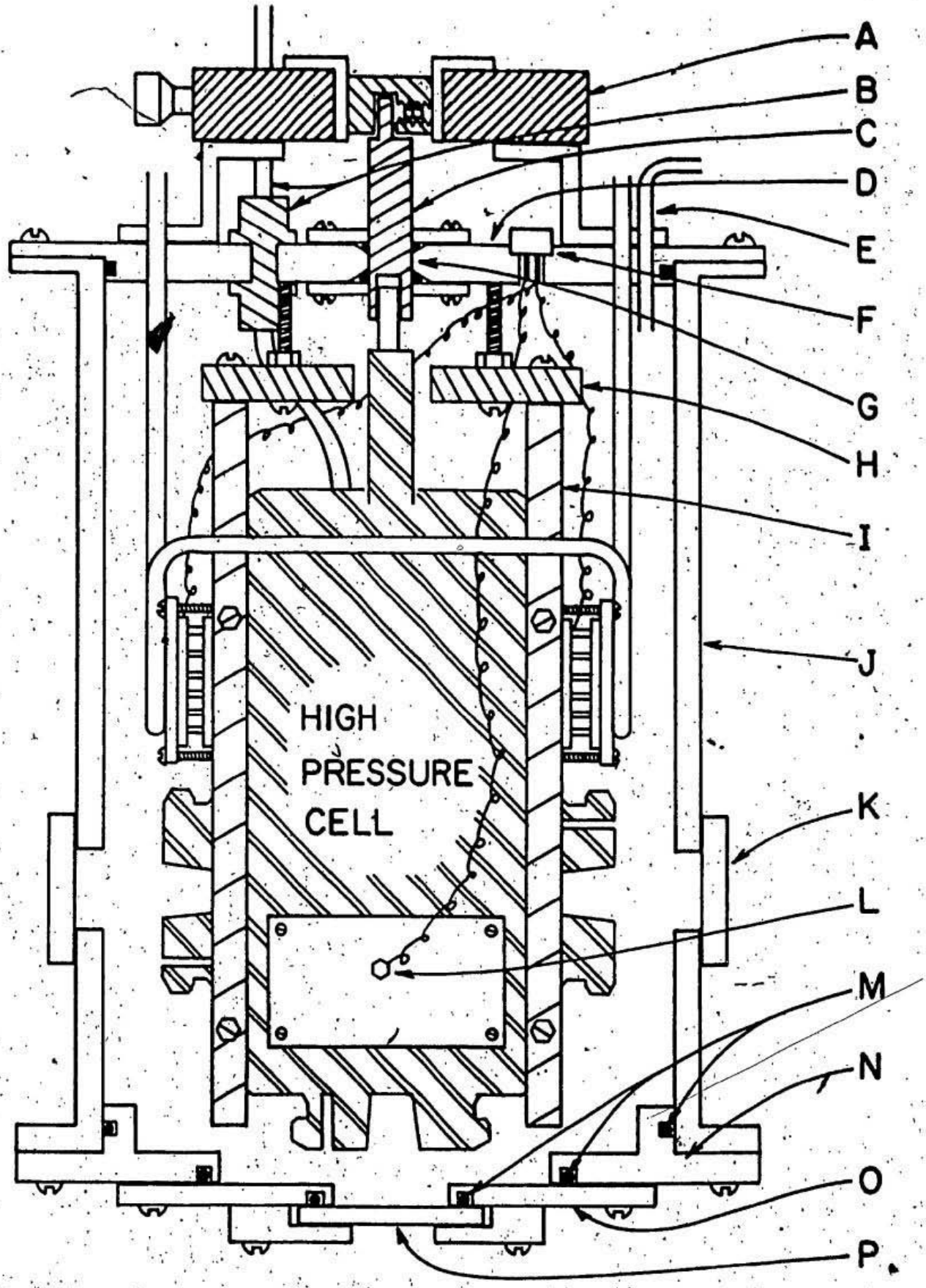

Figure 2.2

held in its holder, which in turn was securely attached to the end of the rotation stem. It would be situated between the two horizontal viewports and directly over the port through which the laser beam entered at the bottom of the cell. After passing through the sample the laser beam would continue through the holder and finally strike the ball shaped end of the rotation stem. The end of the stem had been partially machined out and blackened with flat paint to minimize the amount of back reflected laser light.

To achieve the cold temperatures required for the experiments using the high pressure cell, it was necessary to enclose the cell in an evacuated cryostat and cool it by use of four thermoelectric modules (E of Figure 2.1) attached to its sides. The cryostat (Figure 2.2, lettering refers to this figure unless otherwise indicated) consisted of a section of plexiglass tube, ~16 cm diameter, fitted with a solid brass top (D) and a multisectioned brass bottom. Both top and bottom were sealed with O-rings (M) against the plexiglass wall. Inside, the cell was suspended by four brass columns (I) which were attached to a thick plexiglass plate (H) which had a hole in it for the rotation stem to pass through. The plexiglass was secured to the brass top of the cryostat by four long threaded bolts. During experiments the plexiglass plate provided thermal insulation between the cold cell and the top of the cryostat which was near ambient room temperature. The thermoelectric modules were pressed against the cell by brass plates which were attached by small thermally insulating nylon bolts. Each module had a thin layer of thermal paste applied to its surfaces to ensure maximal thermal transfer during operation. Copper tubing (D of Figure 2.1) had been soldered to the brass plates so that cooling fluid

could be circulated to dissipate the heat liberated from the 'hot' side of the thermal modules. The fluid, a mixture of water and antifreeze, was circulated and kept cold by a Neslab cooler (model RTE-4). The temperature of the cell was monitored to within ±.5°C by means of a silicon-diode sensor (L) (model DT-500, Lake Shore Cryotronics Inc.) attached to a copper plate which was coated with thermal paste underneath and bolted to the cell. The sensor had been previously calibrated against a mercury thermometer, with .1°C graduations, in oil baths at various temperatures. Electrical connections for the thermal modules and the temperature sensor were made at connector plugs (F) which were installed with epoxy cement in holes cut in the brass top of the cryostat.

The partially flattened top section of the cell's rotation stem fitted into a matching end of a stainless steel tube (C) which extended from the inside of the cryostat, through a hole in the brass top, to the outside. The tube was sealed at the top. At the opening in the top of the cryostat, O-rings (G) were configured in such a manner as to permit rotation of the tube while the vacuum was maintained. The top section of the tube coupled to a device (A) (Ardel Kinematic) which was used to accurately rotate the tube, which in turn rotated the stem and ultimately the ice sample situated inside the cell.

At the positions of the two horizontal view ports of the cell, holes were drilled through the plexiglass housing of the cryostat and glass windows (K) were installed over the holes and held in place with silicone glue. This was necessary because the plexiglass, which had originally been optically quite clear, gradually clouded over as a result of a multitude of small surface cracks which probably

accumulated due to the stress induced by the vacuum inside the cryostat.

The bottom of the cryostat consisted of a large annular brass ring (N) which was bolted to the plexiglass housing and sealed with an O-ring. A smaller brass ring (O), to which a quartz window assembly was attached, was bolted and sealed to the larger one. This smaller brass ring with the window (D) was simply and quickly removed whenever samples were transferred to or from the cell.

The cell was pressurized by means of a 3 kbar hand pump (Enerpac) coupled to an intensifier (NRC) which had a hydraulic ratio of 16:1. The hydraulic medium, which was supplied to the cell through high pressure stainless steel tubing, was a clear oil, dioctyl-sebacate, commonly known as Monoplex™. This oil remained clear at all pressures and was not photochemically effected by the passage of the laser beam. Another important feature of the oil was that the individual molecules were very large. This effectively prevented the formation of clathrate hydrates with any of the high pressure ice polymorphs. Clathrate hydration occurs when quest molecules of suitably small size, such as CH_4 or H_2S, become trapped inside ice as a result of caging, which is a process whereby the water molecules arrange themselves to form cages surrounding the guest molecules. The formation of clathrate hydrates would dramatically change the structure and elastic properties of ice.

Pressure inside the cell was measured by means of two gauges. One (3 kbar Heise) measured the pressure on the low pressure side of the intensifier. The other (NRC) was situated on the high pressure side of the intensifier and consisted mainly of a manganin wire inside a heat treated steel housing. The resistance of the wire changed as the

hydrostatic pressure was applied. It had been calibrated at NRC prior to its shipment to M.U.N. During initial experiments it was found that the resistance of the wire seemed to oscillate and drift over time even though the cell pressure was maintained at one value. It was, therefore decided to perform a quick calibration, before drifting could influence the results, of the small gauge pressure against the larger gauge throughout the whole pressure range. Once this was done, the pressure inside the cell could be determined by monitoring the pressure of the smaller Heise gauge. The ratio of pressure readings on the two gauges was not simply 16:1, since the friction of the O-ring in the intensifier had to be taken into account. Two separate calibrations were in fact necessary, one for ascending pressure and one for descending pressure. The Brillouin scattering experiments on single crystals of ice Ih were performed without the pressure intensifier in the oil circuit so that the true pressure was that read off the Heise guage. All other experiments, density and light scattering, were performed with the intensifier in place. The estimated uncertainty in the pressure measurements was ±1%.

2.2 Stabilized Optical Detection and Data Acquisition System

The principal elements of the optical detection system have been described in detail in previous publications.[95,124-128] What follows is a condensed description of the main components. The basic layout is shown in Figure 2.3. The highly monochromatic light source was a single mode argon ion laser (two units were used during the course of this work, a Spectra Physics 165-08 series and also a 2000 series) which provided a beam output power of 100-130 mW at a wavelength of 514.5 nm.

Figure 2.3. Brillouin scattering setup and geometry: B, high pressure sample cell; A, aperture and spatial filter; M, mirror; L, lenses; PM, photomultiplier; AD, amplifier discriminator; DAS, data acquisition and stabilization system.

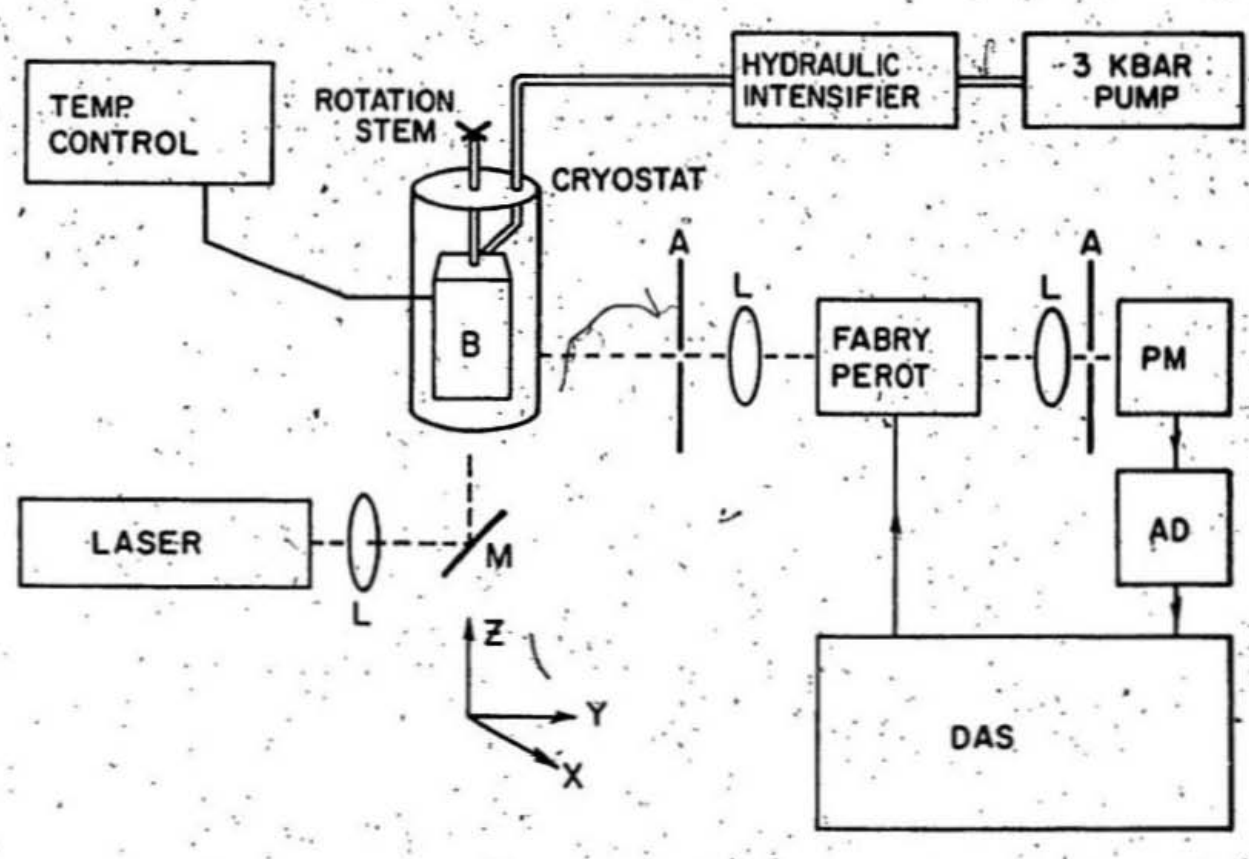
TEMP CONTROL
ROTATION STEM
HYDRAULIC INTENSIFIER
3 KBAR PUMP
CRYOSTAT
A
L
B
FABRY PEROT
L
A
PM
AD
LASER
L
M
Z
Y
X
DAS

Figure 2.3

The effective line width was ~10 MHz. A lens, with focal length 25.4 cm, and front-surfaced plane mirror were used to focus and deflect the beam upwards through 90° into the high pressure cell so that its smallest diameter, about .1 mm, occurred at the observation point within the ice specimen. The mirror could be smoothly and precisely translated to facilitate alignment of the beam within the region of observation defined by the optical detection system. The alignment was carried out, and verified from time to time, by using a thin card in the position normally occupied by the sample, to ensure that the argon laser beam, impinging from one side, precisely overlapped a He-Ne beam which impinged from the other side of the card, and which had been previously aligned along the axis of the optical detection system.

The angle α, which appears in the Brillouin equation (1-9), is the angle through which the incident light is deflected during the scattering process. In this experimental setup, this angle, corresponding to the angle between the incident beam and the axis of the optical detection system, was chosen to be 90°. The angle was set, and checked occasionally, by using a pentaprism to direct the incident laser beam along the path of the previously mentioned He-Ne beam. Using this method, α could be set to the desired angle to within an estimated uncertainty of ±.2°.

Light, scattered from the region of observation in the sample, was collimated by a lens (focal length = 40 cm) and then analyzed by a piezoelectrically scanned triple-pass Fabry-Perot interferometer (Burleigh Instruments Inc. model RC-110). A diaphragm, with an adjustable aperture, was used to limit the angular radius of the cone of light reaching the interferometer to ~.5°. The plates of the

interferometer were flat to within $\lambda/200$ and had a reflectivity of 93%. The ratio of free spectral range (FSR) to instrumental half width, known as finesse, was typically greater than 50. Defined as the apparent frequency separation between consecutive orders of interference within the interferometer, the FSR is given by $c/(2d)$, where c is the speed of light in a vacuum and d is the separation between the interferometer plates. The plate separation was precisely measured with a digital micrometer, and also calibrated using the Brillouin spectrum of a standard quartz block, so that the accuracy of the FSR, for all subsequent calculations, was better than .1%. A number of free spectral ranges were used during the course of this work, depending on which polymorph was under investigation (Chapter 4).

Before passing to the photomultiplier tube detector (ITT FW 130), the scattered light which was transmitted by the interferometer was spatially filtered in order to minimize the effect of stray light scattered from the interior of the cell. This was accomplished by placing a lens and pinhole between the Fabry-Perot and the photomultiplier tube (PMT) such that the pinhole was situated at the focal point of the lens. Light which originated from points around the periphery of the small volume of observation within the ice samples would come to focus outside of the pinhole and hence would not be transmitted to the PMT.

A Burleigh Instruments Inc. DAS 1 (Data Aquisition and Stabilization) system provided a voltage ramp which was used to repetitively scan the interferometer so that data could be accumulated over a time scale of hours or days, depending on the quality of the light scattering signal. The DAS unit contained a 1024 channel

multichannel analyzer for data storage and display. The system was stabilized by two independent electronic stabilization units within the DAS. One unit compensated for drift in the laser frequency or effectively the Fabry-Perot plate separation by locking a particular spectral feature to a given channel. The other ensured that optimally parallel plate alignment was maintained for indefinite periods of time. Both stabilization modules utilized negative feedback circuitry.

The multichannel analyzer of the DAS displayed data in the form of photon counts versus channel number, where the photon counts corresponded to the intensity of the light which was transmitted through the interferometer, detected by the PMT and processed by an amplifier discriminator (PAR 1120). The voltage ramp used to scan the interferometer, and hence Fabry-Perot plate separation, was linearly related to the channel number. Therefore the frequency of the transmitted light was directly proportional to the channel number.

An important aspect of the DAS, which was utilized for most of the experiments in this work, was a segmented time base feature which allowed the slope of the digital voltage ramp to be reduced over a prescribed number of channels. This effectively increased the spectral accumulation time in that interval by a chosen factor ranging from 2 to 99, relative to the other channels. Hence, an amplification window could be placed over the portion of the spectrum of interest for any given light scattering experiment, and this would considerably reduce the run time.

CHAPTER 3

PRESSURE DEPENDENCE OF THE ELASTIC CONSTANTS OF ICE Ih

3.1 Sample Preparation for Ice Ih

In order to accurately determine the pressure dependence of the full set of elastic constants for ice Ih it was necessary to produce right cylindrical single crystals which could be placed inside the high pressure cell. The first stage in the preparation was to cut a very rough rectangular single crystal (1 cm x 1 cm x 6 cm) from a large piece of Mendenhall monocrystalline ice. This was done using a thin copper tube which had warm tap water circulating through it to melt the ice. Prior to this, the c-axis of the large crystal was roughly determined by placing it between crossed polarized filters, situated between a white light source and the viewer, and orienting it until a rainbow pattern was visible. This was indicative of interference between ordinary and extraordinary light beams in the ice. The appearance of the colorful pattern in a thick crystal implied that the c-axis was pointing at the observer. Its orientation was thereby roughly obtained. The rectangular crystal was then cut so that the c-axis was oriented at about 45° to its long axis. It was then frozen onto an aluminum block in an upright position and placed in the melt extrusion device (Figure 3.1) inside the freezer.

The melt extrusion device consisted of a plexiglass plate (C) which had three identical brass rods (F) attached in a triangular configuration pointing upwards normal to the plate. A solid circular

Figure 3.1. Device for producing cylindrical monocrystalline specimens of ice Ih: A, large single crystal of Mendenhall glacial ice; B, aluminum stablization block frozen to the ice; C, plexiglass plate; D, warm copper disc; E, center hole in disc through which unmelted ice passes to produce optically high quality samples; F, brass guide rods, attached to the plexiglass plate, which pass through holes in the periphery of the copper plate and facilitate uniform motion as it melts the ice.

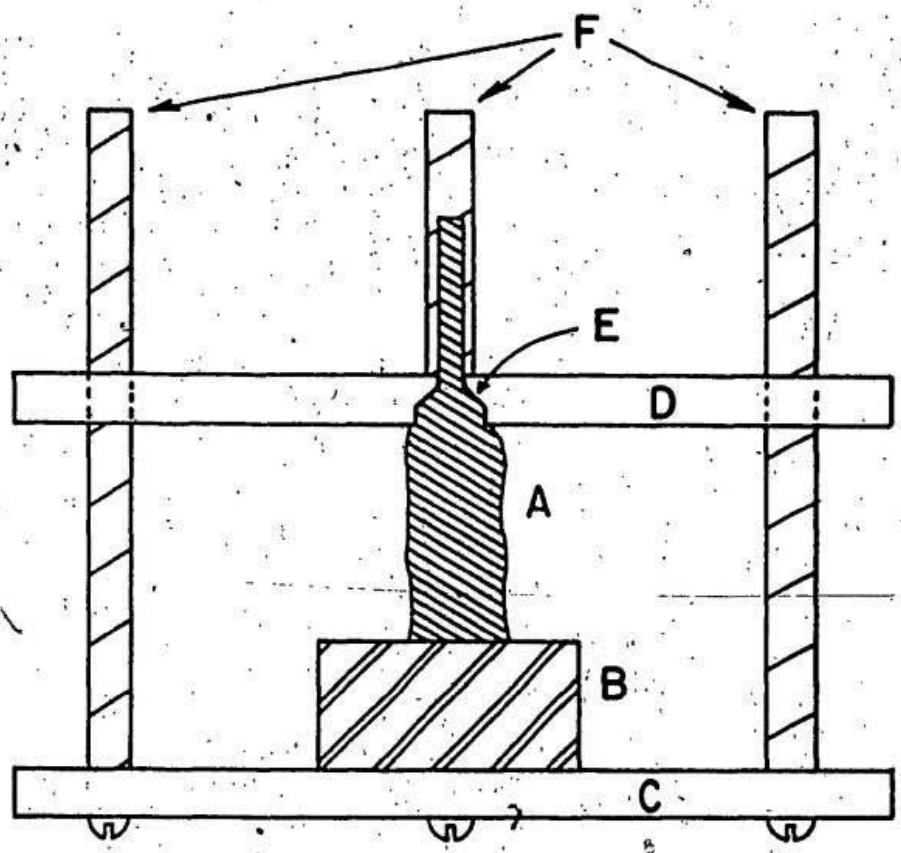

Figure 3.1

copper plate (D) had been previously drilled so that it had three holes around its periphery, through which the three rods of the plexiglass plate could smoothly pass. The center of the copper plate (E) had been drilled part way through with a bit (7 mm diameter). A smaller hole (4.5 mm diameter) had been drilled completely through the plate, concentric with the larger recessed area. After the aluminum block (B) and ice sample (A) had been placed in the center of the plexiglass, the copper plate was cooled to -10°C and gently placed over the apparatus so that the brass rods protruded through its stabilizing holes and the ice specimen was situated directly beneath the small center hole at the top. The plate was then slid down the rods and brought into contact with the ice which immediately began to melt. Under the influence of its own weight, and guided by the rods, the plate evenly melted its way to the aluminum block. All ice melted in the process except for a slender temperate cylinder protruding from the small center hole of the plate. The thin surface layer of melt water on the cylindrical sample quickly froze in the cool atmosphere of the freezer leaving a perfectly smooth and even finish on its wall. As soon as the plate melted its way to the aluminum block the sample was gripped and broken off at the base with a tweezer-like device made of stainless steel wire. After it had been inspected for surface uneveness or tapering, the top end was inserted into the sample holder (G of Figure 2.1). The diameter of the sample was such that it fitted snugly into the holder and the clip prevented it from sliding out or rotating. The end of the specimen was then trimmed to about 11 mm from the holder with a cold pair of wire strippers and roughly flattened with sandpaper.

To avoid error in the scattering angle, the end of the sample

protruding from the holder had to be very flat and normal to the sample's long axis. This was done by placing the holder onto the end of a brass stem designed to couple to the holder in the same manner as the rotation stem inside the high pressure cell. This stem, with holder and ice sample attached, was inserted into a closely fitting brass tube. The stem was pushed in far enough so that the end of the ice specimen was at the tube's midsection. Then a roughly circular piece of thin glass slide was placed on the flat end of a brass rod which could fit snugly into the other opening of the brass tube. The diameter of the piece of glass was slightly larger than that of the ice sample and was held in place on the end of the rod by the surface tension of a thin film of oil.

The rod was cooled to just below 0°C. Then the end with the glass was quickly warmed by hand to a few degrees above 0°C and inserted into the opposite opening of the tube into which the ice sample had been placed. It was pushed in until the glass made contact with the end of the cylindrical ice specimen. A small amount of melting took place as a result of the residual heat of the brass.

Within a few minutes the melt water refroze and the stem, with the ice holder, was removed from the brass tube. The thin glass piece, which had previously been weakly attached to the brass rod by the oil's surface tension, had separated from the rod and was frozen onto the end of the ice sample. A gentle nudge easily detached it from the sample and left a very flat ice surface which was perpendicular to the axis of the specimen. There was a slight ridge around the periphery due to a small excess of refrozen melt water. This was simply removed with sandpaper. The specimen was now ready to have its c axis orientation

accurately determined in the orientation apparatus, and then to be placed in the high pressure cell for the Brillouin scattering experiments.

An alternate method of sample manufacture, for the experiments on ice Ih, was to machine it in a lathe. Before deciding to use the melt extrusion technique the lathe method was tried. It was found, however, that considerable time was required to machine samples and breakages were frequent because of their small size. Also the finish on the wall surfaces was of poor quality for optical experiments. The melt extrusion method, on the other hand, was fast (less than 1/2 hr), reliable and produced a glassy finish on the samples.

3.2 Sample C-axis Orientation Method for Ice Ih

After a right-cylindrical sample of single-crystal glacial ice had been produced using the melt extrusion method, it was necessary to determine its crystallographic c-axis orientation for the purpose of analyzing the Brillouin frequency-shift data. Normally, for water ice and solid phases of other substances, x-ray Laue photography would be employed. A separate cryostat, however, would have been required since the high pressure cell and its cryostat were not suitable for this purpose. Also, the Laue method sometimes takes hours to perform and the time that samples would have spent outside the protective environment of the hydraulic oil would have increased the likelihood of damage to their surfaces as a result of moisture condensation and sublimation. This would have been especially true during sample transfer from one apparatus to another.

To alleviate this problem a simpler and much faster technique was

developed. Hexagonal ice is birefringent and this fact was exploited by constructing an apparatus (Figure 3.2) which could accurately determine the angle at which extinction occurred when an ice sample was placed between two crossed polarized filters. A cubical plexiglass box had holes (~9 mm diameter) drilled through the centers of a pair of opposing faces and a cylindrical brass tube (D) was inserted and friction fitted into place. Prior to its insertion the tube was drilled with two holes opposite each other so that when placed in the box the tube could be oriented to give a clear optical path through the center of two faces of the box. Holes (~5 mm diameter) were drilled through these opposing faces. Recessed areas, concentric with these holes, were put in place by milling part way through the plexiglass. These served as seats for two cylindrical plexiglass plugs (H) which each had a polaroid filter (I) attached to it so that the filters were at a 90° angle to each other. The plugs were connected together by a plastic retaining arm (K) which maintained the relative orientation of the filters and also served as a handle whereby the filters could be rotated relative to the box. The arm also had a small incandescent white light source (J) attached to one side so that the filament lay directly over the hole in that face. On the opposite side the arm had a lens (M) affixed to it, centered on that hole. The focal length of the lens was such that an object placed at the midpoint of the line joining the centers of the polarized filters would be in focus. On the same side, the arm had a circular protractor (L) with .5° markings attached to it, concentric with the hole in the plexiglass. This was used to monitor the angular orientation of the arm and filters relative to a fine line etched on the diagonal of that face of the box.

Figure 3.2. C-axis orientation device: A, ice Ih single crystal; B, sample holder; C, brass rod; D, brass tube; E, clamp; F, hollow stainless steel tube; G, plexiglass box; H, plexiglass disc ; I, polaroid filter ; J, small incandescent light source ; K , rotation arm ; L, protractors with .5 degree markings; M, lens.

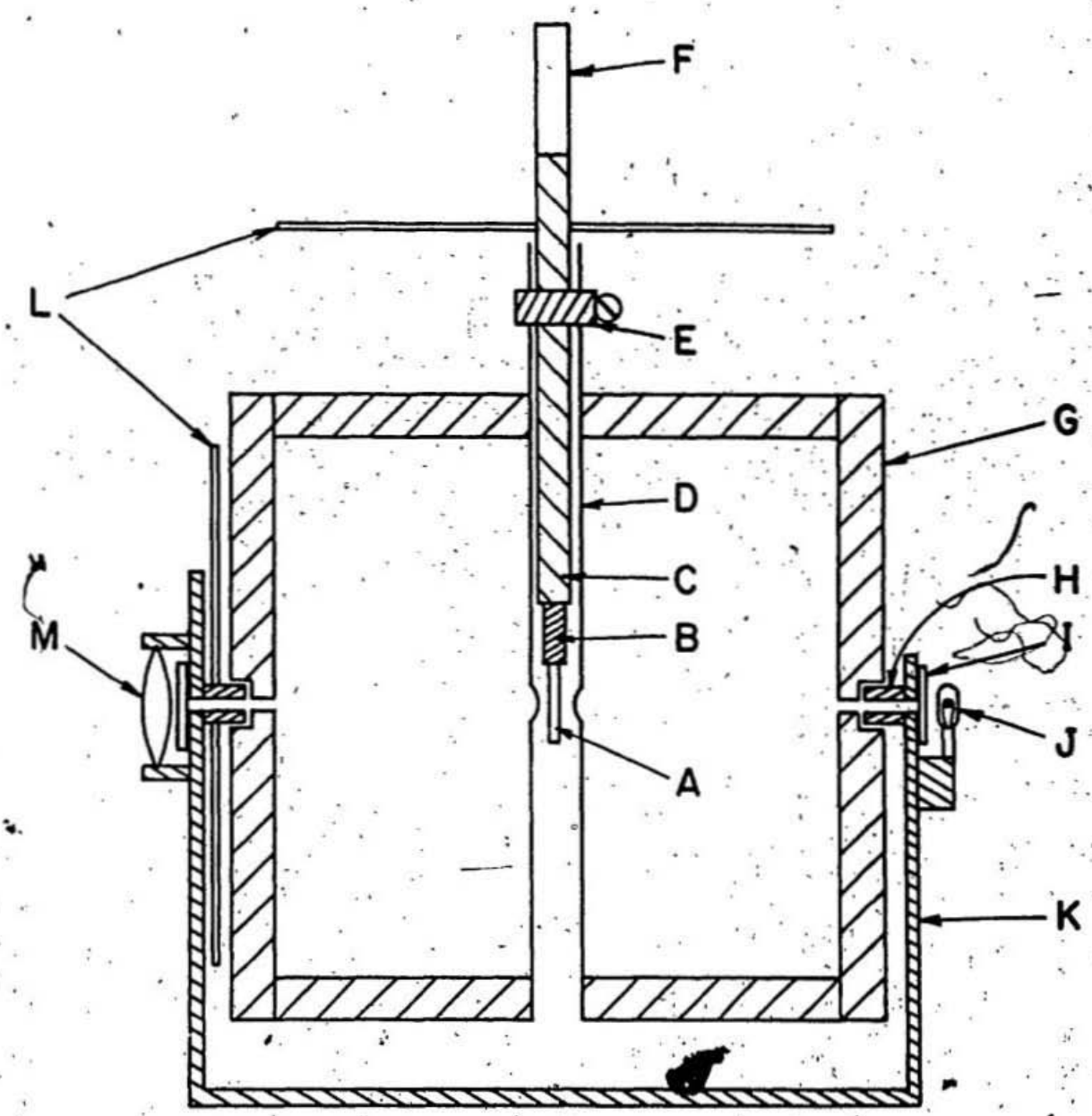

Figure 3.2

A solid brass stem (C) was constructed to which the ice sample holder (B), which was to be used in the high pressure cell, could be securely attached. The end of this stem had the same design as the stem of the Brillouin cell, which allowed rotation of the ice samples. The other end was soldered to a thermally insulating hollow stainless steel tube (F) of the same diameter. This diameter closely fitted the inside diameter of the brass tube which ran through the center of the box. This stem arrangment, with ice and holder attached, could be snugly inserted into the tube so that the ice sample (A) would be visible through the holes in the tube and box. A clamp (E), placed over the protruding end of the tube at the top of the box, could be tightened to prevent movement of the sample once the stainless steel tube had been rotated to suitably orient the stem. A circular protractor (L) was attached to the stem so that its orientation about the vertical axis could be accurately monitored relative to a line etched on the top of the box.

A view through the observation lens, without a sample present in the box, would indicate that very little light passed through the crossed polarized filters. When a sample was present, most stem orientations permitted much more light to get through because the birefringent ice split the light into ordinary and extraordinary beams, one polarized along the c-axis and the other at 90° to that. Fractional components of these beams would then be able to pass through the second filter. Only when the c-axis was oriented so that its projection was along the polarization direction of one or the other of the filters would extinction occur. For any stem orientation, extinction could be brought on by rotating the filters to an

appropriate angle which could be precisely determined to within .5° by averaging five observations. This angle represented one of two possibilities; it was either the angle between the projection of the c-axis and the etched line on the box, or it was that angle plus 90°. By rotating the stem by 90° and again recording the angle at which extinction occurred it was possible, by means of a simple geometric expression to generate four sets of possible orientations for the c-axis in terms of the angle it made relative to the vertical axis, designated as theta, and phi, its projected angle on the plane perpendicular to the vertical axis. This whole precedure was repeated again after the stem had been rotated by 45° to produce a second set of possible orientations for the c-axis. From the two sets of orientations only one would be consistent with the requirements that theta be the same for both, and that the difference in phi between the two would be 45°. This was the correct orientation and was subsequently used for the analysis of the frequency shift data. The expressions which relate the angles phi and theta to the angles measured for the c-axis projections (see Figure 3.3) are given by,

$$\Phi = \tan^{-1}(\tan(A) / \tan(B)) \qquad (3\text{-}1)$$

and

$$\theta = \tan^{-1}(\tan(B)\ \sin(\Phi)) - \pi/2 \qquad (3\text{-}2)$$

where A is the measured c-axis projection at a given stem angle, and B is the measured projection angle when the stem was rotated by 90°.

Using this method the calculated values for theta and phi were consistent to within ±.5°.

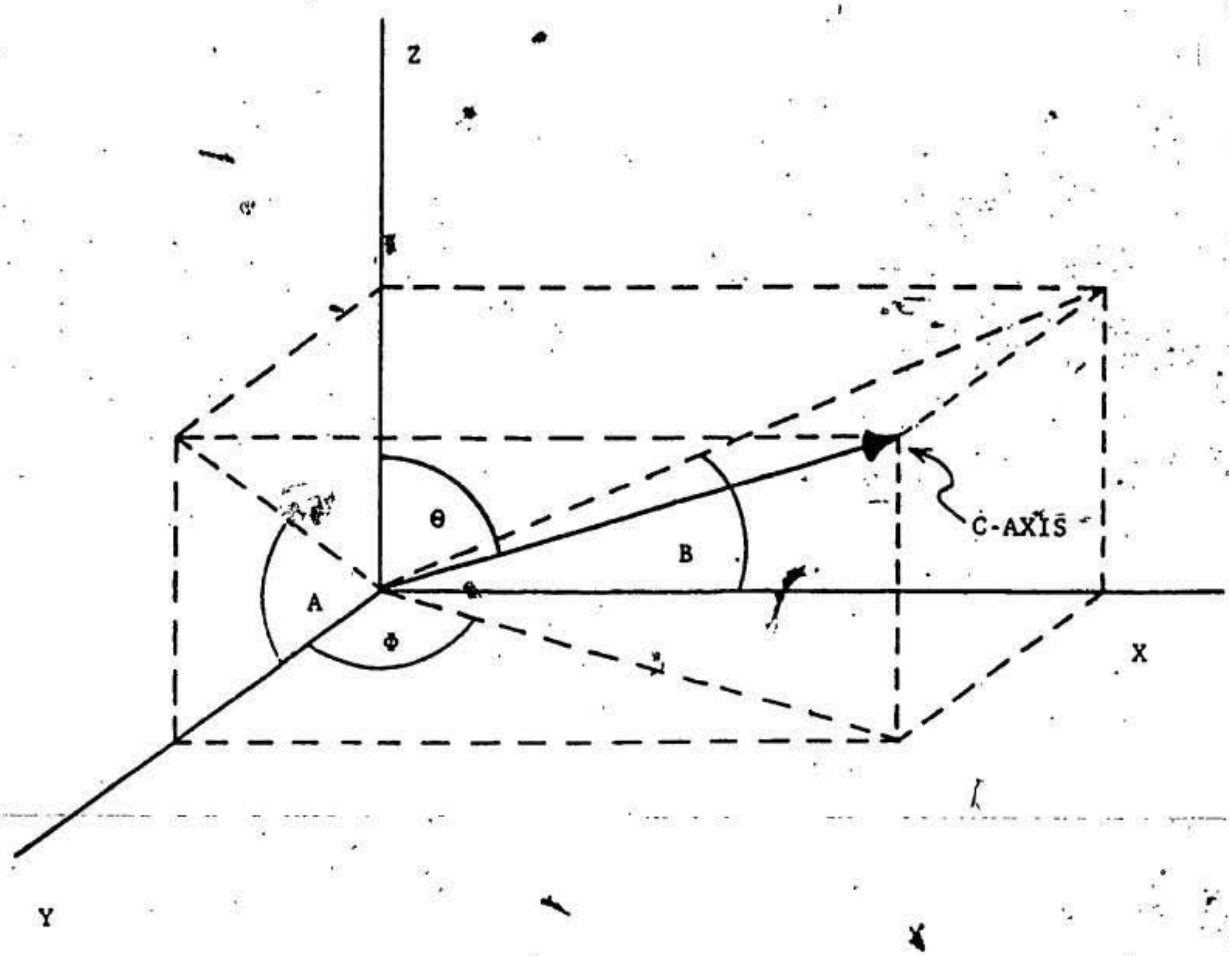

Figure 3.3

3.3 Experimental Procedure and Data Acquisition For Ice Ih

Once a sample of ice Ih had been prepared, and its c-axis orientation determined, the procedure for transfer to the high pressure cell began immediately. First, the holder and sample were attached to a special hand held device, constructed of tubular brass, which fitted over the ice specimen and gripped the end of the holder. This device later facilitated the insertion of the sample into the small chamber of the high pressure cell. The cryostat was then inverted so that the optical port, through which the laser beam entered the high pressure cell, was pointing upwards. The vacuum inside the cryostat was relieved and the bottom plate, to which the cryostat window was attached, was removed. A bolt was screwed into the threaded open end of the high pressure window mount. The gland nut, which secured the mount in its position, was then slackened slightly. A screwdriver, which served as a lever braced against the nut, was then used to pry the head of the bolt and mount out of the opening as far as the gland nut would allow. The nut was slackened further and the window pulled out again. Proceeding in this manner the window mount finally came free of the opening. The gland nut and mount were then completely removed from the cell. The ice sample and holder, gripped on the end of the tubular device described above, were inserted into the partially oil filled chamber, with care taken that the holder properly attached to the rotation stem of the cell. When the holder was securely in place the grip of the tubular device was released and it was removed. A precooled, oil filled hypodermic syringe was used to fill the chamber to the top of the opening. The high pressure window and mount were then inserted and the gland nut screwed back in place. Finally the brass bottom of the

cryostat was reinstalled and the cryostat was inverted and positioned on its stand and evacuated. The temperature setting during this whole procedure was ~-16°C. This was cold enough to avoid any risk of melting the sample, and warm enough to prevent excessive ice buildup on the cell and its window ports from the moisture in the air which was allowed into the cryostat. After the procedure was completed, the electric current supplied to the thermal modules and the temperature of the bath which circulated cooling fluid to the modules were reset so that within 2 hours the cell temperature stabilized to -35.5°C.

The Brillouin frequency shift data in Tables 3.1 to 3.7 were obtained from two samples of Mendenhall glacial ice. The experiments were performed by orienting the sample to a particular γ angle and then running a series of seven experiments, one at each of the pressures 0, .5, 1.0, 1.5, 2.0, 2.5, and 2.8 kbar. The pressure was then reduced to zero and the sample set to a different orientation and another series of experiments were run at the same set of pressures as before.

The zero rotation setting, defined as the angle read on the Ardel rotation device corresponding to the situation where the pin in the rotation stem, and matching slot in the sample holder, were facing in the -Y direction, was determined at zero pressure. A small mirror attached to the flat surface of the stem which protruded through the top of the high pressure cell was used to reflect light back onto a He-Ne laser which was aligned on the Y lab axis. The cell had been constructed such that the flat face of the upper stem pointed in the same direction as the pin on the inside stem. Once the zero rotation setting was known, the value of Φ, the angle which the horizontal projection of the c-axis makes relative to the Y axis in the lab

TABLE 3.1

BRILLOUIN SPECTROSCOPIC DATA FOR HEXAGONAL ICE

Pressure: 0 bar
Temperature: -35.5°C

Euler Angles (deg.)		Gamma Angle (deg.)	Brillouin Frequency Shifts (GHz)		
θ	Φ	γ	Ω_L	Ω_{T1}	Ω_{T2}
47.4	63.7	44.8	13.89	--	--
47.4	48.6	34.6	14.12	--	7.83
47.4	34.0	24.5	14.41	--	7.37
47.4	19.7	14.4	14.69	--	7.00
42.4	0.3	2.6	14.87	6.65	6.65
42.4	5.7	4.7	14.86	--	6.72
42.4	10.8	7.9	14.80	--	6.74
42.4	19.3	13.5	14.72	--	6.94
42.4	31.8	22.0	14.47	--	7.30
42.4	47.2	32.2	14.19	--	7.72
42.4	62.6	42.1	13.96	6.88	7.99
42.4	70.3	46.9	13.88	6.92	8.02
42.4	78.6	52.0	13.87	6.97	--
42.4	95.9	61.8	13.97	6.99	7.67
42.4	115.7	71.6	14.13	7.04	--
42.4	140.2	81.0	14.26	7.08	--
42.4	176.7	87.4	14.29	7.11	--

TABLE 3.2

BRILLOUIN SPECTROSCOPIC DATA FOR HEXAGONAL ICE

Pressure: 503 bar
Temperature: -35.5°C

Euler Angles (deg.)		Gamma Angle (deg.)	Brillouin Frequency Shifts (GHz)		
θ	Φ	γ	Ω_L	Ω_{T1}	Ω_{T2}
47.4	63.7	44.8	14.00	--	--
47.4	48.6	34.6	14.18	--	7.80
47.4	34.0	24.5	14.51	--	7.41
42.4	0.3	2.6	14.99	6.61	--
42.4	5.7	4.7	14.97	--	6.65
42.4	10.8	7.9	14.93	--	6.73
42.4	19.3	13.5	14.81	--	7.00
42.4	31.8	22.0	14.54	--	7.25
42.4	47.2	32.2	14.31	--	7.70
42.4	62.6	42.1	14.04	6.85	7.98
42.4	70.3	46.9	13.99	6.98	8.07
42.4	78.6	52.0	13.98	6.93	--
42.4	95.9	61.8	14.06	7.02	7.60
42.4	115.7	71.6	14.24	--	7.07
42.4	140.2	81.0	14.36	6.99	--
42.4	176.7	87.4	14.39	7.05	--

TABLE 3.3

BRILLOUIN SPECTROSCOPIC DATA FOR HEXAGONAL ICE

Pressure: 1006 bar
Temperature: -35.5°C

Euler Angles (deg.)		Gamma Angle (deg.)	Brillouin Frequency Shifts (GHz)		
θ	Φ	γ	Ω_L	Ω_{t1}	Ω_{t2}
47.4	63.7	44.8	14.07	--	--
47.4	48.6	34.6	14.31	--	7.79
47.4	34.0	24.5	14.61	--	7.34
42.4	0.3	2.6	15.07	6.63	6.63
42.4	5.7	4.7	15.07	--	6.65
42.4	10.8	7.9	15.02	--	6.62
42.4	19.3	13.5	14.90	--	6.85
42.4	31.8	22.0	14.67	--	7.22
42.4	47.2	32.2	14.38	--	7.62
42.4	62.6	42.1	14.14	6.87	7.98
42.4	70.3	46.9	14.08	6.83	7.96
42.4	78.6	52.0	14.09	6.87	--
42.4	95.9	61.8	14.16	--	--
42.4	115.7	71.6	14.31	--	7.06
42.4	140.2	81.0	14.47	7.05	--
42.4	176.7	87.4	14.51	7.07	--

TABLE 3.4

BRILLOUIN SPECTROSCOPIC DATA FOR HEXAGONAL ICE

Pressure: 1507 bar
Temperature: -35.5°C

Euler Angles (deg.)		Gamma Angle (deg.)	Brillouin Frequency Shifts (GHz)		
θ	Φ	γ	Ω_L	Ω_{T1}	Ω_{T2}
47.4	63.7	44.8	14.21	--	7.96
47.4	48.6	34.6	14.38	--	7.74
47.4	34.0	24.5	14.67	--	7.31
42.4	0.3	2.6	15.15	6.63	6.63
42.4	5.7	4.7	15.14	--	6.63
42.4	10.8	7.9	15.10	--	6.66
42.4	19.3	13.5	14.98	--	6.83
42.4	31.8	22.0	14.72	--	7.20
42.4	47.2	32.2	14.43	--	7.59
42.4	62.6	42.1	14.23	6.73	7.95
42.4	70.3	46.9	14.16	6.81	7.91
42.4	78.6	52.0	14.17	6.82	--
42.4	95.9	61.8	14.25	6.89	7.47
42.4	115.7	71.6	14.43	--	7.02
42.4	140.2	81.0	14.52	6.97	--
42.4	176.7	87.4	14.60	7.00	--

TABLE 3.5

BRILLOUIN SPECTROSCOPIC DATA FOR HEXAGONAL ICE

Pressure: 2006 bar
Temperature: -35.5°C

Euler Angles (deg.)		Gamma Angle (deg.)	Brillouin Frequency Shifts (GHz)		
θ	Φ	γ	Ω_L	Ω_{T1}	Ω_{T2}
47.4	63.7	44.8	14.29	--	7.82
47.4	48.6	34.6	14.46	--	7.73
47.4	34.0	24.5	14.75	--	7.29
42.4	0.3	2.6	15.23	6.53	6.53
42.4	5.7	4.7	15.22	--	6.60
42.4	10.8	7.9	15.21	--	6.58
42.4	19.3	13.5	15.08	--	6.79
42.4	31.8	22.0	14.81	--	7.15
42.4	47.2	32.2	14.53	--	7.60
42.4	62.6	42.1	14.32	6.71	7.89
42.4	70.3	46.9	14.25	6.81	7.79
42.4	78.6	52.0	14.25	6.81	7.79
42.4	95.9	61.8	14.30	6.93	7.45
42.4	115.7	71.6	14.50	--	6.98
42.4	140.2	81.0	14.61	6.94	--
42.4	176.7	87.4	14.65	7.04	--

TABLE 3.6

BRILLOUIN SPECTROSCOPIC DATA FOR HEXAGONAL ICE

Pressure: 2504 bar
Temperature: -35.5°C

Euler Angles (deg.)		Gamma Angle (deg.)	Brillouin Frequency Shifts (GHz)		
θ	Φ	γ	Ω_L	Ω_{T1}	Ω_{T2}
47.4	63.7	44.8	14.33	--	7.94
47.4	48.6	34.6	14.53	--	7.74
47.4	34.0	24.5	14.84	--	7.35
42.4	0.3	2.6	15.29	6.51	6.51
42.4	5.7	4.7	15.31	--	6.60
42.4	10.8	7.9	15.29	--	6.56
42.4	19.3	13.5	15.14	--	6.84
42.4	31.8	22.0	14.89	--	7.18
42.4	47.2	32.2	14.61	--	7.54
42.4	62.6	42.1	14.39	6.75	7.93
42.4	70.3	46.9	14.32	6.76	7.94
42.4	78.6	52.0	14.34	6.80	--
42.4	95.9	61.8	14.41	6.85	7.43
42.4	115.7	71.6	14.56	--	6.98
42.4	140.2	81.0	14.68	6.86	--
42.4	176.7	87.4	14.74	6.98	--

TABLE 3.7

BRILLOUIN SPECTROSCOPIC DATA FOR HEXAGONAL ICE

Pressure: 2802 bar
Temperature: -35.5°C

Euler Angles (deg.)		Gamma Angle (deg.)	Brillouin Frequency Shifts (GHz)		
θ	Φ	γ	Ω_L	Ω_{T1}	Ω_{T2}
47.4	63.7	44.8	14.36	6.69	7.88
47.4	48.6	34.6	14.58	--	7.67
47.4	34.0	24.5	14.87	--	7.27
42.4	0.3	2.6	15.35	6.47	6.47
42.4	5.7	4.7	15.33	--	6.53
42.4	10.8	7.9	15.32	--	6.58
42.4	19.3	13.5	15.21	--	6.80
42.4	31.8	22.0	14.94	--	7.13
42.4	47.2	32.2	14.67	--	7.68
42.4	62.6	42.1	14.43	6.71	7.93
42.4	70.3	46.9	14.38	6.73	7.92
42.4	78.6	52.0	14.40	6.77	7.88
42.4	95.9	61.8	14.45	6.78	7.36
42.4	115.7	71.6	14.61	--	7.03
42.4	140.2	81.0	14.76	6.84	--
42.4	176.7	87.4	14.76	6.93	--

reference frame, could be determined for any setting of the rotation device, since the birefringent orientation technique had already been used to determine the c-axis orientation about the stem relative to the pin.

All rotations were made in the same direction to avoid any backlash in the rotation device. It had been observed that the zero rotation setting was slightly different if determined at other pressures. This resulted from the increased torque required to rotate the sample. This was the reason why all sample rotations were made at zero pressure, since only one determination of the zero rotation setting would then be required.

Two crystals were deemed sufficient as a statistical sample base for these experiments because of the high degree of sample-to-sample consistency observed by Gammon[126] in Mendenhall glacial ice, and which was also clearly evident in the present work. The ice itself is a suitable standard because it has low concentrations of impurities, which could contribute to the elastic behaviour.[126]

A total of 16 Brillouin spectra (17 at zero pressure), roughly evenly distributed throughout the whole range of γ angles, were obtained from the two crystals at each pressure. Because of the segmented window placed on the spectral region of interest, which amplified that section by a factor of 70, accumulation times were relatively short, ranging from 15 minutes to 2 hours, depending on the intensity of the transverse signals. Experiments were run until one or both transverse components were reasonably resolved, or until it was clear that no transverse peaks were going to appear, which was the case occasionally. A complete set of data for one pressure typically

required 2 days of experimentation.

The Brillouin spectra (Figure 3.4) were of characteristically low intensity. The relative intensity of unshifted components compared to longitudinal shifted components was approximately 130 to 1, whereas previous Brillouin experiments on methanol, using a similar optical setup, yielded an intensity ratio of 2 to 1.[126] The relatively high intensity of the unshifted component in the present experiments was due primarily to stray reflections within the cell. The linewidths of the central, the longitudinal and transverse components were typically ~.5 GHz. This was effectively the instrumental linewidth. The degree of Rayleigh scattering in the ice was very slight, as was evident by the fact that the laser beam was not visible in the samples as it passed through them. Raman scattered light, on the other hand, was fairly intense and necessitated the placement of a filter, with 1 nm bandwidth centred at the laser frequency, in front of the PMT to block this light which would otherwise increase the background noise level significantly. There was an important beneficial effect of the Raman shifted signal, however, in that it made the beam quite visible in the samples when they were viewed through an orange filter. This effect was fully utilized when optically aligning the cell relative to the laser beam.

The spectral free range of the Fabry-Perot interferometer (25.13 GHz) was chosen to optimally satisfy the following three requirements: 1. That any ambiguity as to which transverse components were associated with which longitudinal components be minimal. 2. That there be no overlap of components throughout the whole range of pressures. 3. That there be maximal resolution so that the data could be used to

Figure 3.4. Representative Brillouin spectrum from a single crystal of Mendenhall ice at -35.5°C. One complete order is shown, with two unshifted central components U. The free spectral range of the Fabry-Perot is 25.13 GHz. L designates the longitudinal Brillouin component and T_1 and T_2 the transverse components as shifted from U. The region of the spectrum showing L, T_1 and T_2 has been amplified 70x in terms of data acquisition.

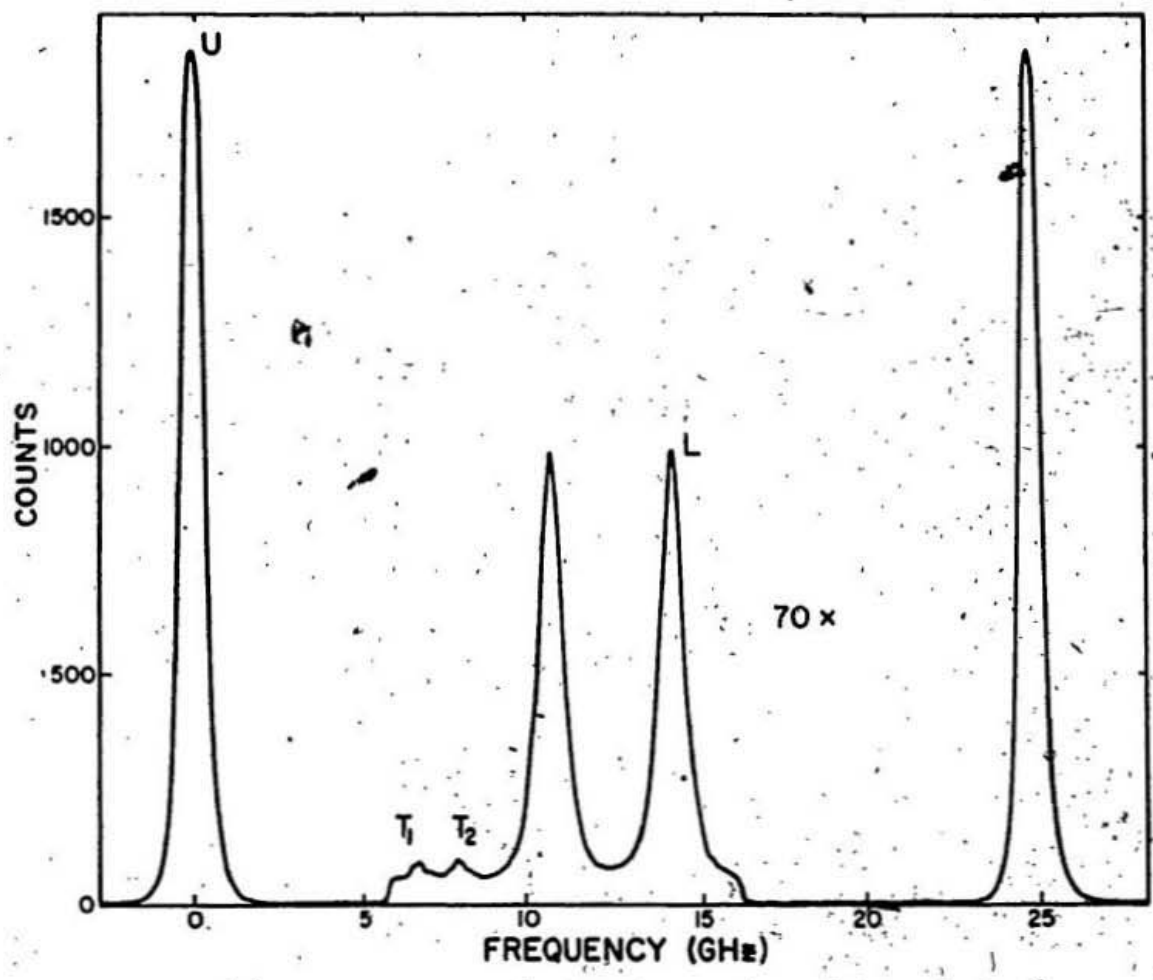

Figure 3.4

accurately determine the elastic constants. In consideration of the last requirement the chosen setting allowed the longitudinal Brillouin peaks to shift by more than 50% of the free spectral range, however, this did not prevent the other requirements from being adequately met.

A frequency shift measurement was made by first smoothing the spectrum a couple of times with a three point smoothing routine, which was an integral feature of the DAS. Then an estimate, to the nearest 1/2 channel (.03 GHz), was made of the separation between the two longitudinal peaks (Figure 3.4) within the amplified window of one order of the Brillouin spectrum. The frequency shift, Ω_L, was obtained using the expression,

$$\Omega_L = \frac{R + N}{2 \times N} \times FSR \qquad (3\text{-}3)$$

where R was the channel separation between the longitudinal peaks and N was the number of channels corresponding to the free spectral range (FSR) of the Fabry-Perot interferometer. N was the measured channel separation between the instrumental peaks of an adjacent spectral order on the DAS display. The transverse frequency shifts were measured relative to the longitudinal components and were obtained from the following expression,

$$\Omega_T = \Omega_L - (T/N) \times FSR \qquad (3\text{-}4)$$

where T was the channel separation between the appropriate longitudinal and transverse components.

Usually the introduction of an amplified section in the scanning range of the interferometer will cause some nonlinearity in the spectrum, and therefore some caution has to be exercised in the

spectral analysis. As a precaution, the accuracy of the results obtained when the amplification window was used was checked by comparing longitudinal frequency shifts from several experiments on ice and a quartz standard, with those obtained when the window was not used. When the window was not used, data from two consecutive orders could be averaged to yield the most accurate results possible using this experimental technique. The longitudinal results, with and without the window, were always in excellent agreement, ±.2%. Transverse data for ice were compared in a similar fashion and a slight constant offset of .07 GHz was discovered, which had to be subtracted from all transverse measurements when the window was employed.

3.4 Determination of the Elastic Constants

The 7 complete sets of frequency shift data, and accompanying crystal orientations, are given in Tables 3.1 to 3.7. The Brillouin equation (1-9) was used to calculate the acoustic velocity associated with each frequency shift. Besides the shift, three pieces of information were required to do this: the wavelength λ of the incident laser light, the scattering angle α and the refractive index n of the ice.

The wavelength λ of the laser was known to be 5.145×10^{-7}m with negligible uncertainty. The scattering angle α had been set to $90^\circ \pm .2^\circ$. The following relation was derived from the Lorentz-Lorenz expression, which relates polarizability and density to the refractive index, and was used to determine the refractive indices for ice at the 7 different pressures, at -35.5°C:

$$n = \left(\frac{1 + 2Z\rho}{1 - Z\rho}\right)^{1/2} \tag{3-5}$$

Here n denotes refractive index, Z is a constant with units of reciprocal density determined from the Lorentz-Lorenz expression using Gammon's[126] refractive index and density of ice at -16°C, and zero pressure. The zero-pressure density, at -35°C, was determined from the expression for the temperature dependence of the density derived by Gammon using the results of Butkovich,[131] and given by,

$$\rho(T) = \rho_0 \left(1 + 1.576 \times 10^{-4}T - 2.778 \times 10^{-7}T^2 + 8.850 \times 10^{-9}T^3 - 1.778 \times 10^{-10}T^4\right)^{-1} \tag{3-6}$$

where ρ_0 denotes the density of ice at 0°C, and T is the temperature in degrees Celsius.

The very slight birefringence of hexagonal ice has a negligible effect on the Brillouin spectra.

Equations (1-5), (1-6), and (1-7) relate the elastic constants, c_{ij}'s, the propagation direction, γ, and the density, ρ, to the velocities of the three acoustic modes in hexagonal media, V_L, V_{T1}, and V_{T2}. They are of the form,

$$f(c_{ij}, \cos^2\gamma) = 2\rho V^2 \tag{3-7}$$

The Brillouin equation linearly relates the velocity of the acoustic modes to the frequency shifts, so that the elastic constants obtained by inverting (1-5), (1-6), and (1-7) depend linearly on the density and on the square of the frequency shifts.

The computational method used to calculate elastic constants from

the observed frequency shift data involved minimizing the squared error, generated from the differences between measured and calculated frequency shifts, by varying assumed values for the elastic constants in expressions (1-5), (1-6), and (1-7). The squared error term, χ^2, is given by,

$$\chi^2(c_{ij}) = \frac{1}{N-5} \sum_{k=1}^{N} \left[\frac{(\Omega_k^{obs.} - \Omega^{calc.}(\gamma_k, c_{ij}))}{\sigma_k} \right]^2 \qquad (3\text{-}8)$$

where N is the total number of observed frequency shifts, N-5 denotes the number of degrees of freedom, $\Omega_k^{obs.}$ is the k'th observed frequency shift, and $\Omega^{calc.}$ is the calculated frequency shift, based on the assumed c_{ij}'s, for sound propagating at an angle γ_k relative to the ice crystal's c-axis. σ_k denotes the standard deviation of the k'th measured frequency shift.

The squared error term was minimized using a modified Newton-Raphson iterative technique which was a principal feature of an existing FORTRAN program described in the thesis of Landheer.[132] The program also contained an analytic routine to determine the nonsystematic errors associated with all of the elastic constants, resulting from measurement errors in the observed data, slight variations in scattering angle and uncertainty in the c-axis orientations.

With data that exhibit nonuniformity in the accuracy of the frequency measurements, different values of σ_k can be used as weighting factors for different data blocks. However, in the present work $\sigma_k = \sigma$, that is, the error associated with all frequency shift

measurements on single crystals of ice Ih was the same. σ was empirically determined by running the FORTRAN program using a reasonable first guess for σ, and then adjusting it according to the statistical criterion that when $\chi^2=1$, σ would be equal to one standard deviation. Hence, the nonsystematic uncertainties computed by the program and quoted for the elastic constants (Tables 3.8 and 3.9) correspond to the situation where χ^2 has been normalized.

The systematic errors associated with the density of Mendenhall glacial ice, and the terms $1/\sin(\alpha/2)$ and $1/n$ of the Brillouin equation were .01%, .17% and .08% respectively.[126] This led to a combined systematic error in the expression ρV^2, and hence the elastic constants, of .38%.

For the analysis of the experiments carried out at elevated pressures it was necessary to determine the pressure dependence of the density of ice Ih. The refractive indices were then calculated using expression (3-5). Density was determined by first converting the zero pressure dynamic elastic constants to isothermal values, in order to obtain the isothermal bulk modulus using the standard expression.[126] Then a reasonable estimate was made for the pressure dependence of the bulk modulus, dB/dP, based on the value obtained by Polian and Grimsditch.[116]

The strain fluctuations associated with acoustic wave propagation in solids occur over very small time intervals ($\sim 10^{-10}$s for Brillouin spectroscopic studies). No heat transfer can take place over such short intervals so that entropy is conserved in the strained regions. Hence it is the adiabatic, constant entropy, elastic constants that are measured when acoustic techniques are used to investigate the elastic

TABLE 3.8

ELASTIC CONSTANTS OF MENDENHALL GLACIAL ICE AT VARIOUS PRESSURES SPANNING THE REGION OF PHASE STABILITY

Phase: Ice Ih
Temperature: -35.5°C

Pressure (kbar)	Elastic Constants (x 10^4 bar)				
	c_{11}	c_{12}	c_{13}	c_{33}	c_{44}
0.000	14.484 ±.14%	7.349 ±.37%	5.965 ±.30%	15.627 ±.10%	3.147 ±.22%
0.503	14.734 ±.29%	7.633 ±.79%	6.186 ±.61%	15.893 ±.22%	3.133 ±.54%
1.006	14.968 ±.20%	7.864 ±.56%	6.508 ±.41%	16.134 ±.15%	3.089 ±.36%
1.507	15.175 ±.21%	8.226 ±.53%	6.773 ±.38%	16.307 ±.16%	3.084 ±.36%
2.006	15.343 ±.23%	8.332 ±.60%	7.082 ±.40%	16.539 ±.18%	3.038 ±.43%
2.504	15.577 ±.27%	8.672 ±.68%	7.168 ±.49%	16.765 ±.21%	3.043 ±.49%
2.802	15.710 ±.25%	8.882 ±.61%	7.312 ±.44%	16.891 ±.20%	3.018 ±.46%

Note: The uncertainties quoted in Table 3.8 refer to nonsystematic error. The systematic error was the same for all of the elastic constants, ±.38%.

TABLE 3.9

DENSITY, REFRACTIVE INDEX AND BULK MODULUS FOR HEXAGONAL ICE AT VARIOUS PRESSURES SPANNING THE REGION OF PHASE STABILITY

Phase: Ice Ih
Temperature: -35.5°C

Pressure (kbar)	Density (g/cm^3)	Refractive Index	Bulk Modulus ($\times 10^4$ bar)	
			Adiabatic	Isothermal
0.000	.9228	1.3141	9.239	8.977
			±.31%	
0.503	.9279	1.3160	9.485	9.216
			±.66%	
1.006	.9329	1.3179	9.759	9.480
			±.46%	
1.507	.9378	1.3197	10.022	9.734
			±.47%	
2.006	.9426	1.3215	10.246	9.950
			±.52%	
2.504	.9473	1.3232	10.436	10.135
			±.60%	
2.802	.9500	1.3242	10.590	[illegible]283
			±.56%	

properties of solids. The determination of the density of ice at elevated pressures required the isothermal bulk modulus, however, since the sample was maintained at the same temperature for all pressures. To convert the dynamic bulk moduli to isothermal bulk moduli, for the purpose of calculating the density at the elevated pressures, an expression used by Gammon[126] was employed. This expression, based on the mathematical relationships between the equations of elasticity and the equations of thermodynamics, discussed in detail by Huntington[133] and Nye,[134] is given for an arbitrary single crystal medium by,

$$s^T_{ijkl} = s^S_{ijkl} + \alpha_{ij}\alpha_{kl}T/(\rho C_P) \qquad (3\text{-}9)$$

where s^T and s^S denote the isothermal and adiabatic elastic compliance tensors, α is the thermal expansion tensor, T is the temperature (in K), ρ is the density, and C_P denotes the heat capacity at constant stress. This relation takes into account the contribution to the strain tensor of thermal expansion which arises from stress-induced temperature changes when stress is applied to a solid.

For the case of hexagonal ice crystals at -16°C, Gammon used Butkovich's[131] data on the thermal expansion tensor, and the heat capacity measurements of Giauque and Stout[135] to reduce the expression to,

$$s^T_{ij} = s^S_{ij} + .364 \times 10^{-12}\ m^2/N \qquad ij = 11,12,13,33$$
$$s^T_{44} = s^S_{44} \qquad (3\text{-}10)$$

He then calculated isothermal elastic constants, c^T_{ij}, from the isothermal compliance constants of (3-10) using the expressions given

below, adapted from Nye,[134] which relate the elastic and compliance constants.

$$
\begin{aligned}
c &= [(c_{11} + c_{12})\, c_{33} - 2c_{13}^2]^{1/2} \\
s_{11} &= (c_{11}c_{33} - c_{13}^2) \,/\, [c^2(c_{11} - c_{12})] \\
s_{12} &= (c_{13}^2 - c_{12}c_{33}) \,/\, [c^2(c_{11} - c_{12})] \\
s_{13} &= -c_{13} / c^2 \\
s_{33} &= (c_{11} + c_{12}) \,/\, c^2 \\
s_{44} &= 1/c_{44}
\end{aligned}
\tag{3-11}
$$

In the present analysis, the isothermal elastic constants, which were used to calculate the isothermal bulk modulus, were determined by simply multiplying each adiabatic parameter c_{ij}^S by the ratio c_{ij}^T/c_{ij}^S from Gammon's results. The appropriate ratios are,

$$
\begin{aligned}
c_{11}^T/c_{11}^S &= .98174 & c_{33}^T/c_{33}^S &= .98341 \\
c_{12}^T/c_{12}^S &= .96413 & c_{44}^T/c_{44}^S &= 1 \\
c_{13}^T/c_{13}^S &= .95646
\end{aligned}
\tag{3-12}
$$

The assumed form of the isothermal bulk modulus was,

$$B(P) = B_0 + B_1 P \tag{3-13}$$

where B_0 denotes the isothermal bulk modulus at zero pressure, B_1 is dB/dP, and P is the pressure. This expression was then used in the following integral to obtain the ice density.

$$\int_0^P \frac{1}{B}\, dP = \ln\left(\frac{\rho}{\rho_o}\right) \qquad (3\text{-}14)$$

Here ρ_o is the zero pressure density from (3-6) and ρ is the density at pressure P.

The preliminary densities and refractive indices of ice at the 6 elevated pressures were determined in this manner. These parameters were then used, along with the 6 sets of frequency shift data, to compute the elastic constants at each pressure. The constants were used to calculate isothermal bulk moduli, in the same manner described above, which were then least-squares quadratically fitted to the pressure, so that a more refined expression for the pressure dependence of the bulk modulus could be determined. This slightly improved version was then cycled through equation (3-14) to generate slightly different densities. The densities, in turn, were again used to compute 6 new sets of slightly improved elastic constants. This time, the general quadratic expression for the bulk modulus determined from the 6 new values, was able to reproduce the exact values of the densities used in the analysis. The result of this iterative procedure was a completely self consistent set of densities, refractive indices and elastic constants for ice Ih at 7 different pressures spanning the region of phase stability at -35.5°C (Tables 3.8 and 3.9). The elastic compliance constants, calculated using (3-11), are given in Table 3.10.

Figures 3.5 to 3.11 represent the distributions of Brillouin frequency shift data versus gamma, and Figures 3.12 to 3.18 the consequent acoustic velocities versus gamma angle, for the 7 pressures

TABLE 3.10

ELASTIC COMPLIANCE CONSTANTS FOR MENDENHALL GLACIAL ICE AT VARIOUS PRESSURES SPANNING THE REGION OF PHASE STABILITY

Phase: Ice Ih
Temperature: -35.5°C

Pressure (kbar)	Elastic Compliance Constants ($Mbar^{-1}$)				
	s_{11}	s_{12}	s_{13}	s_{33}	s_{44}
0.000	9.901 ±.42%	-4.114 ±.67%	-2.209 ±.45%	8.086 ±.34%	31.776 ±.22%
0.503	9.890 ±.89%	-4.192 ±1.6%	-2.218 ±.95%	8.018 ±.73%	31.918 ±.54%
1.006	9.882 ±.64%	-4.194 ±1.1%	-2.294 ±.67%	8.049 ±.53%	32.373 ±.36%
1.507	10.008 ±.65%	-4.382 ±1.0%	-2.337 ±.65%	8.073 ±.53%	32.425 ±.36%
2.006	9.971 ±.74%	-4.292 ±1.2%	-2.432 ±.72%	8.129 ±.60%	32.916 ±.43%
2.504	10.001 ±.88%	-4.482 ±1.4%	-2.360 ±.87%	7.983 ±.72%	32.862 ±.49%
2.802	10.062 ±.82%	-4.586 ±1.3%	-2.370 ±.80%	7.973 ±.67%	33.135 ±.46%

Figure 3.5. Data for Mendenhall glacial ice at zero pressure and -35.5°C. Measured Brillouin frequency shifts Ω (indicated by crosses) and calculated frequency shifts (indicated by solid curves) versus the angle γ between the crystal c (hexagonal) axis and the direction of sound propagation. Curves specified by least squares elastic constants via equation (1-5) (L), equation (1-6) (T_1) and equation (1-7) (T_2) along with the Brillouin equation (1-9). The empirical standard deviation in frequency shift measurements, σ, is .019 GHz.

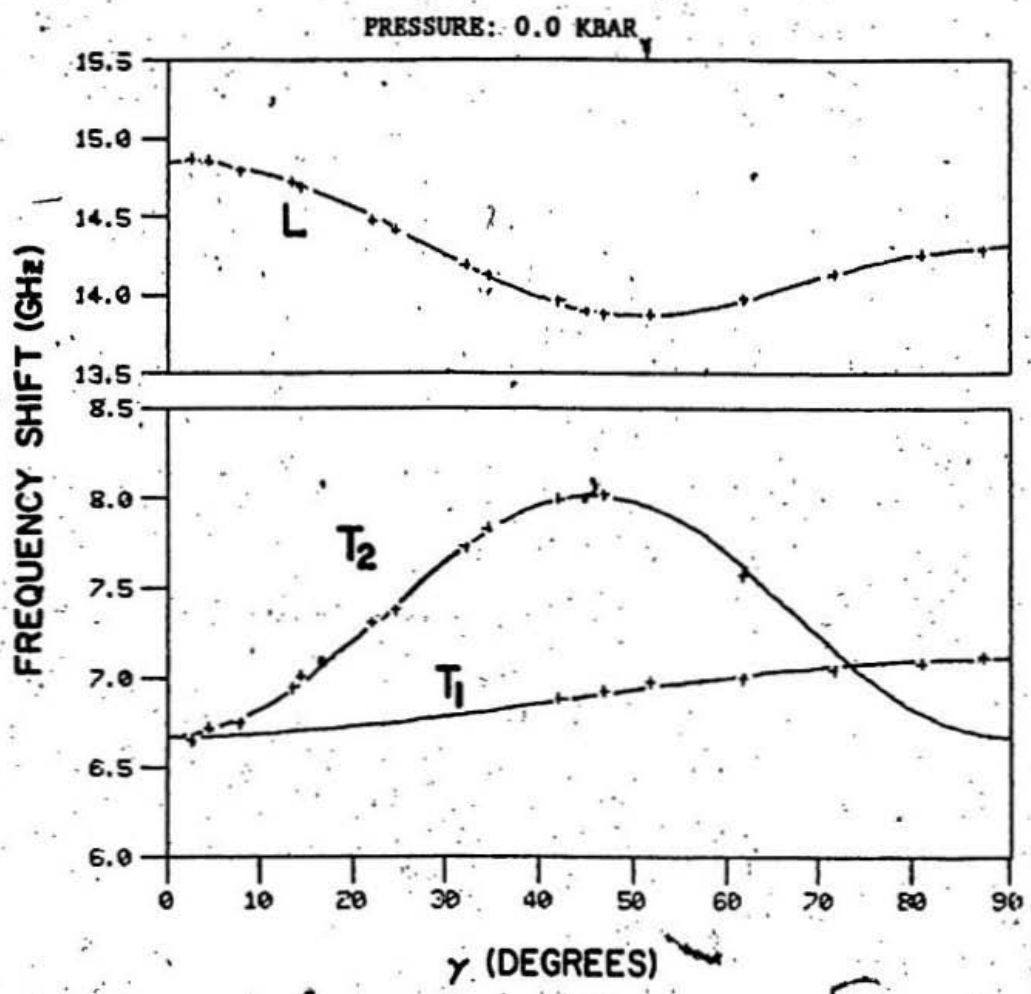
PRESSURE: 0.0 KBAR
FREQUENCY SHIFT (GHz)
15.5
15.0
14.5
14.0
13.5
L
8.5
8.0
7.5
7.0
6.5
6.0
T2
T1
0
10
20
30
40
50
60
70
80
90
γ (DEGREES)

Figure 3.5

Figure 3.6. Brillouin frequency shift versus γ for Mendenhall glacial ice at .503 kbar and -35.5°C. Curves identified as in Figure 3.5. The empirical standard deviation in frequency shift measurements is .040 GHz.

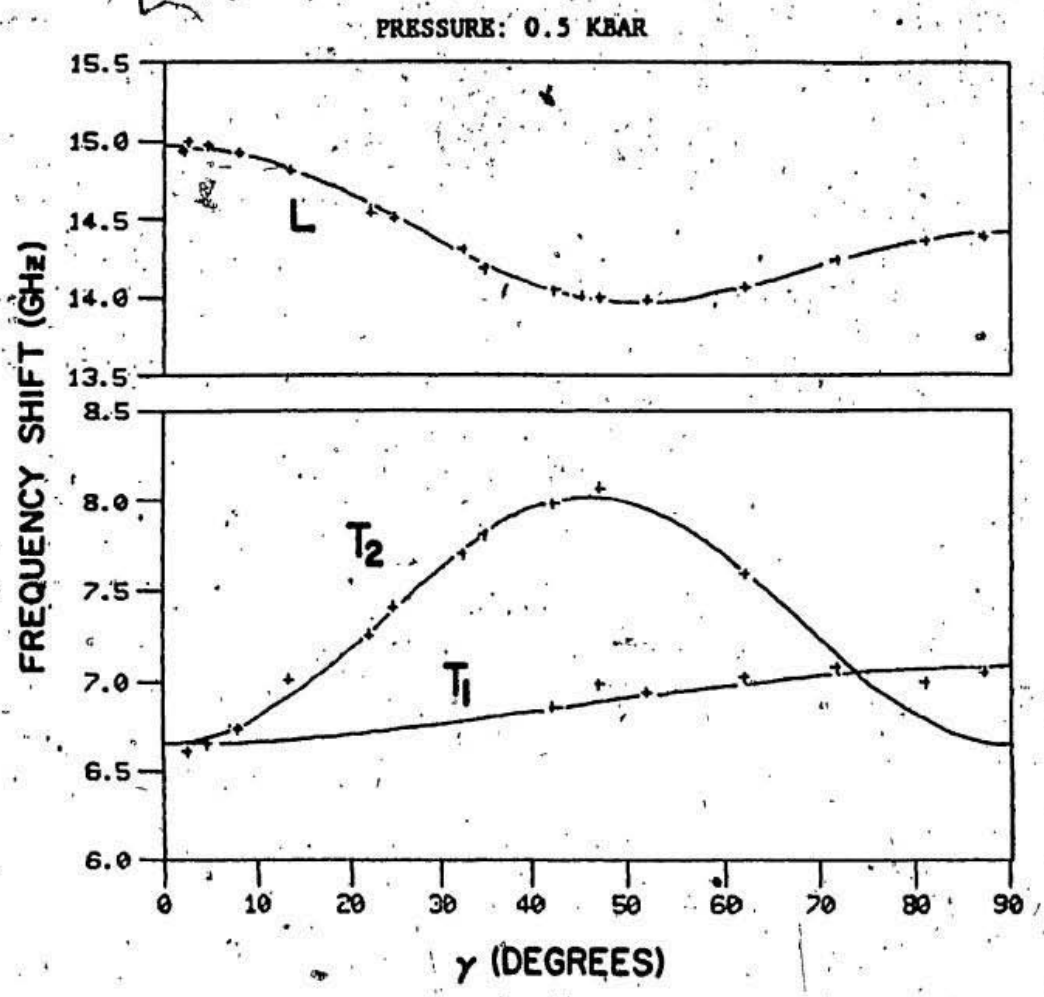
PRESSURE: 0.5 KBAR
15.5
15.0
14.5
14.0
13.5
L
8.5
8.0
7.5
7.0
6.5
6.0
T2
T1
FREQUENCY SHIFT (GHz)
0
10
20
30
40
50
60
70
80
90
γ (DEGREES)

Figure 3.6

Figure 3.7. Brillouin frequency shift versus γ for Mendenhall glacial ice at 1.006 kbar and -35.5°C. Curves identified as in Figure 3.5. The empirical standard deviation in frequency shift measurements is .028 GHz.

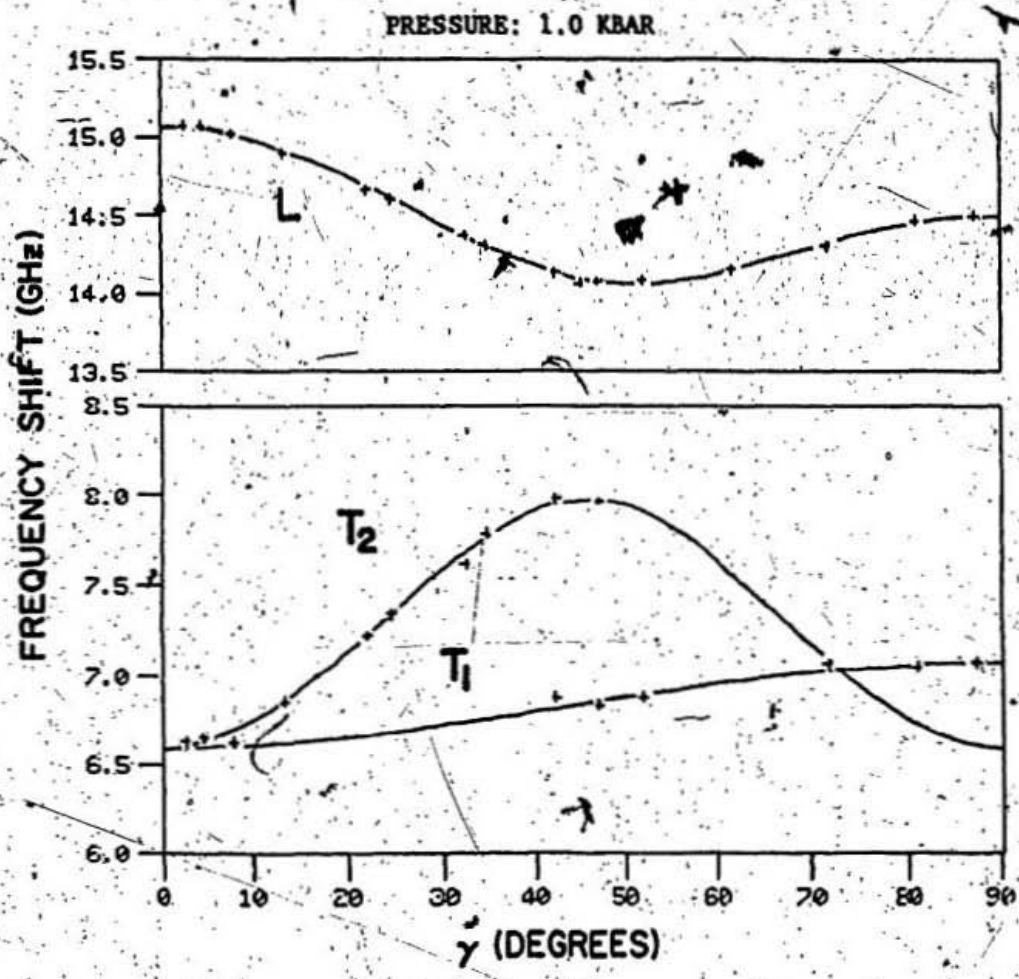
PRESSURE: 1.0 KBAR
FREQUENCY SHIFT (GHz)
15.5
15.0
14.5
14.0
13.5
L
8.5
8.0
7.5
7.0
6.5
6.0
T2
T1
0
10
20
30
40
50
60
70
80
90
γ (DEGREES)

Figure 3.7

Figure 3.8. Brillouin frequency shift versus γ for Mendenhall glacial ice at 1.507 kbar and -35.5°C. Curves identified as in Figure 3.5. The empirical standard deviation in frequency shift measurements is .030 GHz.

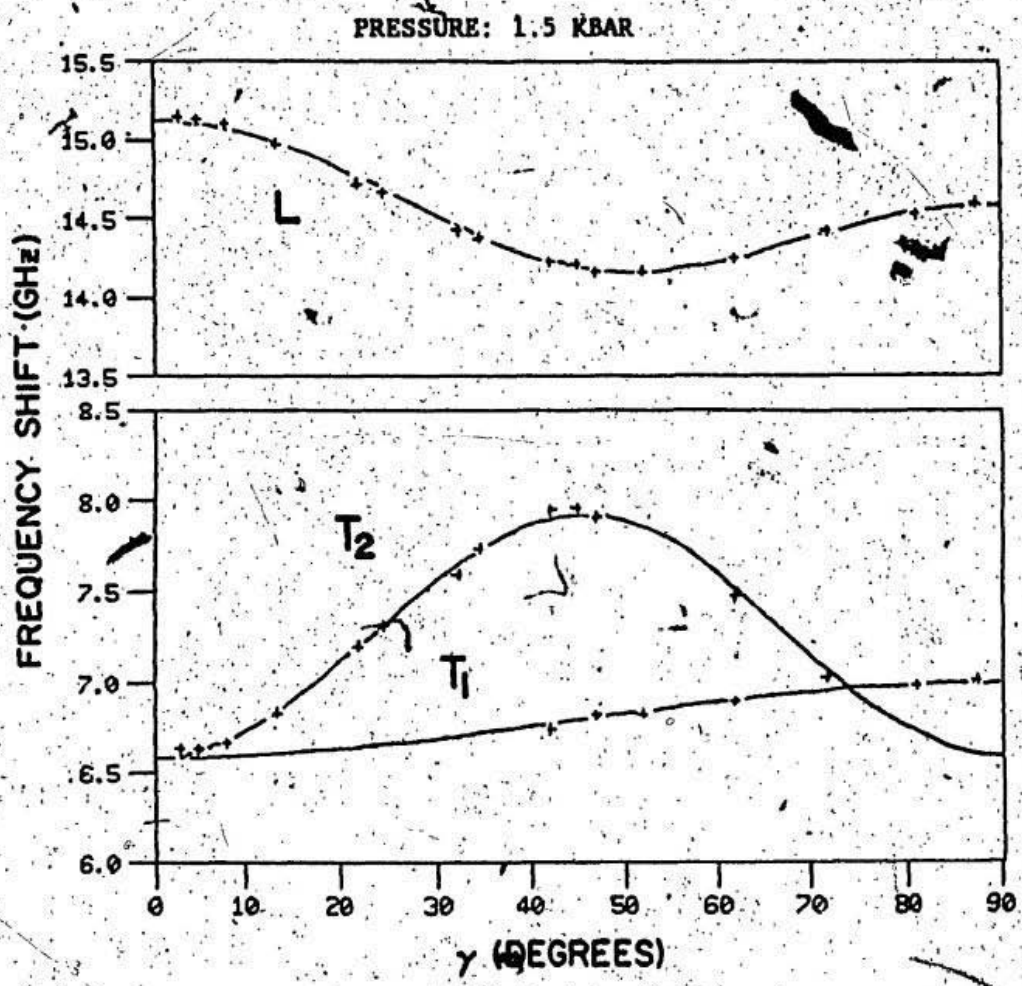
PRESSURE: 1.5 KBAR
FREQUENCY SHIFT (GHz)
15.5
15.0
14.5
14.0
13.5
L
8.5
8.0
7.5
7.0
6.5
6.0
T2
T1
0
10
20
30
40
50
60
70
80
90
γ (DEGREES)

Figure 3.8

Figure 3.9. Brillouin frequency shift versus γ for Mendenhall glacial ice at 2.006 kbar and -35.5°C. Curves identified as in Figure 3.5. The empirical standard deviation in frequency shift measurements is .034 GHz.

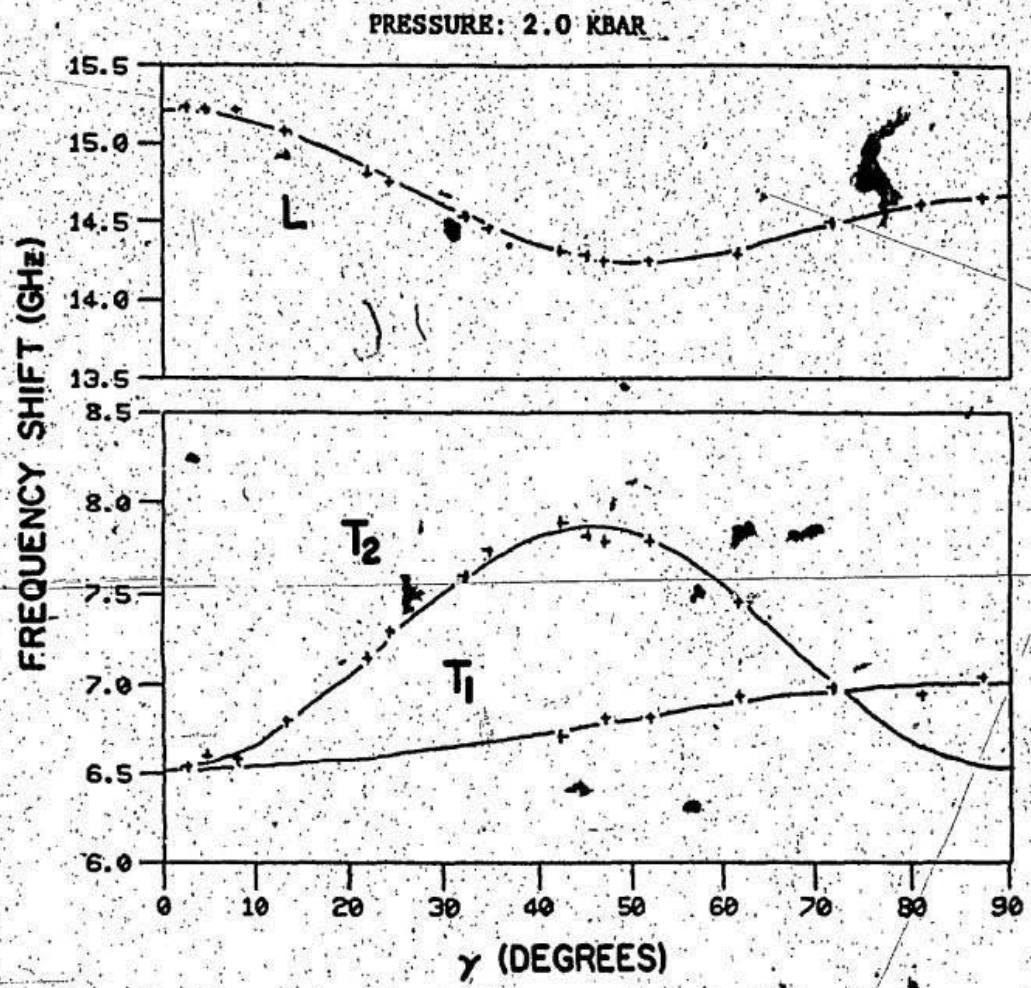
PRESSURE: 2.0 KBAR
FREQUENCY SHIFT (GHz)
15.5
15.0
14.5
14.0
13.5
L
8.5
8.0
7.5
7.0
6.5
6.0
T2
T1
0
10
20
30
40
50
60
70
80
90
γ (DEGREES)

Figure 3.9

Figure 3.10. Brillouin frequency shift versus γ for Mendenhall glacial ice at 2.504 kbar and -35.5°C. Curves identified as in Figure 3.5. The empirical standard deviation in frequency shift measurements is .039 GHz.

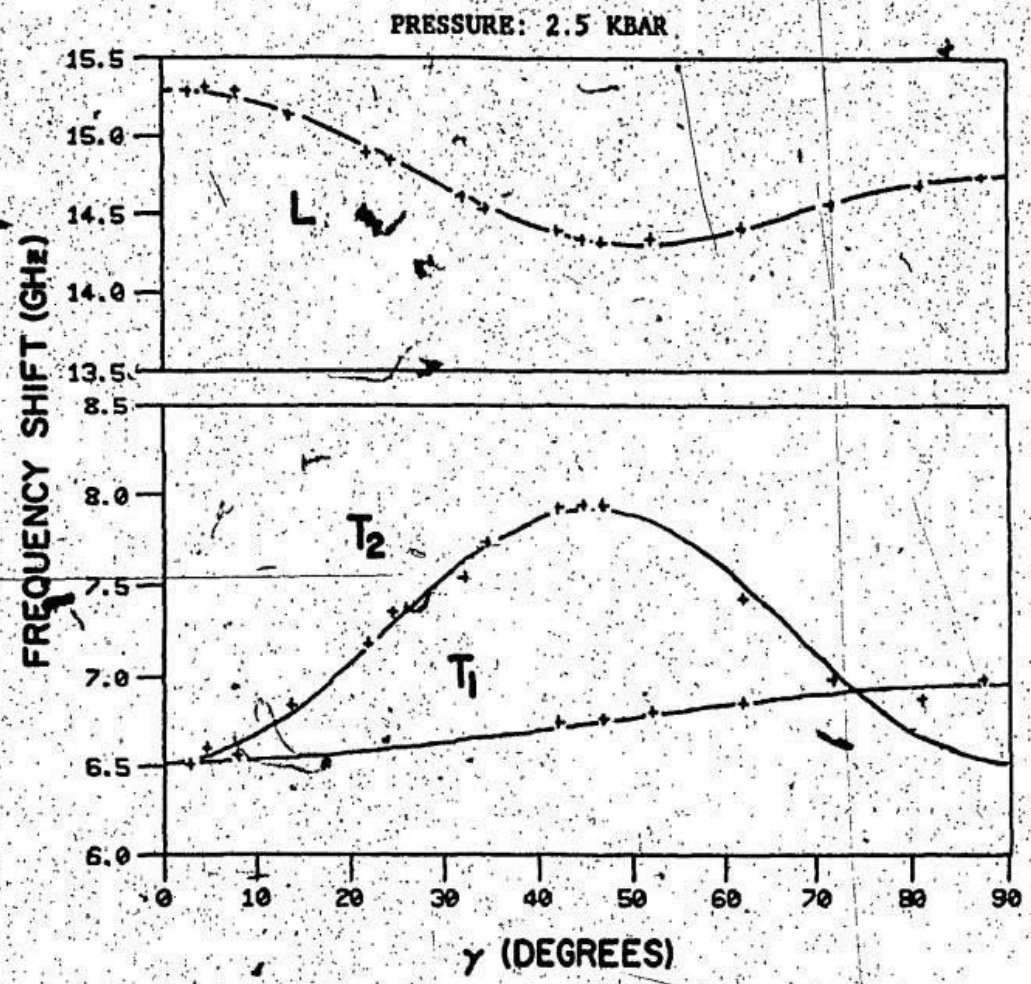
PRESSURE: 2.5 KBAR
15.5
15.0
14.5
14.0
13.5
L
8.5
8.0
7.5
7.0
6.5
6.0
T2
T1
FREQUENCY SHIFT (GHz)
0
10
20
30
40
50
60
70
80
90
γ (DEGREES)

Figure 3.10

Figure 3.11. Brillouin frequency shift versus γ for Mendenhall glacial ice at 2.802 kbar and -35.5°C. Curves identified as in Figure 3.5. The empirical standard deviation in frequency shift measurements is .037 GHz.

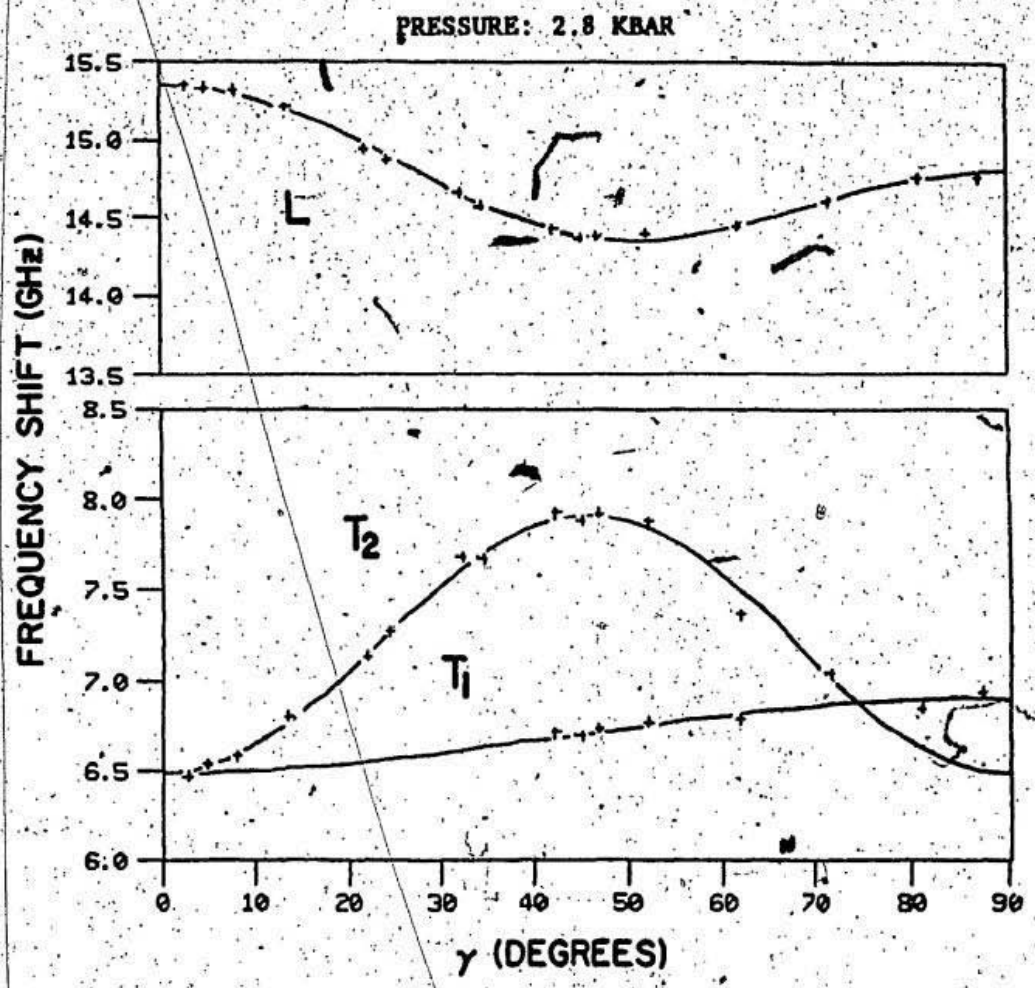
PRESSURE: 2.8 KBAR
15.5
15.0
14.5
14.0
13.5
L
8.5
8.0
7.5
7.0
6.5
6.0
T2
T1
FREQUENCY SHIFT (GHz)
0
10
20
30
40
50
60
70
80
90
γ (DEGREES)

Figure 3.11

Figure 3.12. Data for Mendenhall glacial ice at zero pressure and -35.5°C. Acoustic velocities (indicated by crosses), determined from measured frequency shifts (via the Brillouin equation (1-9)), and calculated velocities (indicated by solid curves) versus the angle γ between the crystal c (hexagonal) axis and the direction of sound propagation. Curves specified by least squares elastic constants via equation (1-5) (L), equation (1-6) (T_1) and equation (1-7) (T_2).

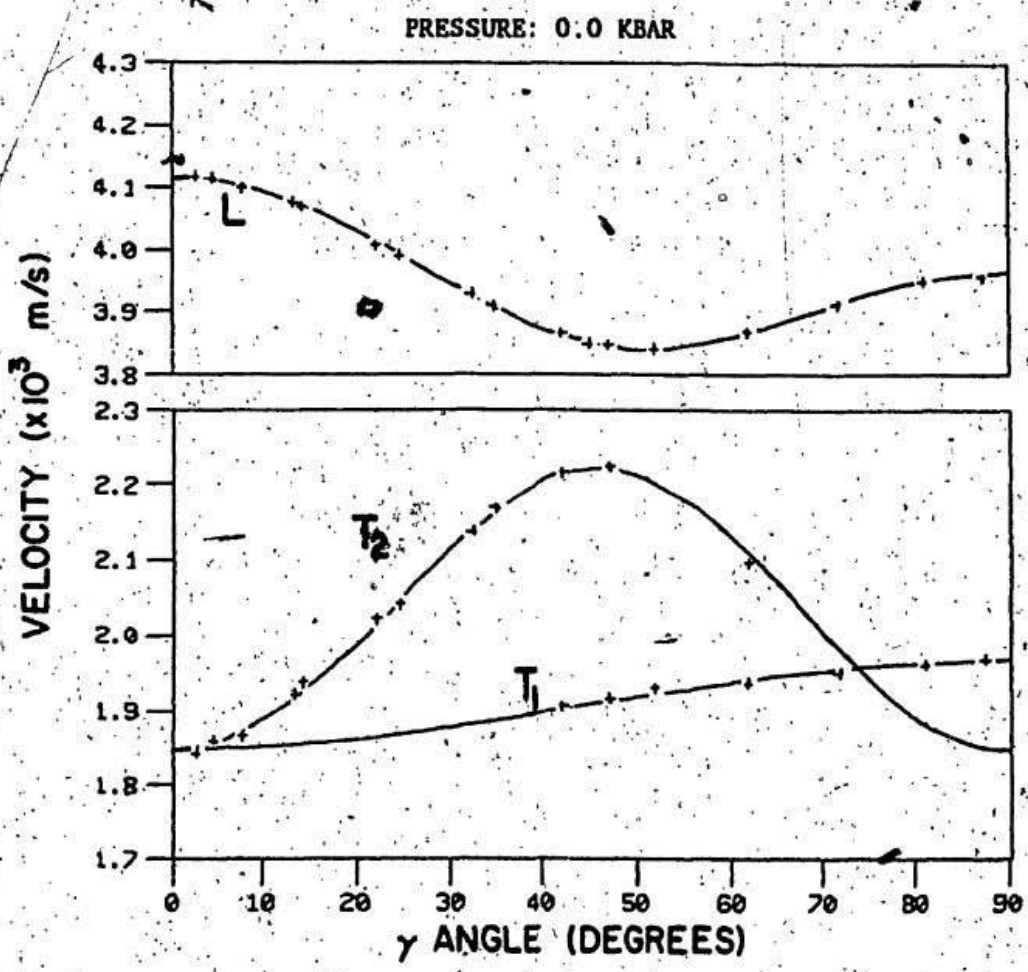
PRESSURE: 0.0 KBAR
VELOCITY (x10³ m/s)
4.3
4.2
4.1
4.0
3.9
3.8
L
2.3
2.2
2.1
2.0
1.9
1.8
1.7
T2
T1
0
10
20
30
40
50
60
70
80
90
γ ANGLE (DEGREES)

Figure 3.12

Figure 3.13. Acoustic velocity versus γ for Mendenhall glacial ice at .503 kbar and -35.5°C. Curves identified as in Figure 3.12.

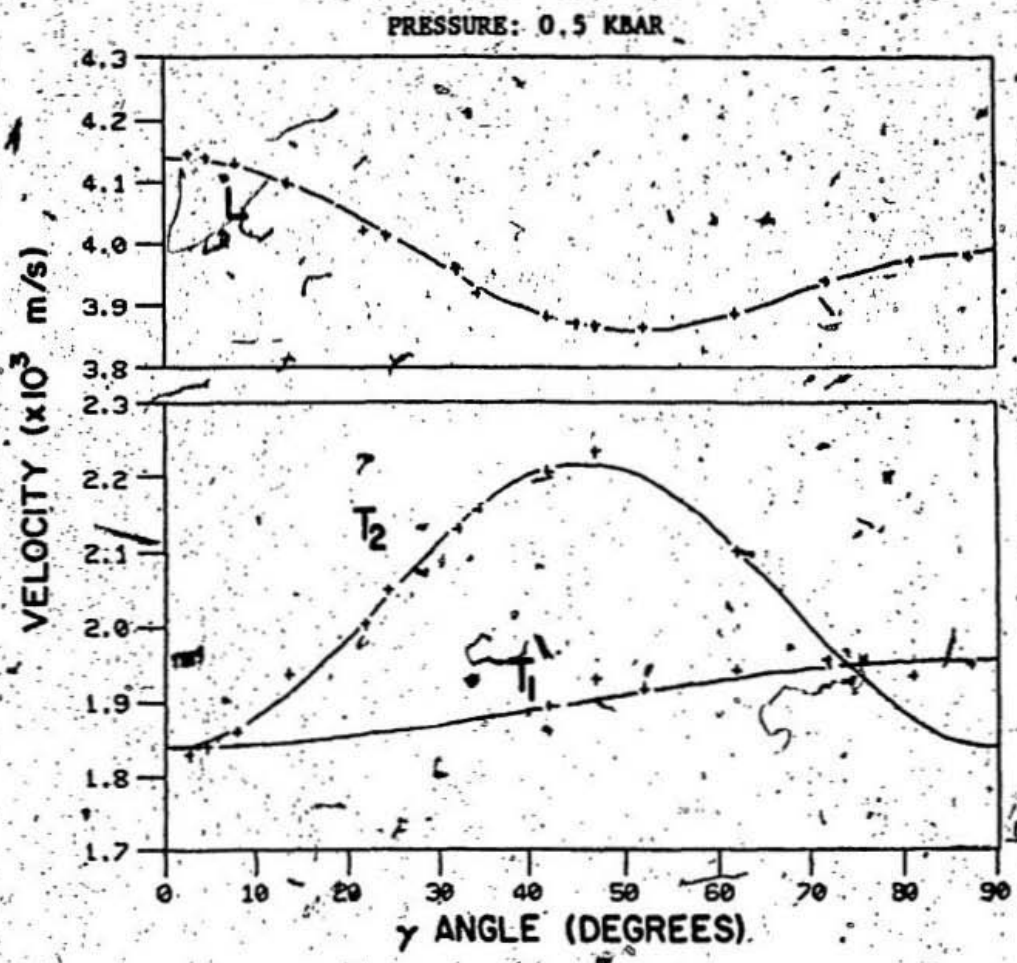
PRESSURE: 0.5 KBAR
VELOCITY (x10^3 m/s)
4.3
4.2
4.1
4.0
3.9
3.8
L
2.3
2.2
2.1
2.0
1.9
1.8
1.7
T2
T1
0
10
20
30
40
50
60
70
80
90
γ ANGLE (DEGREES)

Figure 3.13

Figure 3.14. Acoustic velocity versus γ for Mendenhall glacial ice at 1.006 kbar and -35.5°C. Curves identified as in Figure 3.12.

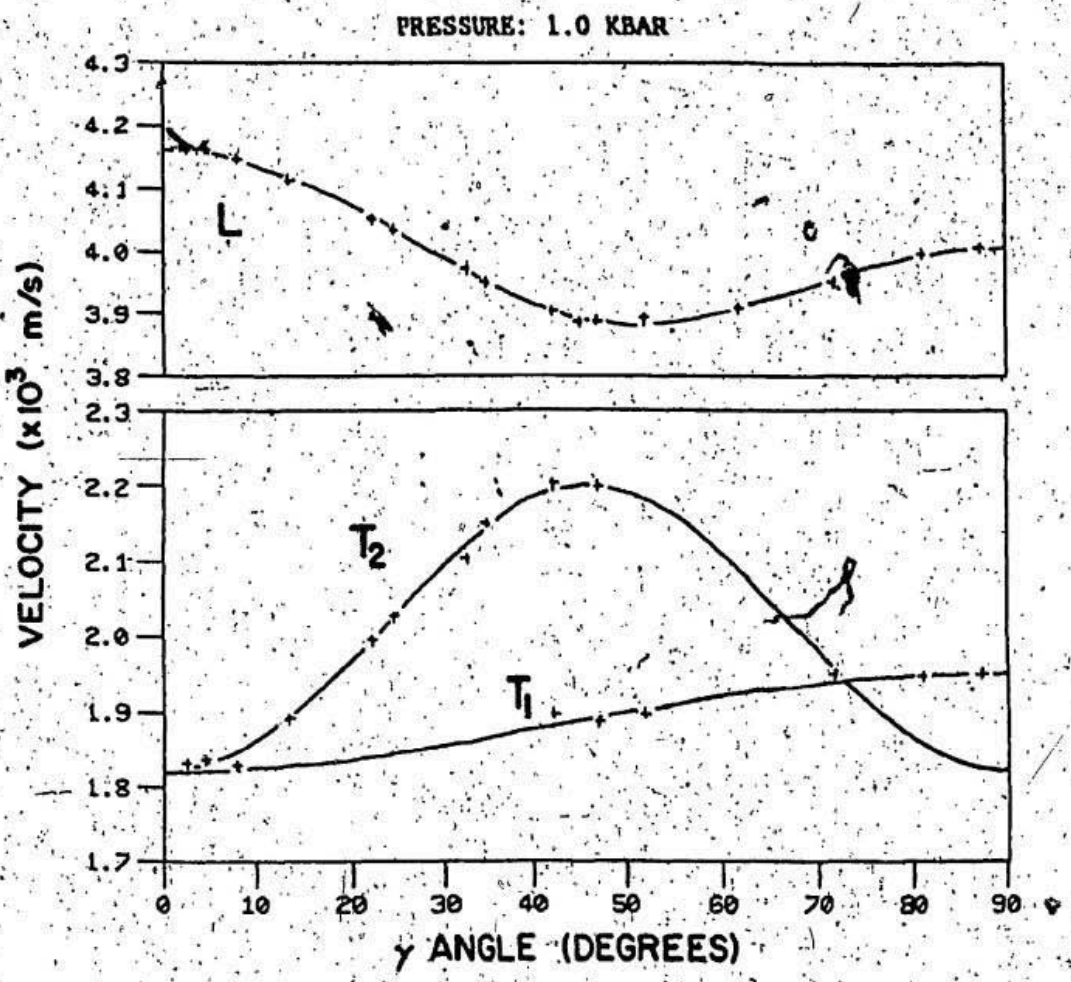
PRESSURE: 1.0 KBAR
VELOCITY (x10^3 m/s)
4.3
4.2
4.1
4.0
3.9
3.8
L
2.3
2.2
2.1
2.0
1.9
1.8
1.7
T2
T1
0
10
20
30
40
50
60
70
80
90
γ ANGLE (DEGREES)

Figure 3.14

Figure 3.15. Acoustic velocity versus γ for Mendenhall glacial ice at 1.507 kbar and -35.5°C. Curves identified as in Figure 3.12.

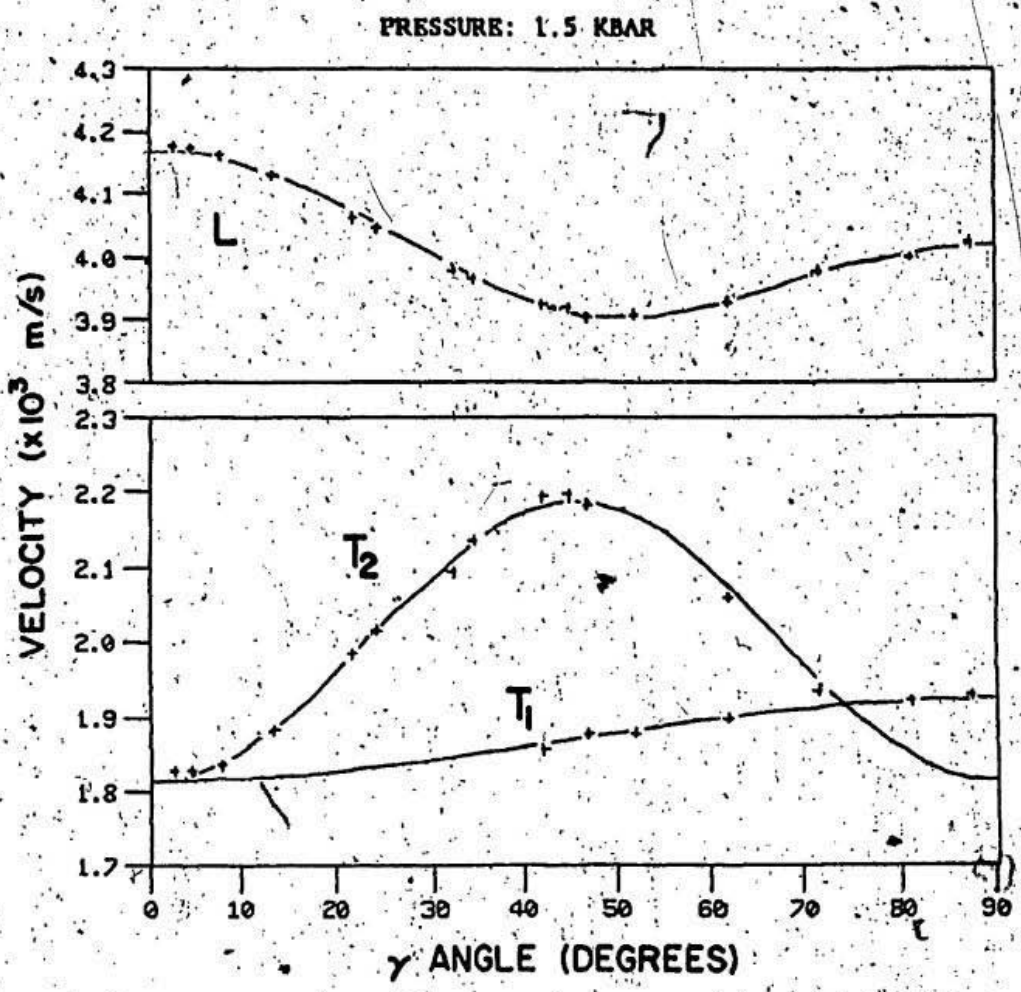
PRESSURE: 1.5 KBAR
VELOCITY (x10³ m/s)
4.3
4.2
4.1
4.0
3.9
3.8
L
2.3
2.2
2.1
2.0
1.9
1.8
1.7
T2
T1
0
10
20
30
40
50
60
70
80
90
γ ANGLE (DEGREES)

Figure 3.15

Figure 3.16. Acoustic velocity versus γ for Mendenhall glacial ice at 2.006 kbar and -35.5°C. Curves identified as in Figure 3.12.

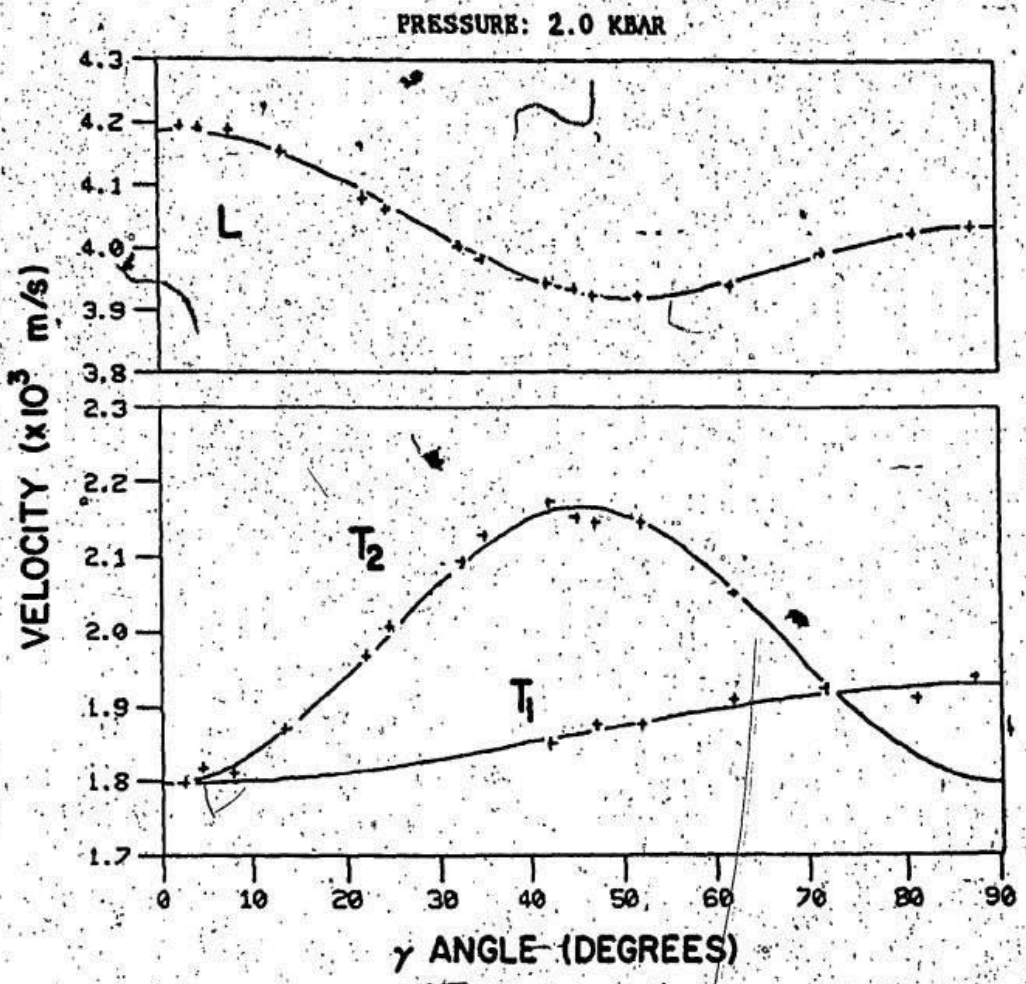
PRESSURE: 2.0 KBAR
VELOCITY (x10^3 m/s)
4.3
4.2
4.1
4.0
3.9
3.8
L
2.3
2.2
2.1
2.0
1.9
1.8
1.7
T2
T1
0
10
20
30
40
50
60
70
80
90
γ ANGLE (DEGREES)

Figure 3.16

Figure 3.17. Acoustic velocity versus γ for Mendenhall glacial ice at 2.504 kbar and -35.5°C. Curves identified as in Figure 3.12.

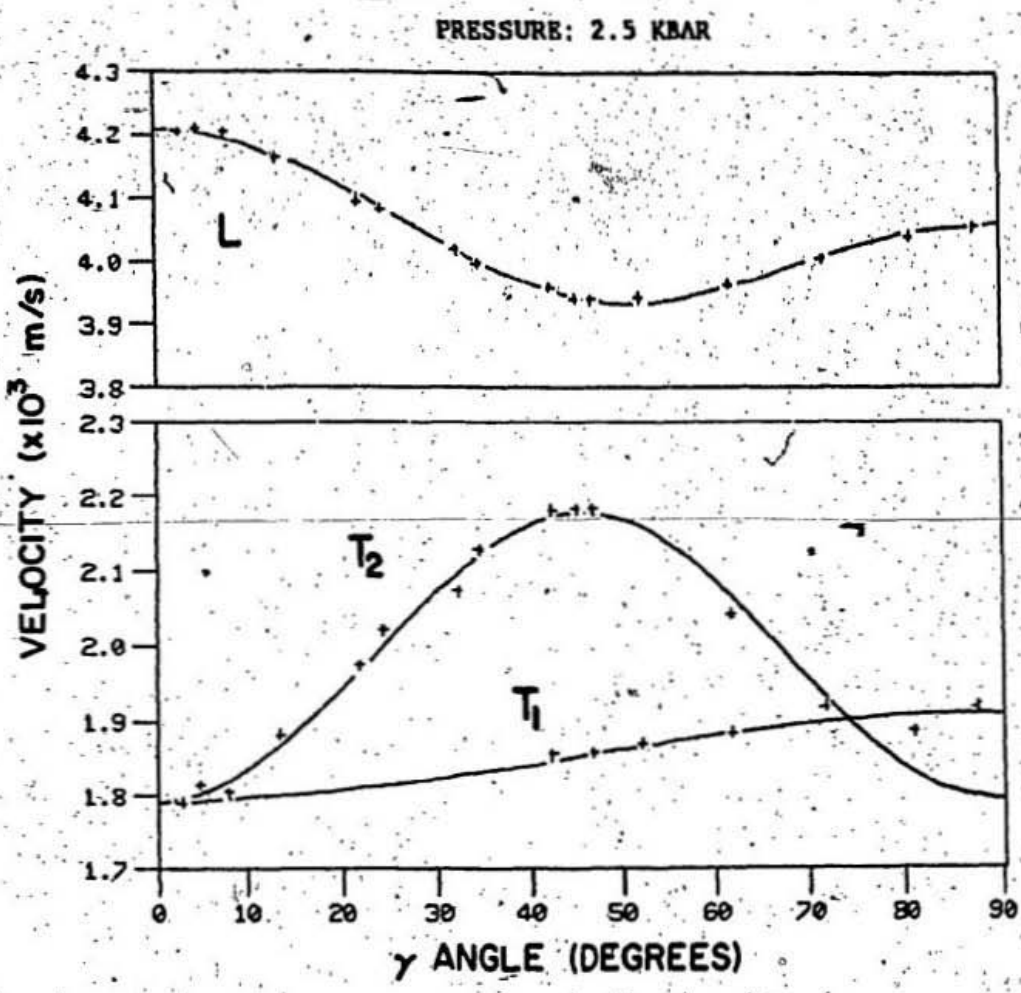
PRESSURE: 2.5 KBAR
VELOCITY (x10^3 m/s)
L
T2
T1
γ ANGLE (DEGREES)
4.3
4.2
4.1
4.0
3.9
3.8
2.3
2.2
2.1
2.0
1.9
1.8
1.7
0
10
20
30
40
50
60
70
80
90

Figure 3.17

Figure 3.18. Acoustic velocity versus γ for Mendenhall glacial ice at 2.802 kbar and -35.5°C. Curves identified as in Figure 3.12.

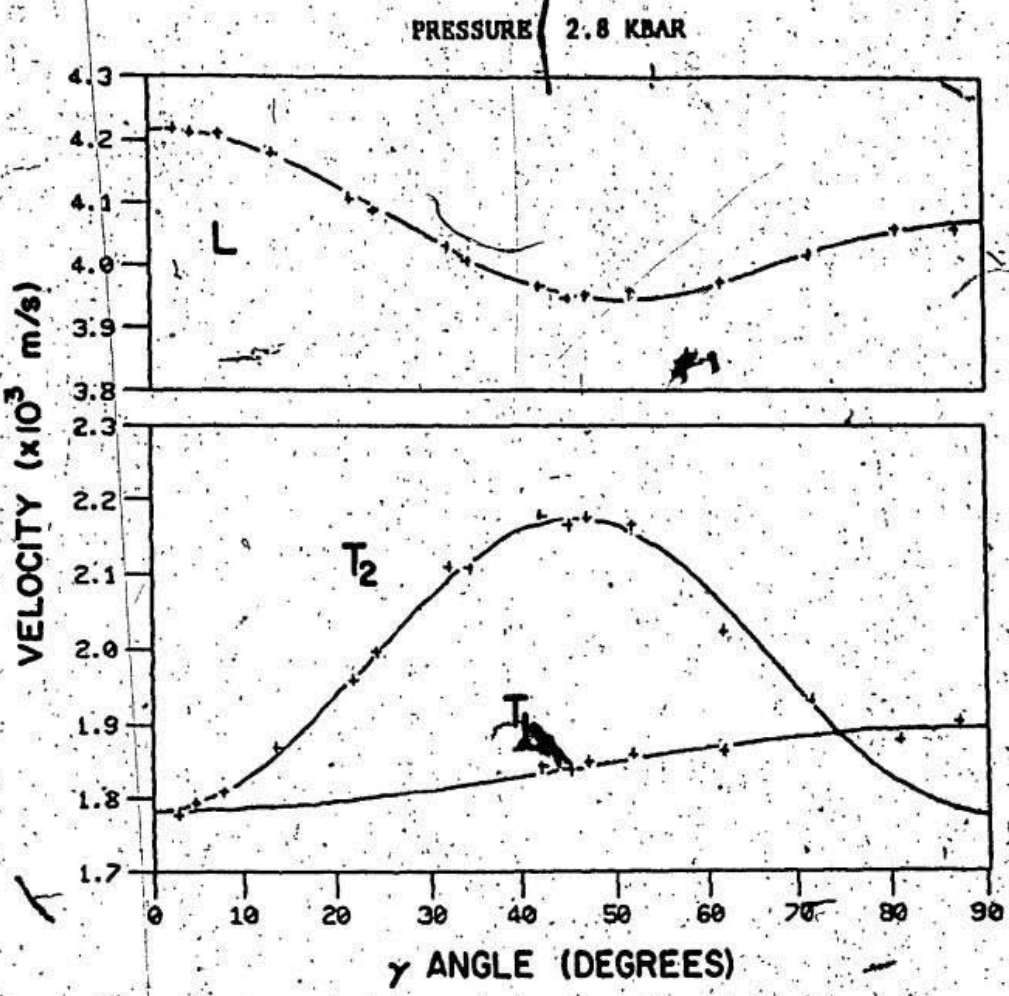
PRESSURE 2.8 KBAR
VELOCITY (x10^3 m/s)
4.3
4.2
4.1
4.0
3.9
3.8
L
2.3
2.2
2.1
2.0
1.9
1.8
1.7
T2
T1
0
10
20
30
40
50
60
70
80
90
γ ANGLE (DEGREES)

Figure 3.18

at which experiments were run. The curves correspond to the frequency shifts and velocities as calculated from the least squares elastic constants. Figures 3.19 and 3.20 are composites, included for comparison, which represent calculated frequency shifts and velocities for the full range of pressures. Figure 3.21 shows the percentage variation of each of the 5 elastic constants, based on data from Table 3.8, throughout the whole pressure range.

Tables 3.8 and 3.9 summarize the results from the entire set of experiments. All elastic parameters included in the tables are adiabatic values unless otherwise specified. The five elastic constants were least-squares quadratically fitted to the pressure so that reasonable values for all of them could be obtained at any pressure within the region of phase stability. Similar expressions were also derived for the density, the adiabatic and isothermal bulk moduli. These equations are given below.

$$c_{11}(P) = (14.495 + 4.665\times10^{-4}P - 1.350\times10^{-8}P^2)\times10^4 \text{ bar}$$

$$c_{12}(P) = (7.362 + 5.074\times10^{-4}P + 8.592\times10^{-9}P^2)\times10^4 \text{ bar}$$

$$c_{13}(P) = (5.929 + 6.419\times10^{-4}P - 5.249\times10^{-8}P^2)\times10^4 \text{ bar}$$

$$c_{33}(P) = (15.642 + 4.755\times10^{-4}P - 1.131\times10^{-8}P^2)\times10^4 \text{ bar}$$

$$c_{44}(P) = (3.151 - 5.662\times10^{-4}P + 3.692\times10^{-9}P^2)\times10^4 \text{ bar} \qquad (3\text{-}15)$$

$$\rho(P) = (.9228 + 1.0247\times10^{-5}P - 1.8869\times10^{-10}P^2) \text{ g/cm}^3$$

$$B^S(P) = (92296 + 5.5533\,P - 2.6104\times10^{-4}P^2) \text{ bar}$$

$$B^T(P) = (89684 + 5.3668\,P - 2.5215\times10^{-4}P^2) \text{ bar}$$

Figure 3.19. Brillouin frequency shifts, specified by least squares elastic constants via equation (1-5) (L), equation (1-6) (T_1) and equation (1-7) (T_2) along with the Brillouin equation (1-9), versus angle γ at pressure 0, 1.006, 2.006 and 2.802 kbar for Mendenhall glacial ice at -35.5°C.

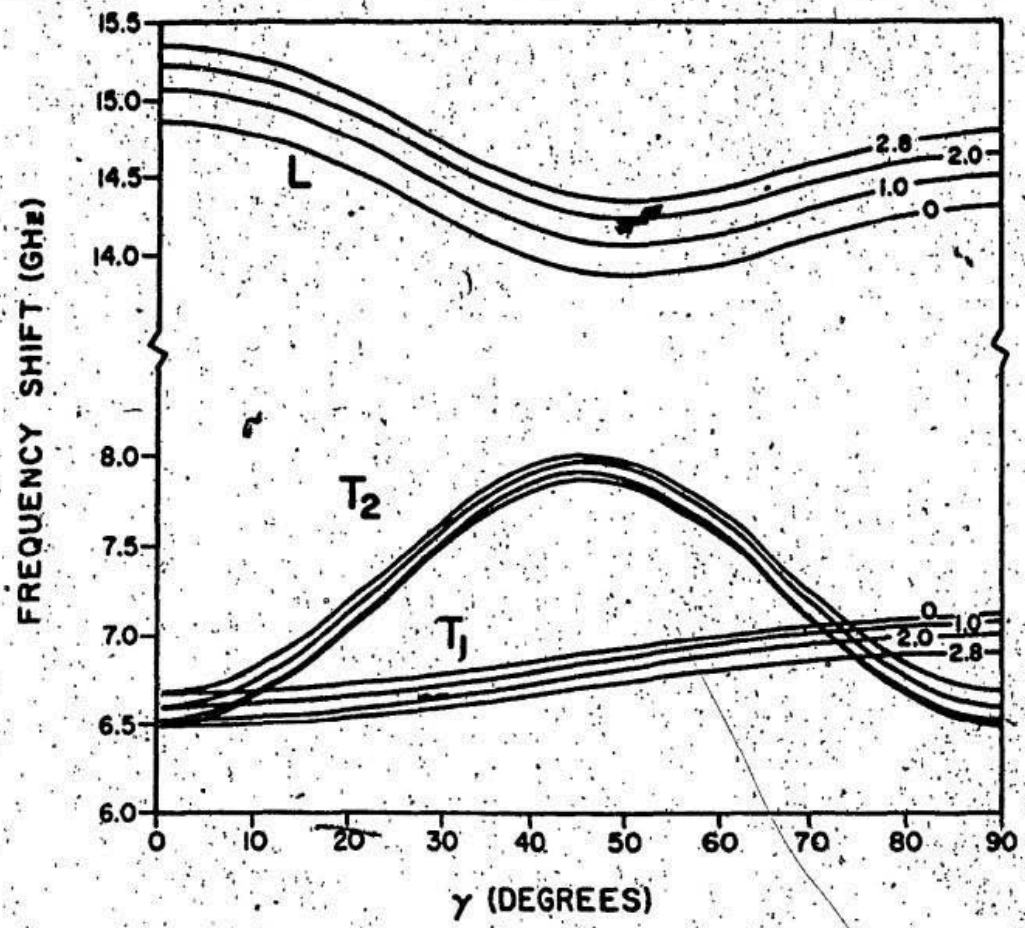
15.5
15.0
14.5
14.0
8.0
7.5
7.0
6.5
6.0
FREQUENCY SHIFT (GHz)
L
2.8
2.0
1.0
0
T2
T1
0
1.0
2.0
2.8
0
10
20
30
40
50
60
70
80
90
γ (DEGREES)

Figure 3.19

Figure 3.20. Velocities, for L (equation (1-5)), T_1 (equation (1-6)) and T_2 (equation (1-7)) acoustic modes, versus angle γ calculated from the 'best' fit elastic constants at pressure 0, 1.006, 2.006 and 2.802 kbar for Mendenhall glacial ice at -35.5°C.

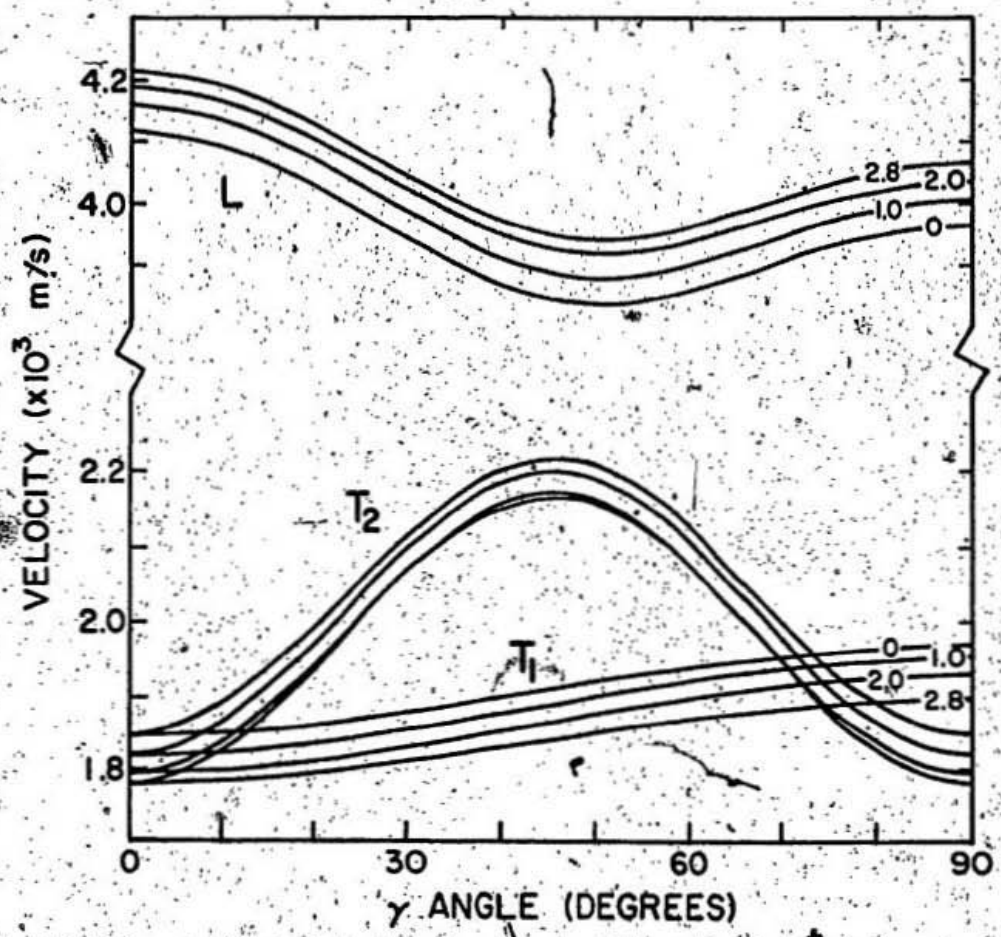
4.2
4.0
2.2
2.0
1.8
VELOCITY (x10³ m/s)
L
T2
T1
2.8
2.0
1.0
0
0
1.0
2.0
2.8
0
30
60
90
γ ANGLE (DEGREES)

Figure 3.20

Figure 3.21. Percentage change in elastic constants c_{11}, c_{12}, c_{13}, c_{33} and c_{44} versus pressure for Mendenhall ice at -35.5°C.

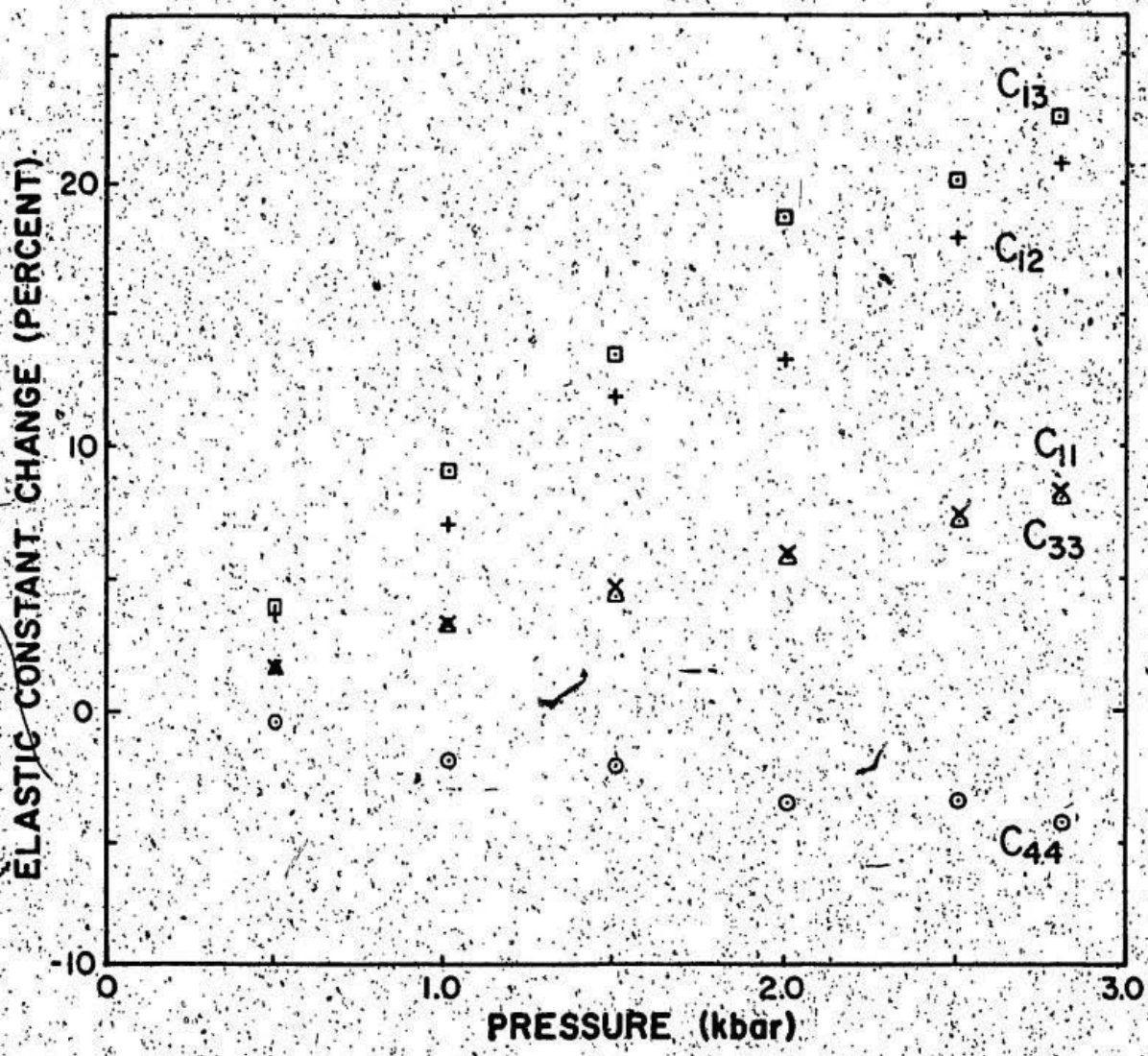
ELASTIC CONSTANT CHANGE (PERCENT)
20
10
0
-10
0
1.0
2.0
3.0
PRESSURE (kbar)
C13
C12
C11
C33
C44

Figure 3.21

In the equations above, P denotes pressure in bars, B^S denotes the adiabatic (constant entropy) bulk modulus, and B^T is the isothermal (constant temperature) bulk modulus.

3.5 Discussion of the Results and Comparison With Other Work

The only other study found in the literature which investigated the pressure dependence of the elastic constants of ice Ih was the work of Brockamp and Rüter.[114] These ultrasonic pulse transmission experiments were conducted on single crystals of ice to a maximum pressure of 400 bars, at -20.5°C. Longitudinal and transverse acoustic velocities were measured in three crystallographic directions; parallel and perpendicular to the c-axis, and at an angle of 45° to the c-axis.

The pressure dependences of the elastic constants from the study of Brockamp and Rüter are compared with the present results in Table 3.11. Values quoted from the present study were calculated from the expressions for the elastic constants (3-15) at a pressure of 1400 bar, which was the midpoint of the whole pressure range for which data was collected. The overall trends for the fractional increases in the elastic constants, $(1/c_{ij}(0))dc_{ij}/dP$, where $c_{ij}(0)$ denotes the zero pressure magnitude, were common to both sets of experiments, except that the relative magnitudes for c_{12} and c_{13} were interchanged. The overall magnitudes were in reasonable agreement, where the largest discrepancy was ~23% for $(1/c_{12}(0))\cdot dc_{12}/dP$, while the best agreement was ~1% for $(1/c_{11}(0))\cdot dc_{11}/dP$. The negative pressure dependence of c_{44} was also evident in both sets of data. According to Born[136] and Misra,[137] this negative pressure dependence was an indication of softening of the shear modes and decreasing crystal stability as the

TABLE 3.11

COMPARISON OF THE PRESENT RESULTS WITH ANOTHER STUDY OF THE PRESSURE DEPENDENCE OF THE ELASTIC CONSTANTS

ij	$\frac{1}{c_{ij}(0\ \text{bar})}\frac{dc_{ij}}{dP}$ (Mbar^{-1})		$\frac{dc_{ij}}{dP}$ (Dimensionless)	
	Brockamp and Rüter[11]	Present Results	Brockamp and Rüter	Present Results
11	29.8	29.6	4.09	4.29
12	88.5	72.2	5.96	5.31
13	76.3	83.5	3.96	4.95
33	24.8	28.4	3.70	4.44
44	-12.6	-14.7	-0.39	-0.46

phase transition to ice III was approached. Born argued that the second law of thermodynamics requires that the strain energy of any lattice must increase when the lattice is arbitrarily strained. In other words, the bulk and shear moduli can never vanish. Hence c_{44} must never vanish for first order phase transitions. Since c_{44} has a negative pressure derivative within ice Ih and it is never allowed to vanish, the phase must therefore become unstable and transform to some other structure before c_{44} goes to zero.

The present results are considered to be much more accurate than those of Brockamp and Rüter for two reasons. First of all, the frequency shift data were collected for 16 different directions relative to the c-axis of the ice crystals, spanning the whole range of γ angle from -0° to -90°, whereas the ultrasonic measurements were made for 3 crystallographic directions only. Secondly, in ultrasonic experiments the accuracy of the results is very sensitive to the quality of the acoustic coupling between the transducers and the specimen. This is especially true for shear waves. The coupling quality appreciably alters with the application of hydrostatic pressure, and this may influence the measured acoustic pulse travel times. This problem does not exist in Brillouin scattering experiments since the sound waves are generated spontaneously as a result of the thermal energy of the ice specimens rather than by transducers, and furthermore, frequency shifts are measured rather than travel times.

The temperature corrected elastic constants at zero pressure, determined from the present experiments, are compared with the results of Gammon et al.,[112,113] for ice at -3°C and -16°C, in Table 3.12. Brillouin light scattering experiments were used for all three sets of

TABLE 3.12

COMPARISON OF THE PRESENT RESULTS AT ZERO PRESSURE, CORRECTED TO -3°C and -16°C, WITH OTHER BRILLOUIN SCATTERING ICE STUDIES

Author(s)	Temperature (°C)	Elastic Constants (x 10^4 bar)				
		c_{11}	c_{12}	c_{13}	c_{33}	c_{44}
Gammon et al.[112] (1980)	-3	13.696	6.966	5.628	14.702	2.959
Present[a]	-3	13.766	6.985	5.669	14.852	2.991
Present[b]	-3	13.849	6.917	5.624	14.896	3.005
Gammon et al.[113] (1983)	-16	13.929	7.082	5.765	15.010	3.014
Present[a]	-16	14.099	7.154	5.806	15.211	3.063
Present[b]	-16	14.110	7.096	5.761	15.200	3.065

Note: Present[a] refers to the present results, which were temperature adjusted by using the experimentally determined temperature dependence of the frequency shifts (described in this section). Present[b] refers to the present data, which were temperature corrected using Dantl's[108] expressions for the temperature dependences of the elastic constants.

results. Two means of temperature correction were used to adjust the present data to the temperatures of the other two studies. One method was to use the quadratic temperature adjustment expressions for each elastic constant derived by Dantl,[108] using ultrasonics. The other technique was to determine the temperature dependence of the frequency shifts by conducting light scattering experiments at various temperatures, for one particular setting of angle γ, and then computing the elastic constants from suitably temperature corrected frequency shift data previously obtained at -35.5°C and zero pressure, assuming that the same fractional shift variations applied for all values of γ. The expression below is a quadratic fit to the frequency shift-versus-temperature data, obtained from a Mendenhall sample, given in Table 3.13.

$$\Omega_L(T) = 13.636 - 1.387 \times 10^{-2}\ T - 9.586 \times 10^{-5}\ T^2 \qquad (3\text{-}16)$$

In the expression above, Ω_L denotes longitudinal frequency shift in GHz and T is the temperature in degrees Celcius. Figure 3.22 is a graphical representation of the data given in Table 3.13. The solid curve corresponds to expression (3-16).

The data in Table 3.13 were obtained by orienting a sample to one particular value of γ, then applying and maintaining a pressure of 500 bars, and recording the frequency shift as the temperature was incrementally raised from ~-35°C to ~-4°C, allowing sufficient time for the system to reach thermal equilibrium at each step. It was tacitly assumed, when this latter method was used to temperature correct the elastic constants, that their ratios did not vary with temperature. This assumption has been shown to be valid, within experimental

TABLE 3.13

TEMPERATURE DEPENDENCE OF THE BRILLOUIN FREQUENCY SHIFT IN HEXAGONAL ICE AT CONSTANT PRESSURE AND FIXED ORIENTATION

Pressure: 500 bar
Sample c-axis orientation: $\gamma \approx 47^0$

Temperature of Sample (^{0}C)	Longitudinal Frequency Shift (GHz)
-35.56	14.01
-31.13	13.97
-27.08	13.94
-21.45	13.90
-16.47	13.84
-12.06	13.78
-8.65	13.75
-6.04	13.71
-4.17	13.70

Figure 3.22. Temperature dependence of Brillouin frequency shift for Mendenhall glacial ice at .5 kbar and c-axis orientation $\gamma \approx 47^0$. The diameter of the open circles is comparable to the standard deviation of the frequency shift measurements. The solid curve represents the least squares fit to the data given by equation (3-16).

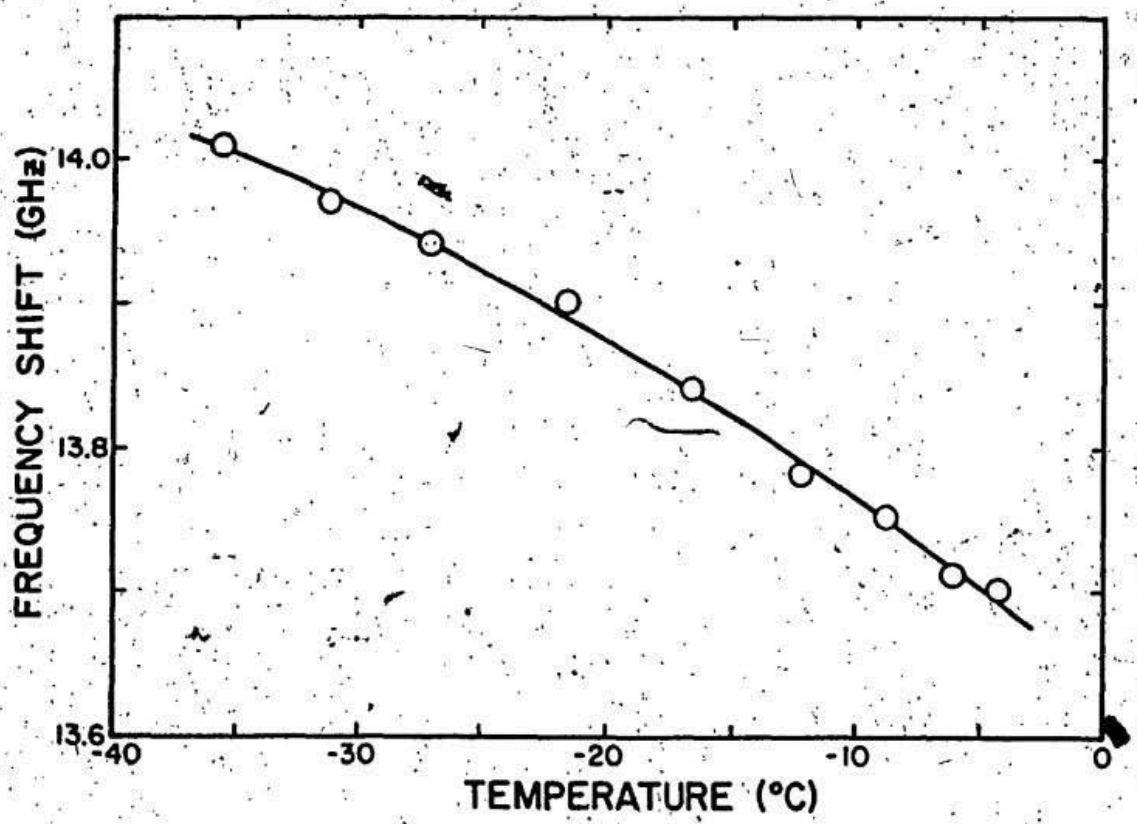

Figure 3.22

uncertainty, in the results of Gammon[126] over the range -16°C to -3°C. The present frequency shift data obtained at zero pressure and -35.5°C were adjusted to 9 temperatures spanning the range -3°C to -35.5°C using expression (3-16). A complete set of elastic constants was then generated for each temperature. The 9 values for each elastic constant and the associated adiabatic and isothermal bulk moduli were least squares fitted to the temperature to yield the quadratic temperature dependence expressions given below.

$$c_{11}(T)=(13.681 - 2.894\times10^{-2}T - 1.783\times10^{-4}T^2)\times10^4 \text{ bar}$$

$$c_{12}(T)=(6.942 - 1.467\times10^{-2}T - 9.036\times10^{-5}T^2)\times10^4 \text{ bar}$$

$$c_{13}(T)=(5.634 - 1.192\times10^{-2}T - 7.312\times10^{-5}T^2)\times10^4 \text{ bar}$$

$$c_{33}(T)=(14.761 - 3.113\times10^{-2}T - 1.895\times10^{-4}T^2)\times10^4 \text{ bar} \qquad (3\text{-}17)$$

$$c_{44}(T)=(2.973 - 6.287\times10^{-3}T - 3.896\times10^{-5}T^2)\times10^4 \text{ bar}$$

$$B^S(T)=(8.727 - 1.840\times10^{-2}T - 1.122\times10^{-4}T^2)\times10^4 \text{ bar}$$

$$B^T(T)=(8.480 - 1.789\times10^{-2}T - 1.094\times10^{-4}T^2)\times10^4 \text{ bar}$$

In the expressions above B^S and B^T are the adiabatic and isothermal bulk moduli respectively. The temperature T is in degrees Celcius.

The elastic constants of the present work were greater than those of Gammon et al.,[112,113] Table 3.12, regardless of which temperature correction method was employed. The reason for this was not clear. All the optical elements in the scattering setup were checked for alignment on numerous occasions. Also, the system yielded consistent frequency shift results on a rectangular piece of fused quartz which was used as

a standard in various Brillouin experimental setups besides the one used on ice. The high pressure cell and cryostat were rotated by 180° so that experiments could be run with the other horizontal view port facing the optical system in order to check the geometry of the cell windows by noting whether there were any frequency shift discrepancies at this new orientation. There were none. Finally, the temperature at which experiments were carried out was carefully checked by placing a diode thermistor inside the cell chamber to compare with the reading taken on the outside of the cell. It was subsequently discovered that a slight temperature gradient was present. A reading of -33°C on the outside corresponded to an actual reading of -35.5°C on the inside. This was probably the combined effect of radiative heating and also heating by conductive transfer through the very light partial atmosphere in the vacuum space inside the cryostat. Consequently, the temperature readings on the outside of the cell were calibrated against those on the inside, in the range -5°C to -40°C, so that the true temperature was always known during the experiments.

The other possible source of error that might explain the discrepancy between the present results and those of Gammon et al.[11,11s] was that there was error in their scattering geometry. Their results for ice at -16°C, which yielded the largest discrepancies when compared to the present results, were obtained from irregular shaped samples placed in a refractive index matching liquid, whereas the data for -3°C were obtained from grown cylindrical specimens and were in better agreement with the present values. In the former case the index match may not have been perfect. Unfortunately it was not feasible to verify this hypothesis. In any case, the values for the elastic

constants from all three sets of experiments were still in agreement to within ~1% on average.

3.6 Elastic Properties of Polycrystalline Aggregates

The analysis of the propagation of elastic waves through polycrystalline aggregates must take into account the various sizes, shapes, and orientations of the crystallites that comprise the medium. This is inherently difficult, and further complicated by the fact that when an elastic wave passes through such a medium, within a given region which is comprised of several crystallites of differing orientation, neither uniform strain nor uniform stress prevails. The situation where uniform strain is assumed has been treated mathematically by Voigt,[99] and Reuss[115] has dealt with the situation of assumed uniform stress, though the reality is somewhere in between.

In the present work a good estimate was obtained for the velocity of longitudinal acoustic waves in aggregates, comprised of tiny uniformly shaped and uniformly oriented crystallites, by suitably averaging the velocities over the complete range of propagation direction available within a crystal.

In the present Brillouin experimental setup the elastic waves, or phonons, which scatter light into the optical system have a fixed direction of propagation in the lab frame of reference. The c-axis of randomly oriented crystallites within a polycrystalline sample may make an angle γ with the phonon direction, anywhere between 0° and 90°. The sample may be rotated about the phonon propagation direction without altering γ. Therefore the likelihood of the c-axis of any crystallite being at an angle γ with the propagation vector is just the element of

solid angle $d\Omega = 2\pi \sin\gamma d\gamma$, divided by the total solid angle $\Omega = 4\pi$, since a crystallite may be oriented with equal likelihood anywhere on the solid sphere. Hence the average longitudinal velocity, $\overline{V}_L$, throughout a sample comprised of these small crystallites can be expressed by the integral,

$$\overline{V}_L = \frac{1}{4\pi} \int_0^{2\pi} V_L(\gamma) d\Omega = \int_0^{\pi/2} V_L(\gamma) \sin\gamma d\gamma \qquad (3\text{-}18)$$

This was evaluated numerically using Simpson's rule and the 7 sets of predetermined elastic constants to obtain values of $\overline{V}_L$ for ice Ih, at -35.5°C, for all of the pressures at which experiments were conducted. The results produced by this analysis for polycrystalline samples were experimentally verified by conducting Brillouin experiments on actual polycrystalline aggregates, at zero pressure, produced using the method described in Section 4.2. The mean velocity, $\overline{V}_L = 3.926$ km/s, determined from the results of 4 experiments on three such samples, was in excellent agreement with the calculated value, 3.914 km/s.

Various elastic parameters can be derived for homogeneous, polycrystalline aggregates from the theoretical equations which link the elastic constants of isotropic media. These relationships have been discussed in numerous texts including those of Landau and Lifshitz,[138] Nye[134] and Malvern.[139] The bulk modulus B, which is the same for single crystals of ice Ih as for aggregates since the linear compressibility is nearly isotropic,[126] can be used along with the average longitudinal velocity $\overline{V}_L$ and the density ρ to derive the Lamé constants, λ and μ, Young's modulus E, Poisson's ratio σ and the shear wave velocity $\overline{V}_T$, for polycrystalline aggregates.

The main linking equations are,

$$B = \lambda + 2\mu/3$$

$$\rho\bar{V}_L^2 = \lambda + 2\mu$$

$$E = 9B\mu/(3B+\mu) \qquad (3\text{-}19)$$

$$\sigma = ((3B/\mu-2)/(3B/\mu+1))/2$$

$$\bar{V}_T = (\mu/\rho)^{1/2}$$

Table 3.14 summarizes the results of the analysis for the 7 pressures at which Brillouin experiments on ice Ih were conducted. Based on the uncertainties associated with the refractive index, the scattering angle and the frequency shifts, the estimated uncertainties for the longitudinal and transverse velocities are .5% and .8% respectively. The data for $\bar{V}_L$ and $\bar{V}_T$ in the table have been least-squares quadratically fitted to yield the following expressions for the velocities at any pressure in the region of phase stability.

$$\bar{V}_L(P) = 3.914 + 4.516 \times 10^{-5}\, P - 3.083 \times 10^{-9}\, P^2$$

$$\bar{V}_T(P) = 1.997 - 2.495 \times 10^{-5}\, P + 1.083 \times 10^{-9}\, P^2 \qquad (3\text{-}20)$$

Here P denotes pressure in bars and the velocity is in km/s.

Figure 3.23 illustrates the behaviour of the averaged longitudinal and transverse velocities as a function of pressure. Note in particular that $\bar{V}_T$ decreased with pressure which clearly indicated, as previously mentioned, decreasing crystal stability. The solid lines drawn through the points correspond to (3-20). The data from Table 3.14 have also

TABLE 3.14

AVERAGED POLYCRYSTALLINE (ISOTROPIC) VELOCITIES AND ELASTIC PARAMETERS FOR ICE Ih AT VARIOUS PRESSURES SPANNING THE REGION OF PHASE STABILITY

Temperature: -35.5°C

Pressure (bar)	$\bar{V}_L$ ±.5% (km/s)	$\bar{V}_T$ ±.8% (km/s)	μ (x10^3 bar)	E (x10^3 bar)	λ (x10^3 bar)	σ
0	3.914	1.995	36.74	97.33	67.89	.32442
503	3.936	1.988	36.69	97.49	70.39	.32870
1006	3.958	1.975	36.40	97.11	73.32	.33414
1507	3.976	1.960	36.01	96.48	76.21	.33955
2006	3.991	1.948	35.78	96.14	78.61	.34362
2504	4.007	1.945	35.83	96.45	80.48	.34598
2802	4.018	1.935	35.58	96.00	82.18	.34893

Note: $\bar{V}_L$ and $\bar{V}_T$ are the averaged longitudinal and transverse velocities; μ is the shear modulus, E denotes Young's modulus, λ is a Lamé constant and σ is Poisson's ratio.

been used to obtain least square fits similar to (3-20), given below, for the other elastic parameters.

$$\mu(P) = 36.826 - 5.308 \times 10^{-1}\, P + 3.385 \times 10^{-2}\, P^2$$

$$E(P) = 97.520 - 6.068 \times 10^{-1}\, P + 2.888 \times 10^{-2}\, P^2$$

$$\lambda(P) = 67.740 + 5.912\, P - 2.841 \times 10^{-1}\, P^2 \qquad (3\text{-}21)$$

$$\sigma(P) = .32396 + 1.1305 \times 10^{-2}\, P - 8.8321 \times 10^{-4}\, P^2$$

Here the elastic parameters μ, E and λ and the pressure P are in kbar.

Figure 3.23. Percentage change in the calculated "mean" longitudinal and transverse acoustic velocities, as expected in polycrystalline aggregates, versus pressure for Mendenhall ice at -35.5°C.

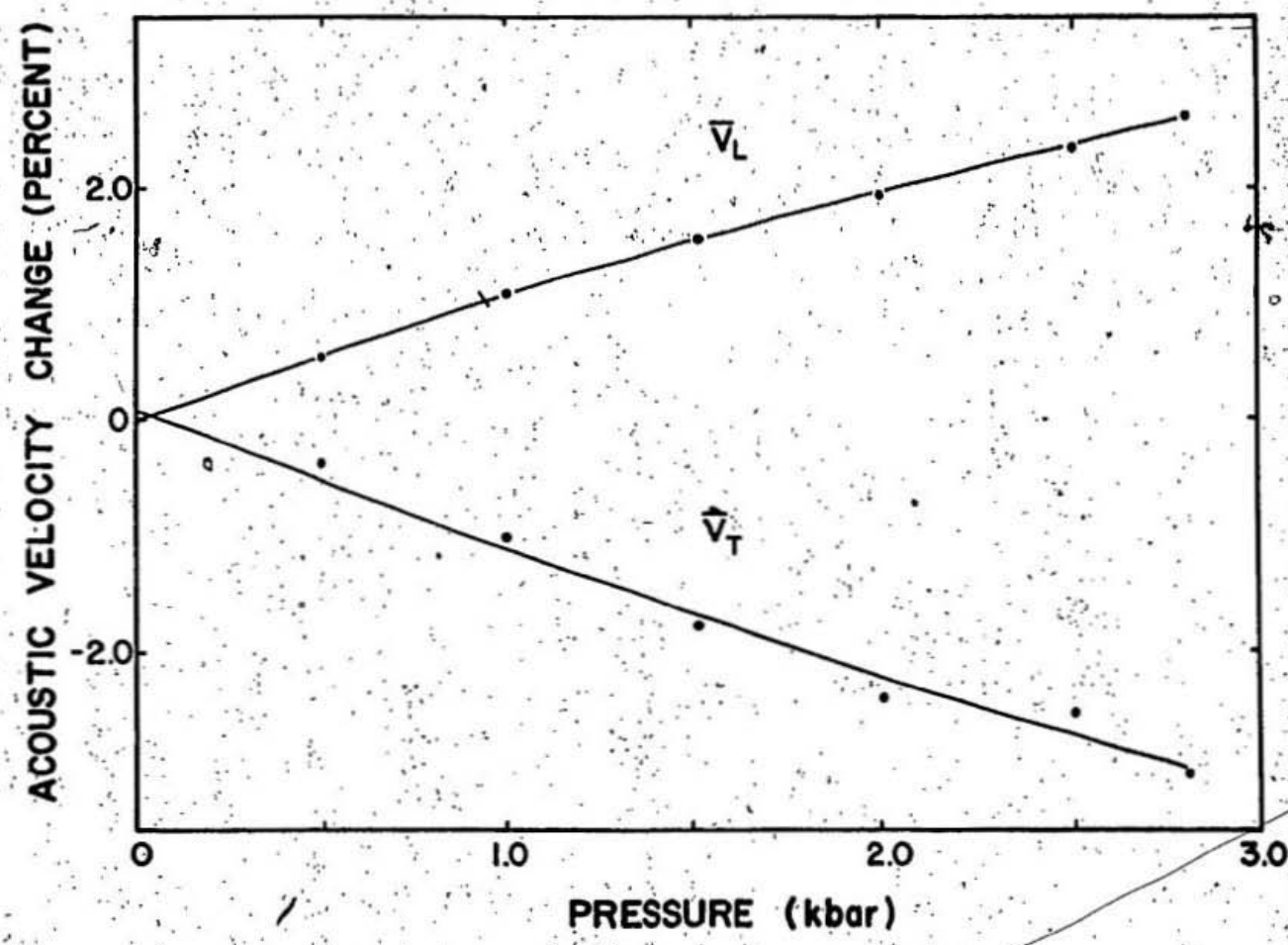
ACOUSTIC VELOCITY CHANGE (PERCENT)
2.0
0
-2.0
$\bar{V}_L$
$\bar{V}_T$
0
1.0
2.0
3.0
PRESSURE (kbar)

Figure 3.23

CHAPTER 4

THE ELASTIC PROPERTIES OF HIGH PRESSURE ICE POLYMORPHS

4.1 Determination of Densities for the Ice Polymorphs

Density is a critical parameter which appears in the expressions relating the elastic constants to acoustic velocities in ice Ih. It is also required to determine the refractive indices (via the relationship between Eulerian strain and refractive index[116]) of the different ice phases, at the various pressures, for use in the Brillouin equation which translates frequency shifts into acoustic velocities. Little data exists in the literature on the densities of the ice phases at the temperature and range of pressures used in these experiments. Bridgman[79,140] had determined densities for various ice polymorphs, however, his compressibilities for ice Ih were known to be incorrect, which made the results for the other phases suspect. It was therefore necessary to conduct an independent set of experiments to determine the density of ice for the whole pressure range investigated in the present light scattering work.

A thick-walled tube (29.5 mm length and 6.3 mm O.D.) was machined from a solid piece of 304 stainless steel stock (C) of Figure 4.1). A solid right cylindrical stainless steel plug (E), 3.4 mm diameter, was then snugly inserted into one open end to a depth of 13.4 mm and silver soldered into place. The other end was machined to fit onto the rotation stem inside the high pressure cell.

Initially a chamber similar to that just described had been

Figure 4.1. Density determination apparatus: A, right cylindrical glass plug; B, scale with .1 mm markings; C, thick-walled stainless steel tube; D, ice sample; E, hard soldered stainless steel plug; F, coupling space for mounting onto stem inside the high pressure cell.

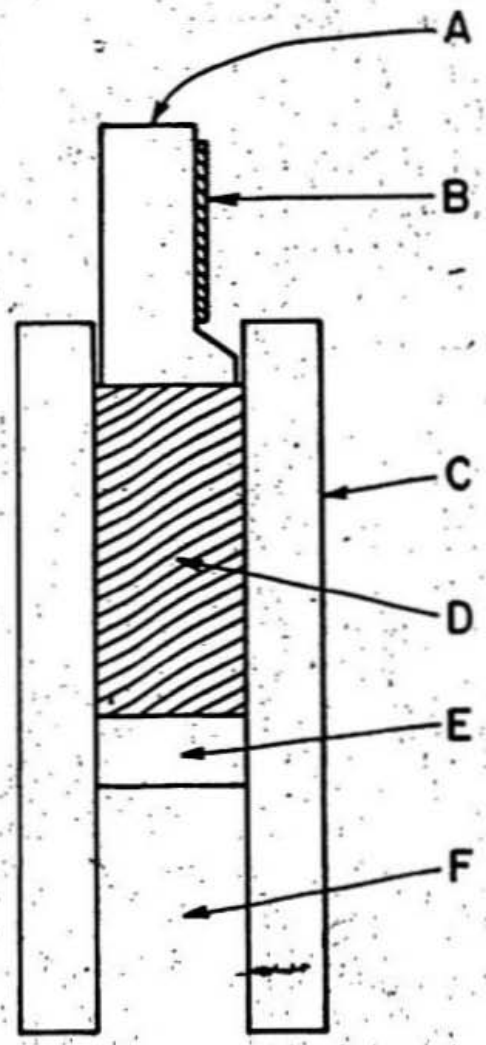

Figure 4.1

made of brass tube with a thinner wall. Its strength was insufficient, however, as it tended to deform when it was filled with ice and pressurized inside the high pressure cell.

To prepare a sample the stainless steel chamber was carefully filled with deionized water using a very small plastic tube to ensure that no bubbles were inadvertantly placed inside. The chamber was then immersed in water at a temperature of approximately 2°C and a close fitting right cylinder of single crystal Mendenhall glacial ice (D), previously cut from a larger crystal by use of the melt extrusion technique (Section 3.1), was quickly plunged into the water and gently pushed all the way into the chamber. This forced most of the water out. The chamber was then removed from the water bath and exposed to the cold atmosphere of the freezer which caused the small amount of deionized water, left inside the chamber [redacted] the ice, to rapidly freeze. The result was a chamber filled with pure ice which was absolutely free of bubbles.

Approximately 2 mm of ice was then removed from the open end of the stainless steel tube by use of a rotating scraper. It was then allowed to warm to 0°C and placed back into the cold bath. The space in the end of the chamber filled with water and a small glass plug (A), 7.5 mm in length, with a diameter close to that of the inside of the tube, was pushed into the opening until it rested against the ice. The stainless steel chamber, with ice inside and the glass plug protruding from one end, was then taken out of the water and left in the freezer.

Prior to its insertion, a section of the glass plug's curved wall had been ground flat and a small scale (B), with 1mm markings, had been epoxied onto it. This had been covered by a thin (~.2 mm)

protective piece of glass slide which had also been epoxied into place. When the ice-filled stainless steel chamber was placed inside the high pressure cell and pressure was applied, the ice would contract and the glass plug would move slightly into the chamber. Since the dimensions of the chamber did not change appreciably in the pressure regime of these experiments, the ice was forced to translate any change of its volume, by plastic extrusion, into a change in length because its diameter was always fixed, ie. $\Delta V/V = \Delta L/L$, where V is volume and L is length. Movement of the plug was monitored through the window of the pressure cell by means of a travelling microscope (.002 mm accuracy). The measurements were taken relative to the edge of the stainless steel cylinder, which was also visible in the central region of the observation window, in order to eliminate errors which might have arisen from recession of the rotation stem as pressure was increased. The cell windows were observed to bow outwards as the internal pressure increased and refraction effects could possibly have introduced small errors in the strain measurements if readings were taken around the window periphery. As precautions, the smallness of the markings on the scale, combined with the fact that the edge of the chamber appeared in the central region of the window at all except the highest pressures, made it possible to take most readings when the microscope was reasonably centered with respect to the window, thus avoiding possible error due to refraction. By measuring the spacing of the markings on the scale at high pressure it was later determined that the error arising from refractive effects was very small, if not negligible. The estimated accuracy of the data obtained using this density measurement technique was .1%.

The movable plug had been made of glass for two reasons. Its transparency permitted inspection of the ice specimens inside the stainless steel chamber to ensure there were no bubbles present. Also, due to the plug's transparency, the small scale on the plug could easily be illuminated through the view port opposite the one used by the travelling microscope.

The following expression was derived from the geometry of the apparatus to determine the density of ice based on the observed movements of the glass plug relative to the edge of the stainless steel chamber. The slight pressure induced changes in the dimensions of the chamber and the glass plug were also taken into account.

$$\rho(P)=\rho_0 L' \left(e^{-\frac{2}{3}k_s P}\left(Ce^{-\frac{1}{3}k_s P} - \left(Ee^{-\frac{1}{3}k_g P} - A\right)\right)\right)^{-1} \qquad (4\text{-}1)$$

Here $\rho(P)$ denotes the density at pressure P, ρ_0 denotes the zero pressure density of ice Ih, L denotes the zero pressure length of the ice sample, C denotes the zero pressure depth of the stainless steel chamber, E is the zero pressure distance from the observed mark on the measurement scale to the end of the glass plug in contact with the ice, A is the measured distance between the mark on the scale and the edge of the stainless steel chamber, and K_s and K_g are the compressibilities of 304 stainless steel[141] and pyrex glass[142] respectively.

The data presented in Table 4.1 and Table 4.2 were obtained from 4 pressure runs, 2 on each of 2 separate Mendenhall ice samples. A set of data was obtained by first elevating the cell pressure to approximately 10 kbar, which took the ice sample through three phase changes, and leaving it at that pressure for at least 2.5 hours. This gave the ice ample time to flow plastically and relieve any nonhydrostatic stresses

TABLE 4.1

DENSITY VERSUS PRESSURE DATA FOR ICE Ih, ICE II AND ICE III

Temperature: -35.5°C

Ice Ih		Ice II		Ice III	
Pressure (kbar)	Density (g/cm³)	Pressure (kbar)	Density (g/cm³)	Pressure (kbar)	Density (g/cm³)
1.77	.9383	3.27	1.1975	3.25	1.1715
1.76	.9371	3.21	1.1956	3.22	1.1709
1.68	.9379	2.81	1.1904	3.06	1.1700
1.63	.9364	2.54	1.1932	2.79	1.1641
.99	.9302	2.31	1.1878	2.78	1.1655
.99	.9304			2.34	1.1615
.98	.9312			2.31	1.1614
.97	.9309			2.29	1.1580
.38	.9252				
.33	.9255				
.00	.9228				
.00	.9228				
.00	.9228				
.00	.9228				

TABLE 4.2

DENSITY VERSUS PRESSURE DATA FOR ICE V AND ICE VI

Temperature: -35.5°C

Ice V		Ice VI	
Pressure (kbar)	Density (g/cm³)	Pressure (kbar)	Density (g/cm³)
5.84	1.2727	9.48	1.3623
5.82	1.2756	9.44	1.3635
5.81	1.2744	9.23	1.3690
5.80	1.2752	9.18	1.3694
5.00	1.2683	8.28	1.3625
4.98	1.2691	8.23	1.3616
4.97	1.2667	8.17	1.3668
4.91	1.2667	7.27	1.3556
4.03	1.2619	7.27	1.3533
4.00	1.2555	7.23	1.3558
4.00	1.2587	7.19	1.3532
3.99	1.2578	6.45	1.3476
3.30	1.2502	6.43	1.3466
		6.38	1.3443
		6.36	1.3462

caused by friction with the chamber wall. Strain measurements were then recorded as the pressure was incrementally decreased. The fact that one of the measurements on ice II was taken on the increasing side of a pressure run and yielded essentially the same result as the data for decreasing pressure implied that no nonhydrostatic stresses existed after suitable relaxation time was allowed.

The density data for the various ice phases have been fitted with linear or quadratic expressions depending on whether curvature was obvious in the data plots. These expressions are given below.

$$\rho_{iceIh}(P) = .9228 + 7.2785 \times 10^{-3}P + 7.5023 \times 10^{-4}P^2 \qquad (4\text{-}2)$$

$$\rho_{iceII}(P) = 1.1698 + 8.1760 \times 10^{-3}P \qquad (4\text{-}3)$$

$$\rho_{iceIII}(P) = 1.1321 + 1.2057 \times 10^{-2}P \qquad (4\text{-}4)$$

$$\rho_{iceV}(P) = 1.1974 + 1.9632 \times 10^{-2}P - 1.0982 \times 10^{-3}P^2 \qquad (4\text{-}5)$$

$$\rho_{iceVI}(P) = 1.1559 + 4.5212 \times 10^{-2}P - 2.4345 \times 10^{-3}P^2 \qquad (4\text{-}6)$$

Here ρ denotes density in g/cm^3 and P denotes pressure in kbar.

Figure 4.2 shows the data from Tables 4.1 and 4.2. The solid lines are the least square fits given by equations (4-2) to (4-6).

All measurements were taken at -35.5°C. When a sample had been placed in the cell and the pressure was initially applied it was found that ice Ih invariably transformed to ice III, though the pressure and temperature were in the phase stability region of ice II. As the pressure was reduced from its maximum value ice V also transformed into ice III. In order to produce ice II it was necessary to lower the temperature of the cell to approximately -40°C before a sample was

Figure 4.2. Density versus pressure for the various ice phases. The solid lines represent least squares fits to the data points shown as x's. The boxed points for ice Ih are densities determined from the bulk moduli of Mendenhall ice in Section 3.4. All of the density data were obtained at -35.5°C.

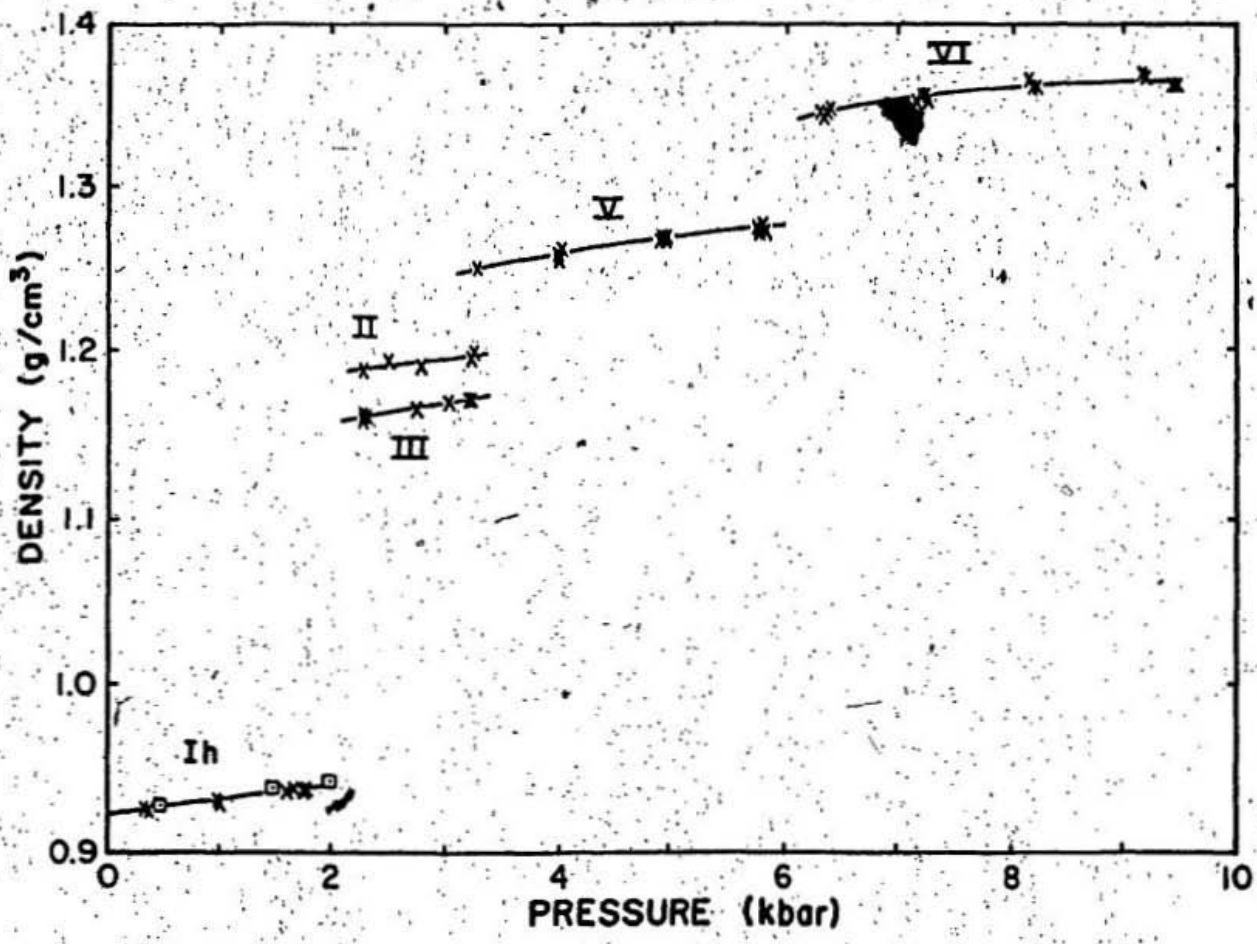
1.4
1.3
1.2
1.1
1.0
0.9
DENSITY (g/cm³)
0
2
4
6
8
10
PRESSURE (kbar)
VI
V
II
III
Ih

Figure 4.2

initially compressed. This temperature was low enough to overcome the tendency of ice III to supercool with respect to ice II. When pressure was applied ice Ih then transformed to ice II, though not immediately. It first transformed to ice III and then within 4 hours another complete phase change to ice II would occur. Maximum pressure was then applied and the temperature was adjusted back to -35.5°C. When the pressure was later reduced, ice V was found to transform to ice II. Whether or not ice V or ice Ih became ice II at the appropriate phase transitions at -35.5°C depended on whether that particular ice sample had already been transformed into ice II earlier in the experiments.

The experiments on the two Mendenhall ice samples were conducted as follows. For run #1 of sample #1 the temperature was set at -35.5°C and the pressure was elevated to its maximum value of 9.23 kbar and left for 8 hours. Pressure was then incrementally reduced and strain measurements recorded at each step. The measurements at the higher pressures were made at minimum 1.5 hour intervals to ensure that the ice sample was given ample time to adjust its volume to suit the reduced pressure and to overcome any friction with the wall of the chamber. Thirteen strain measurements were recorded as the pressure was brought to zero. Phase transitions occurred distinctly and abruptly (see Figure 4.2). The exact procedure was then repeated for run #2 except that when the set of 13 strain measurements had been obtained the cell temperature was adjusted to ~-40°C and the pressure was increased again to the point where ice Ih transformed to ice III. The pressure was held constant until the ice further transformed to ice II. Then the temperature was readjusted back to -35.5°C and measurements of strain in ice II were made at two pressures. Run #1 of sample #2 was

conducted in the same manner as run #1 of sample #1 except that 14 measurements were made instead of 13. The temperature was then reduced to --40°C and the pressure applied until the first phase transition to ice III occurred. Constant pressure was maintained until the transition to ice II was completed and then the pressure was increased to its maximum value and the temperature reset to -35.5°C. Approximately 3 hours later run #2 was conducted in the same manner as the other runs. This time ice V transformed to ice II as the pressure was reduced whereas in run #1 it had transformed to ice III.

To justify this technique for determining ice densities it was necessary to rule out what might sensibly be considered the greatest possible source of error, namely the possible inclusion of oil between crystallites of a sample during phase transitions. Several observations confirmed that oil inclusion did not occur during these experiments on ice density. Firstly it was noted in all cases that after a pressure run the glass plug had returned to the same position in the chamber as it had been prior to the run, which implied that oil was not present in the sample after a run. It could be argued that oil had entered the sample during the pressure run and then escaped in the same manner, however, it was clear from the laser scattering experiments (Section 4.3) that if oil entered a sample it did so only after many phase changes and it remained in the sample even after the pressure was reduced to zero. Samples which contained no oil after a set of high pressure Brillouin experiments had shown no evidence of high background scatter due to oil inclusion during the experiments. Hence, the specimens used in the density experiments which were free of oil inclusions at the end of the pressurizations were also free of oil

during the density measurements. Also the results for ice Ih, from the density experiments, were in close agreement with the densities obtained using the bulk moduli from the light scattering experiments on single crystals of ice Ih. This would not be expected if oil inclusions were present during the density determinations. Finally the consistency of the four independent sets of data, evident in Figure 4.2, excludes the possibility of sporadic inclusions of oil.

4.2 Sample Preparation for the High Pressure Phases

During the course of the experimentation on single crystals of ice Ih it was discovered that when the pressure was elevated to initiate the first phase transition to ice III the sample did not retain its original shape after the phase change. The end of the specimen became very rough and it deviated severely from its original orientation. Also the specimen became barrel shaped in the middle. Furthermore it was no longer moncrystalline, but was instead composed of many crystallites, some of which were large (~1 mm^3) and others were much smaller. The amount of sample distortion was not surprising given that the phase transition entailed a ~20% change in the sample's volume and was observed, when the specimen was transformed back to ice Ih at least, to take place nonuniformly by starting at one end of the specimen and propagating to the other.

Because moncrystalline specimens would shatter during phase transitions it was clearly not possible to conduct experiments on single crystals of any of the high pressure phases of ice using the apparatus as it existed. Single crystals of different polymorphs could conceivably be grown from moncrystalline seeds in an apparatus where

fine adjustments of temperature and pressure could be made while viewing whole specimens, such as in a diamond-anvil cell.[116,143-145] Experiments on polycrystalline aggregates were possible, however, with the high pressure cell as it was, though the problems of sample deformation and nonuniformity of crystallite size had to be overcome. The former would introduce error in the scattering angle and the later would introduce statistical bias in any attempts to obtain averaged data. The samples would also have to be completely free from bubbles. In preliminary experiments it had been noted that the presence of even the tiniest bubbles made samples unsuitable for the Brillouin studies because of laser light reflected from the bubbles which overwhelmed the frequency shifted signals which were of interest. The information obtained from experiments on bubble free, uniformly polycrystalline ice samples could be used to determine averaged elastic properties for the various ice phases accessible with the present apparatus.

The following procedure was used to obtain bubble free, polycrystalline aggregates of very small and uniform crystallites. Deionized water was vigorously boiled in a glass beaker over a Bunsen burner for at least 10 minutes to remove dissolved air. As the water boiled, a glass tube (approximately 4 mm in diameter and 1.5 cm in length), sealed at one end with a flexible plastic plug, was also put into the beaker where it filled with water which continued to boil. After a minute or so the Bunsen burner was removed and the water stopped boiling. Within a few seconds the water vapor bubbles inside the glass tube disappeared and it was then quickly removed from the beaker, oriented vertically with the sealed end pointing upwards. The tube was slightly more than filled so that the open bottom end assumed

a convex shape due to the excess water. The tube was immediately placed, open end downwards, onto a cold copper block (~-20°C). Rapid freezing ensued and within ~5 minutes the water was completely frozen. The flexible plastic plug at the top of the tube permitted expansion as the water solidified and thereby prevented the tube from breaking. Because the freezing was so quick at the instant the water made contact with the plate, very tiny crystallites formed (~.1 mm diameter) and continued to grow along the length of the tube. The final result was a polycrystalline cylinder of ice, completely free of bubbles, which consisted of very fine elongated crystallites. When such a sample of ice was later taken through a phase transition in the high pressure cell the crystallites became rounded and remained very tiny.

To prevent an ice sample from grossly deforming during phase transformations it was necessary to partially confine it in a glass cell (Figure 4.3) which would allow the specimen (H) to expand and contract lengthwise and yet preserve its cylindrical shape. The cell was basically a thick walled pyrex tube (G) plugged at one end with a solid right cylinder of pyrex (I). The ends of the plug had been flattened normal to its length and polished prior to attaching it to the pyrex tube. The plug had been attached by snugly inserting it part way into the cylinder and then carefully applying a flame from a propane torch to the section of cylinder where both pieces of pyrex were in contact. The glass partially melted and fused the two pieces together.

Just inside the open end of the pyrex cell an indentation (N) was ground into the glass around its circumference. This groove provided a

Figure 4.3. Glass cell and brass sample holder for Brillouin scattering experiments: A, securing pin; B, rotation stem head ; C , darkened hole to minimize laser backscatter ; D, retaining clip ; E , anti-rotation fingers; F, glass disc to minimize oil inclusion during phase transitions; G, thick pyrex tube; H, polycrystalline ice sample; I, right cylindrical pyrex plug with polished flattened ends, fused to glass tube; J, copper ring for gripping the glass cell; K, retaining clip; L, brass sample holder; M, tubular brass coupler; N, niche to secure the brass coupler to the glass cell.

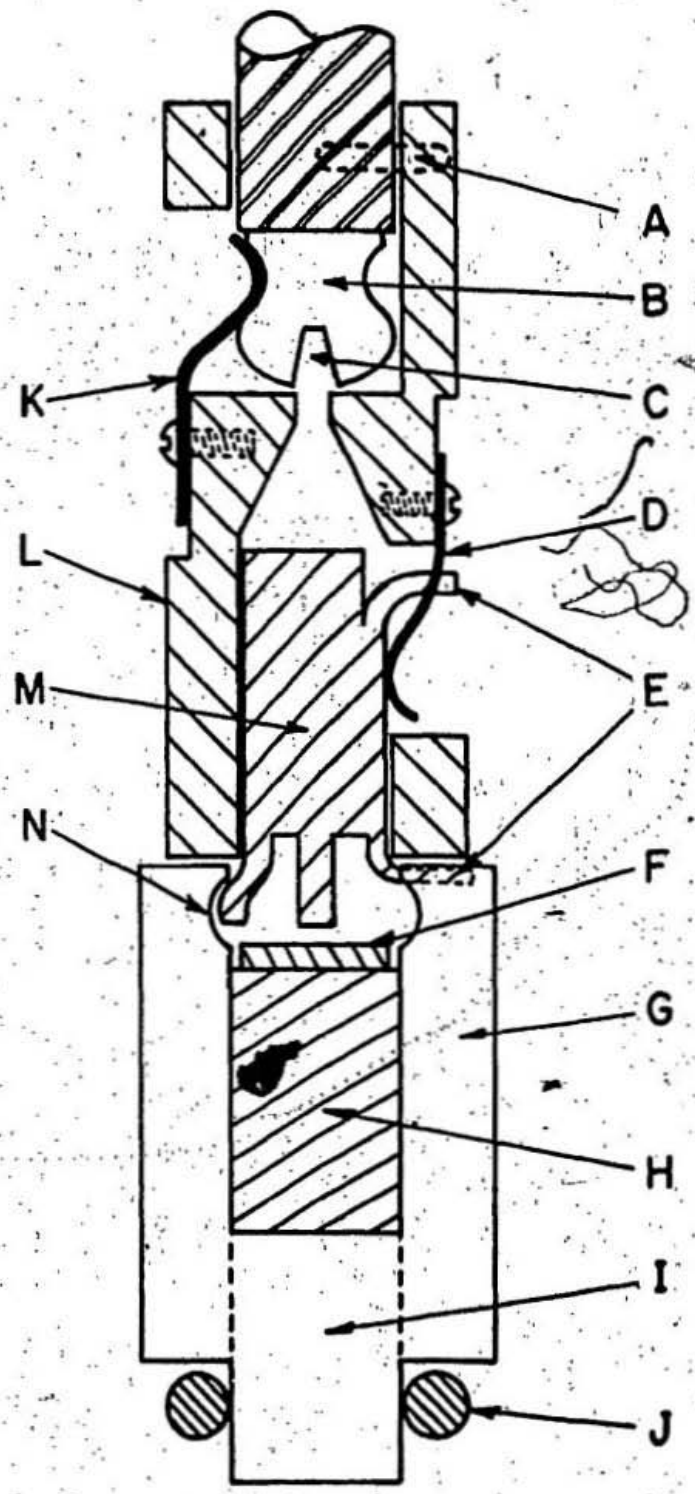

Figure 4.3

niche for the flared sections on the end of a brass tube (M) to grip the cell. This brass tube fitted into the same sample holder (L) used for single crystals of ice Ih. It provided the means whereby the pyrex cell was attached to the brass holder during the experiments. On the end of the brass tube inside the holder there was a flared section (E) which protruded through the opening in the side of the holder and prevented any relative rotation. On the flat circular ring of glass at the open end of the pyrex cell deep slots had been ground into the glass across the diameter of the opening. Another flared section (E) of brass tube fitted into one of the slots and prevented the cell from rotating relative to the holder. These features were necessary because the viscosity of the pressure medium increased whenever the pressure was elevated inside the high pressure cell and this produced torque which opposed the rotation of the sample cell as the stem and holder were rotated. The brass tube provided the strong mechanical coupling required between the cell and the holder.

After a suitable polycrystalline sample had been grown using the technique described above, it had to be transferred to the pyrex cell. This was done by first removing the sample from the glass tube in which it had been grown by letting it warm, until it detached from the wall, and then pushing it out. The sample cell was carefully filled with deionized water so that no bubbles were present and placed in a water bath maintained at ~2°C. The sample, held at one end with wire tweezers, was then plunged into the bath and gently pushed into the open end of the cell until it contacted the bottom. The cell and ice were removed from the bath and the small quantity of water inside with the sample quickly froze in the cool atmosphere of the freezer. The

open end was then cleared of ice, with a rotatable scraper, to a depth which allowed the insertion of a warm thin glass disc (F). This produced a small amount of melt water which refroze and bonded the disc to the ice. Any excessive ice was removed again so that the groove in the inside wall of the cell was accessible to the flared end of the brass tube which connected the cell to the holder. The glass disc served to increase the number of phase changes that a sample could tolerate before oil inclusions severely diminished the quality of the optical spectra during the Brillouin scattering experiments.

A minor feature of the pyrex cell was a ring of thick copper wire (J) which fitted round the glass plug protruding from the closed end. It simply increased the diameter of the cell so that the tool used for placing samples in the high pressure apparatus could grip it.

4.3 Brillouin Scattering Experiments on High Pressure Ice Phases

Once a polycystalline ice sample had been prepared, it was immediately transferred to the high pressure cell, using the same procedure that was employed to place the monocrystalline samples of ice Ih into the apparatus. The application of hydrostatic pressure took place as soon as the cell's temperature had stabilized. Each sample was taken through at least one (usually more than one) phase transition before any light scattering experiments were conducted. The first transformation to ice III, when the temperature had been set at -35.5°C and the pressure reached ~3 kbar, involved a ~20% change in the sample's volume. This ensured that the sample, which was initially composed of tiny elongated grains, had smashed into very tiny rounded crystallites, and was therefore suitably isotropic to yield unbiased

averaged acoustic velocities.

The data presented in Tables 4.3 to 4.6 come from experiments on 5 different ice specimens. Frequency shifts for each of 3 high pressure phases were collected from 3 of the 5 samples. Ice II data had been collected from 4 samples. The frequency shifts were translated into acoustic velocities through use of the Brillouin equation (1-9), where the refractive indices were supplied by the relationship between Eulerian strain and the refractive index[116] using the present density data. This expression is given by,

$$n(\rho_o) - n(\rho) = A\epsilon \qquad (4\text{-}7)$$

where n is the refractive index, ρ denotes density, A is a constant and ϵ is the Eulerian strain as given below.

$$\epsilon = 1/2 \left[1 - \left(\rho/\rho_o \right)^{2/3} \right] \qquad (4\text{-}8)$$

The authors[116] fitted (4-7) in the liquid region, using data for the density and refractive index of water at various pressures, to obtain A and then extrapolated to the solid phases using the same value. The measured and extrapolated refractive index for ice VI[116] were in agreement to within 1%. This method was therefore assumed to be reliable and the same expression (given below), derived from the fitting procedure by Polian and Grimsditch,[116] was subsequently adopted for the present analysis.

$$n = 1.334 + 0.51(\rho^{2/3} - 1) \qquad (4\text{-}9)$$

TABLE 4.3

FREQUENCY SHIFTS AND ACOUSTIC VELOCITIES FOR ICE II

Temperature: -35.5°C

Pressure (kbar)	Averaged Longitudinal Frequency Shift And Acoustic Velocity $\bar{\Omega}_L$ (GHz)		$\bar{V}_L$ (km/s) ±1.5%	Transverse Frequency Shift And Acoustic Velocity Ω_T (GHz)	V_T (km/s) ±3.5%
1.90	16.40	← ±2.7% →	4.276	8.25	2.151
2.43	16.05	← ±1.4% →	4.181	8.95	2.331
2.50	16.61	← ±3.0% →	4.326	8.50	2.214
2.58	16.75	← ±3.2% →	4.362	--	--
2.60	16.78	← ±2.6% →	4.370	8.49	2.211
2.64	16.66	← ±3.0% →	4.338	8.53	2.221
"	"		"	9.22	2.401
2.66	16.61	← ±2.5% →	4.325	8.62	2.244
2.82	16.67	← ±2.5% →	4.339	9.05	2.356
3.16	16.28	← ±1.8% →	4.235	9.08	2.362
3.22	16.79	← ±2.4% →	4.367	8.77	2.281
3.25	16.61	← ±2.3% →	4.320	9.31	2.421
"	"		"	8.39	2.182
3.29	16.50	← ±2.2% →	4.291	8.41	2.187
"	"		"	8.56	2.226
3.72	16.36	← ±1.4% →	4.251	9.18	2.386

Note: In this table and the three that follow, each uncertainty which appears in the columns is the standard deviation for the eight measurements which were averaged to obtain that particular mean frequency shift and mean velocity. The uncertainty quoted at the top of the table, for the mean longitudinal and transverse velocities, corresponds to the estimate for the absolute error of any individual measurement. If no uncertainty is quoted in the column for a longitudinal shift/velocity it indicates that the measurement was a single-point value obtained using the techniques discussed in Section 4.3.

TABLE 4.4

FREQUENCY SHIFTS AND ACOUSTIC VELOCITIES FOR ICE III

Temperature: -27.2°C

Pressure (kbar)	Averaged Longitudinal Frequency Shift And Acoustic Velocity $\bar{\Omega}_L$ (GHz)		$\bar{V}_L$ (km/s) ±1.5%	Transverse Frequency Shift And Acoustic Velocity Ω_T (GHz)	V_T (km/s) ±3.5%
2.17	13.94	← ±3.1% →	3.658	7.35	1.929
"	"		"	6.98	1.831
"	"		"	7.17	1.881
2.18	13.88	← ±3.3% →	3.642	6.70	1.758
2.21	13.81	← ±5.7% →	3.623	--	--
2.29	--		--	6.98	1.831
2.37	--		--	6.96	1.825
2.40	13.95	← ±2.5% →	3.658	7.24	1.898
"	"		"	7.24	1.898
"	"		"	6.82	1.788
"	"		"	7.21	1.891
"	"		"	7.97	2.090
"	"		"	6.96	1.825
"	"		"	7.05	1.849
2.52	14.20	← ±2.8% →	3.722	--	--
2.67	--		--	7.06	1.850
2.68	14.23	← ±2.8% →	3.728	8.01	2.099
2.82	--		--	8.26	2.163
"	--		--	8.60	2.252
"	--		--	8.67	2.271
"	--		--	8.57	2.245
"	--		--	8.12	2.127
"	--		--	7.81	2.046
"	--		--	7.88	2.064
2.85	14.20	← ±1.5% →	3.719	7.21	1.888
2.87	13.82	← ±3.2% →	3.619	6.77	1.773
"	"		"	7.95	2.082
"	"		"	7.19	1.883
"	"		"	8.07	2.113
3.11	14.11	← ±1.8% →	3.693	7.11	1.861
3.16	--		--	7.40	1.936
"	--		--	7.49	1.960
"	--		--	7.26	1.900
3.18	14.33	← ±2.6% →	3.749	7.54	1.973
3.19	14.39	← ±1.8% →	3.765	7.22	1.889
"	"		"	7.49	1.960
"	"		"	6.76	1.769
3.19	--		--	8.60	2.250
"	--		--	9.02	2.360

TABLE 4.5

FREQUENCY SHIFTS AND ACOUSTIC VELOCITIES FOR ICE V

Temperature: -35.5°C

Pressure (kbar)	Averaged Longitudinal Frequency Shift And Acoustic Velocity $\bar{\Omega}_L$ (GHz)	$\bar{V}_L$ (km/s) ±1.5%	Transverse Frequency Shift And Acoustic Velocity Ω_T (GHz)	V_T (km/s) ±3.5%
3.55	16.21 ← ±1.2% →	4.162	--	--
3.87	16.40 ← ±2.1% →	4.208	--	--
3.89	--	--	9.92	2.545
3.91	--	--	8.13	2.086
"	--	--	8.04	2.063
3.97	--	--	8.32	2.134
4.37	--	--	8.99	2.304
4.48	16.29 ← ±2.1% →	4.174	8.66	2.219
4.81	16.57 ← ±1.4% →	4.242	--	--
4.85	16.37 ← ±2.1% →	4.191	8.88	2.273
"	"	"	8.61	2.204
5.55	--	--	7.97	2.038
5.57	16.57 ← ±1.9% →	4.236	7.19	1.838
6.03	16.49	4.213	--	--
6.40	--	--	9.70	2.477
6.59	--	--	8.72	2.226

TABLE 4.6

FREQUENCY SHIFTS AND ACOUSTIC VELOCITIES FOR ICE VI

Temperature: -35.5°C

Pressure (kbar)	Averaged Longitudinal Frequency Shift And Acoustic Velocity $\bar{\Omega}_L$ (GHz)	$\bar{V}_L$ (km/s) ±1.5%	Transverse Frequency Shift And Acoustic Velocity Ω_T (GHz)	V_T (km/s) ±3.5%
6.13	--	--	8.64	2.176
6.31	17.90 ← ±2.5% →	4.506	9.23	2.323
6.75	--	--	9.38	2.358
7.07	17.66	4.437	--	--
7.13	--	--	9.40	2.361
7.27	18.08	4.540	--	--
7.51	--	--	9.27	2.327
7.74	18.19 ← ±0.9% →	4.564	9.28	2.328
8.20	18.28	4.583	--	--
8.41	18.35	4.600	--	--
8.48	--	--	9.40	2.356
9.24	--	--	9.31	2.333
9.32	18.43 ← ±1.4% →	4.618	9.48	2.376
"	"	"	9.33	2.338
9.33	18.35 ← ±0.9% →	4.598	10.48	2.626

The sequence of pressures and temperatures for the light scattering experiments did not necessarily follow a pattern of systematic incremental increase or decrease of pressure or temperature, but depended rather on a number of factors. 1. The FSR of the Fabry-Perot interferometer at any one time would be more suited to measurements of some phases, and not so suitable to others because of the large difference in typical frequency shifts between some phases (eg. ice III and ice VI). 2. The number of phase transformations that a sample had been through was a factor because if the quality of the signal had diminished significantly, due to oil inclusions, it was preferable to continue experiments on that particular phase rather than cause another transformation which would produce more oil inclusions. 3. Sparcity of data in some pressure regions, at times, required experiments to be conducted at points scattered throughout the whole pressure range in order to fill in the gaps. 4. Difficulties encountered with rotating samples, in general, reduced the amount of data collected at high pressure, and necessitated special measures to be taken in order to obtain averaged longitudinal frequency shifts (discussed below).

Since it was not possible to produce monocrystalline samples, as in the case of the experiments on single crystals of ice Ih (Chapter 3), the emphasis of these experiments was shifted towards obtaining average values for longitudinal and transverse acoustic wave velocities for the high pressure ice polymorphs. The strategy for acquiring a typical averaged data point was to set the pressure at a desired value within the stability region of a given phase, and then run a set of 8 different Brillouin scattering experiments at evenly spaced sample rotation settings, fully spanning 360°. These were then averaged and

assumed to be reasonable estimates for the acoustic velocity in homogeneous polycrytstalline ice of that particular phase. Unfortunately the transverse frequency shift components, which were characteristically much weaker than the longitudinal components, were often lost in the background noise so that averaged transverse shifts were not obtained at each pressure setting. The frequency shifts and velocities associated with transverse acoustic waves are therefore presented as single data point values in the tables and on the charts, rather than averaged values.

For each Brillouin experiment, frequency shifts were obtained from the DAS display in essentially the same manner described in the study of single crystals of ice Ih (Section 3.3). A magnification window, corresponding to a factor of 70, was also placed over the spectral region of interest to reduce accumulation times. The estimated uncertainties associated with the velocities determined from the measured frequency shifts of longitudinal and transverse components, for any particular Brillouin scattering experiment, were typically ±1.5% and ±3.5% respectively. This was due mostly to the uncertainty involved in identifying the centers of the broad peaks of each spectral component on the DAS display. The rest of the error was related to the uncertainty in the refractive index, determined using the method of Polian and Grimsditch,[116] which is incorporated in the Brillouin equation. The standard deviations in the longitudinal measurements, associated with each averaged value, for ice II, III, V and VI were typically ±2.4%, ±2.8%, ±1.8% and ±1.4% respectively. Hence, ice VI appeared to be the most isotropic of the ices.

The time required to complete a set of 8 experiments at one

pressure setting varied considerably depending on the quality of the transverse components, if they were visible at all. Usually only 1 or 2 settings out of the 8 would yield transverse components and these would require considerable amounts of time, often overnight, whereas the longitudinal components were usually resolved within one hour. The complete data set presented in the tables and charts was collected from experiments which spanned a two month period. During that time, because of the differences in frequency shift between the different ice phases, the FSR of the Fabry-Perot interferometer was changed twice so that three different settings, 21.51 GHz, 30.13 GHz, and 40.28 GHz were used. These chosen settings optimized the three considerations outlined in the experiments on ice Ih, namely; that the resolution be maximized, that there be no overlap of components, and that any ambiguity as to which transverse peaks were associated with which longitudinal peaks would be minimal.

The quality of a Brillouin spectrum was largely a factor of the number of phase changes that a sample had been cycled through. Ultimately oil inclusions, which sometimes appeared during phase changes, would accumulate to the point where experiments would have to be terminated because the light which scattered from the inclusions was so intense. When this happened the background noise threatened to wash out even the longitudinal signal, which was normally quite discernable. Figures 4.4 to 4.7 are representative spectra for ice II, III, V and VI.

The widths of the central, longitudinal and transverse spectral peaks varied considerably, depending on the degree of oil inclusion, and also on the number and relative c-axis orientations of the grains

Figure 4.4. Representative Brillouin spectrum for a polycrystalline sample of ice II at -35.5°C. One complete order is shown with two unshifted components U. The free spectral range of the Fabry-Perot is 21.51 GHz. L designates the longitudinal Brillouin component and T the transverse component as shifted from U. The region of the spectrum showing L and T has been amplified 70x in terms of data acquisition.

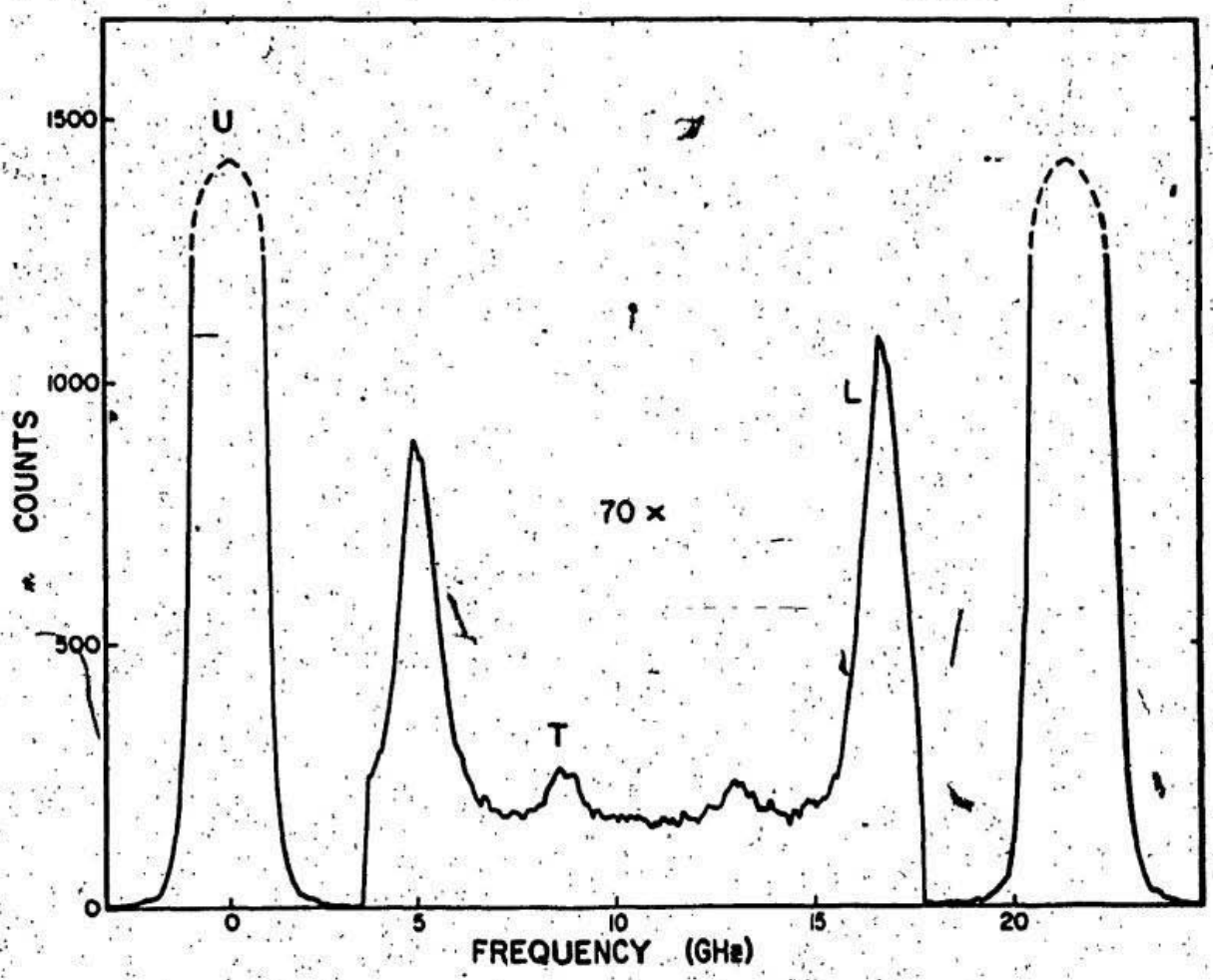

Figure 4.4

Figure 4.5. Representative Brillouin spectrum for a polycrystalline sample of ice III at -27.2°C. One complete order is shown with two unshifted components U. The free spectral range of the Fabry-Perot is 40.28 GHz. L designates the longitudinal Brillouin component and T the transverse component as shifted from U. The region of the spectrum showing L and T has been amplified 70x in terms of data acquisition.

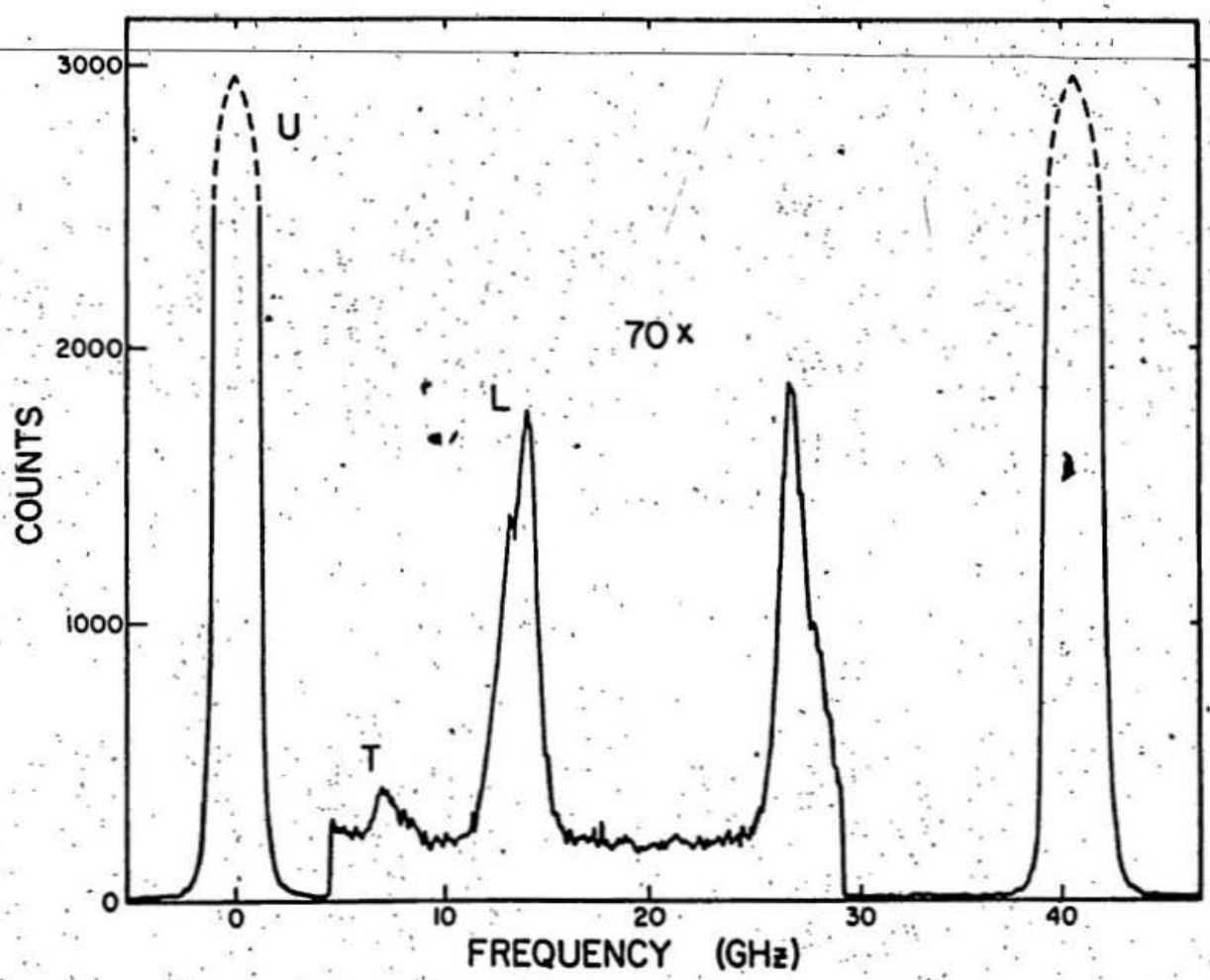

Figure 4.5

Figure 4.6. Representative Brillouin spectrum for a polycrystalline sample of ice V at ~-35.5°C. One complete order is shown with two unshifted components U. The free spectral range of the Fabry-Perot is 21.51 GHz. L designates the longitudinal Brillouin component and T the transverse component as shifted from U. The region of the spectrum showing L and T has been amplified 70x in terms of data acquisition.

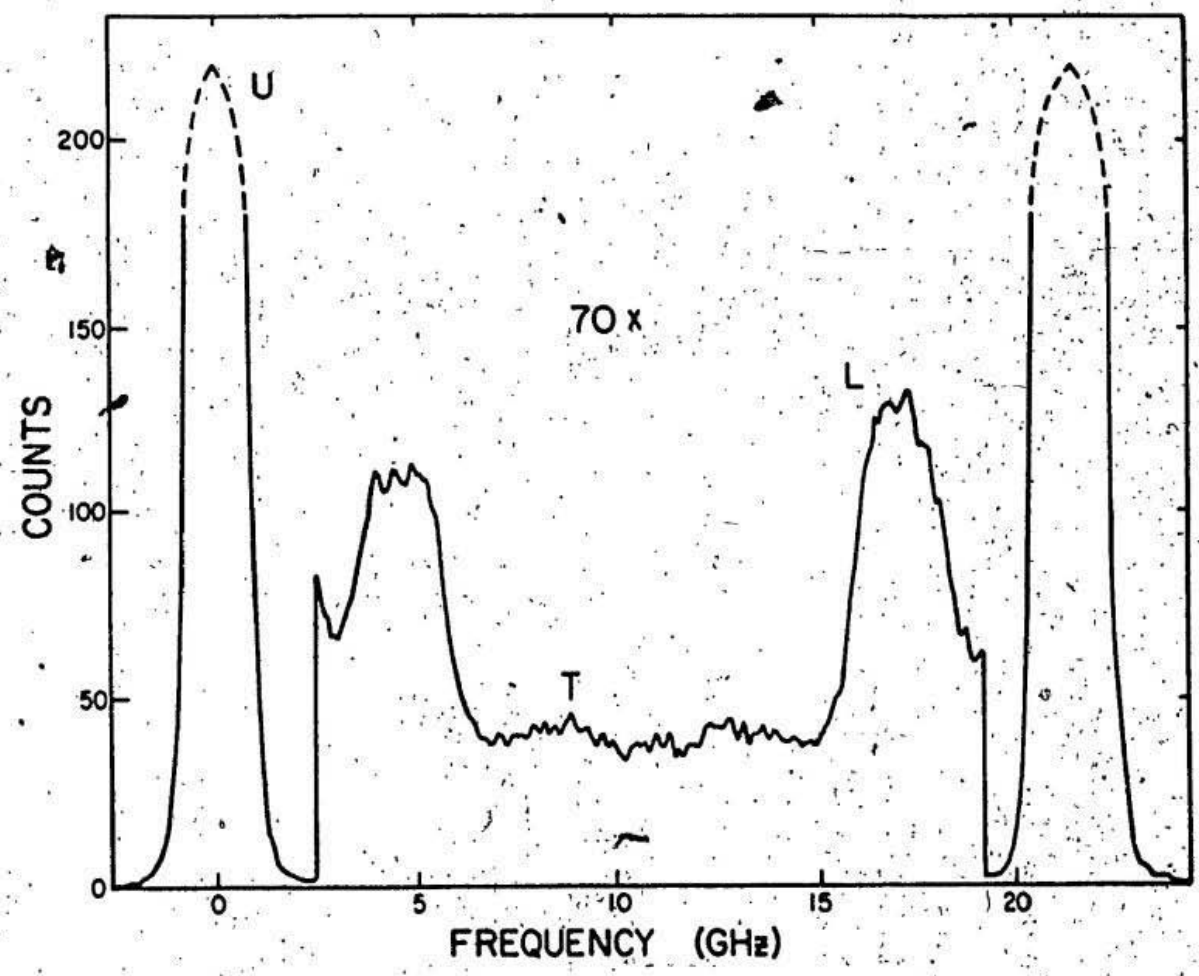

Figure 4.6

Figure 4.7. Representative Brillouin spectrum for a polycrystalline sample of ice VI at -35.5°C. One complete order is shown with two unshifted components U. The free spectral range of the Fabry-Perot is 21.51 GHz. L designates the longitudinal Brillouin component and T the transverse component as shifted from U. The region of the spectrum showing L and T has been amplified 70x in terms of data acquisition.

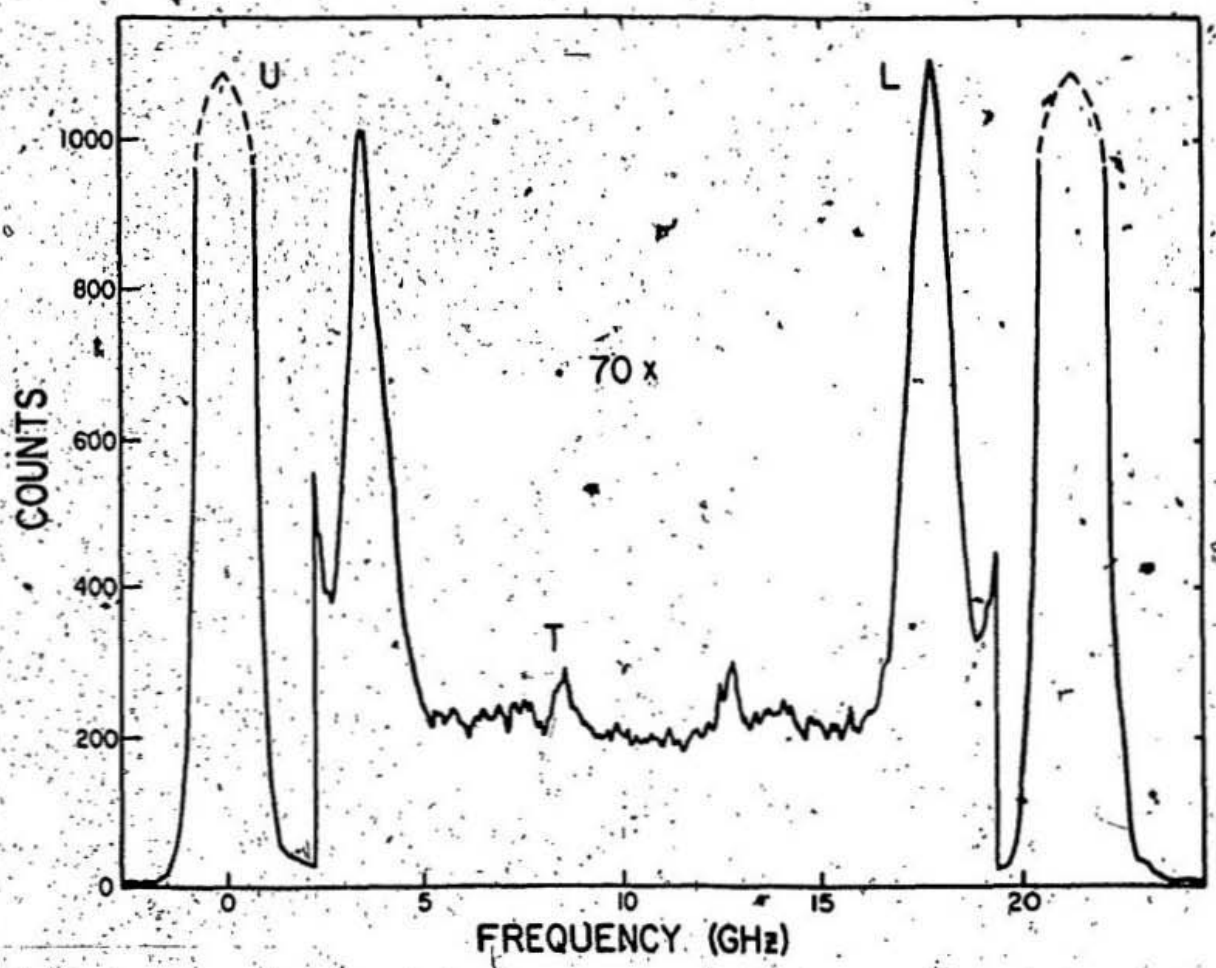

Figure 4.7

encompassed in the region of observation during each experiment. The peaks were usually quite broad, which indicated that more than one crystallite was, in the region of observation, and occasionally it became clear that at least 2 or 3 crystallites were being observed simultaneously because the longitudinal components would exhibit a multipeaked head. The region of observation was ~.2 mm in diameter, so the crystallites were probably less than .1 mm in diameter.

At a temperature setting of -35.5°C ice III, ice V, and ice VI were easily produced by raising the pressure to suitably high values. At that temperature ice III was supercooled with respect to the region of phase stability of ice II. To produce ice II it was necessary to lower the temperature further to ~-40°C while the sample was in the III phase. Then the pressure was raised to the phase transition, at ~3 kbar. As had already been observed during the density determination work, the sample appeared to transform to ice III at first. This was evident from the frequency shift spectrum. But then, within 5 hours, while the same pressure and temperature were maintained, the ice would eventually transform to ice II. The cell temperature was then brought up to -35.5°C and the light scattering experiments commenced. Thereafter it was noted that ice II was readily produced whenever the pressure and temperature fell within its region of phase stability. So it was that for a given sample the readiness with which ice II could be produced depended strongly on whether the sample had already been converted to ice II in the glass cell at some other point in its history. This phenomenon was previously noted in the original work of Bridgman,[70] and also during thermal conductivity experiments by Ross et al.[146] Another observation regarding the general solid phase behavior of water was

that as pressure was increased, any ice phase, except ice II, could be made to extend part way into the region of phase stability of the next higher phase. On a number of occasions ice V was pressurized to ~8 kbar at -35.5°C, however, within ~1 hour it would transform to ice VI. On the other hand, as the pressure was decreased no phase extended beyond its own boundary. Also, ice II could not be superheated with respect to ice III.

Another reason why the temperature of the cell had to be varied was related to the difficulty experienced in rotating the samples at high pressure. This was caused by the marked increase in viscosity of the Monoplex oil pressure medium at high pressures (> 5 kbar) and low temperatures. This condition was so severe at the highest pressures that the force applied to the rotation stem on one occasion had inadvertantly sheared off the pin in the stem which fitted into the slot of the sample holder. After this had happened, rotation of the sample was impossible, even at lower pressures. This accident led to the dismantling of the whole rotation stem assembly so that the pin could be replaced.

To combat this problem, two approaches were taken which, when combined, permitted the collection of averaged longitudinal frequency shifts at high pressure. One approach was to raise the temperature of the cell and Monoplex oil medium in order to reduce the oil's viscosity so that the sample could be rotated. At pressures greater than 6 kbar, ice VI was stable to temperatures up to ~20°C, so that the temperature was safely elevated to 10°C, and the set of experiments, at the 8 different sample orientations, were run to obtain an averaged longitudinal frequency shift. This shift was then temperature corrected

back to -35.5°C by recording the shift at one orientation at the higher temperature, and then reducing the temperature back to -35.5°C, without altering the orientation, and measuring the shift again. From the two measurements, a fractional change in frequency shift, due to the change in temperature, could be calculated. The averaged frequency shift was then multiplied by this factor to obtain a reasonably accurate value of the shift at -35.5°C. This method yielded consistent results when performed at various pressures within the phase stability region of ice VI.

Since ice III could not be supercooled once ice II had been present in the cell, the light scattering data for ice III had to be collected while the sample was at a temperature of -27.2°C, which was a higher temperature than the experiments on the other ice phases. The density data, however, which were used in the Brillouin equation to convert the frequency shifts to acoustic velocities, had been obtained at -35.5°C for ice III. No attempt was made, however, to temperature correct the density before using it in the velocity calculations for ice III since, based on the temperature dependence of density for ice Ih, only an exceedingly small correction would result in the velocity, < .05%, which was negligible in light of the overall uncertainties in the experiments.

The other technique, used in conjunction with the method just described, was to obtain an averaged frequency shift at the highest pressure and then, at the orientation at which the last of the 8 measurements had been made, to slowly reduce the pressure, being careful not to move the apparatus so that the laser beam did not change its position in the sample, to a lower setting and measuring the new

frequency shift. The fractional change in frequency shift, due to the change in pressure, was multiplied by the averaged shift obtained at the highest pressure to yield a value for the average shift at the lower pressure setting. In a similar manner the pressure was reduced further and more averaged frequency shifts were obtained.

Four of the averaged frequency shifts for ice VI, and also 1 from ice V, were obtained using the methods described above.

4.4 Analysis of the Data for the High Pressure Ice Phases

Upon examination of the data presented in Tables 4.3 to 4.6, and their graphic representations illustrated in Figure 4.8 and Figure 4.9, the most striking features are the drop in longitudinal velocity in ice III compared with ice Ih, though the density increased by ~20%, and the high velocity of ice II relative to that of ice III and ice V, though the density of ice II was only slightly higher than ice III and less than ice V. In the efforts made to explain these, and other general features, the following picture, based on stiffnesses of the hydrogen bonds, emerged.

The factors that appear to influence the velocity of acoustic waves in the various solid phases of water studied here are: 1. The density which, as it increases, stiffens the ice by either shortening and stiffening the hydrogen bonds within a given phase, or increasing the number of bonds per unit volume at a phase transition, though not necessarily shortening them. A bond of a given stiffness requires more force to compress or bend it than one of a lesser stiffness. Within any given ice phase, the O-O-O angles do not alter significantly with the application of pressure and only very slight changes, if any, occur

Figure 4.8. Brillouin frequency shifts versus pressure for the various ice phases. L and T designate longitudinal (averaged) and transverse (single-point) frequency shifts. The solid lines represent linear least squares fits (equations (4-14), (4-15), (4-16) and (4-17)) to the data (x's, dots and crosses) for each high pressure phase. The boxed points and best-fit curves shown for ice Ih were obtained from the Brillouin equation (1-9) after applying the averaging procedure of Section 3.6 to the velocity equations (1-5), (1-6) and (1-7) using the best-fit elastic constants for Mendenhall ice. All of the data were obtained at -35.5°C, except for ice III, which were obtained at -27.2°C.

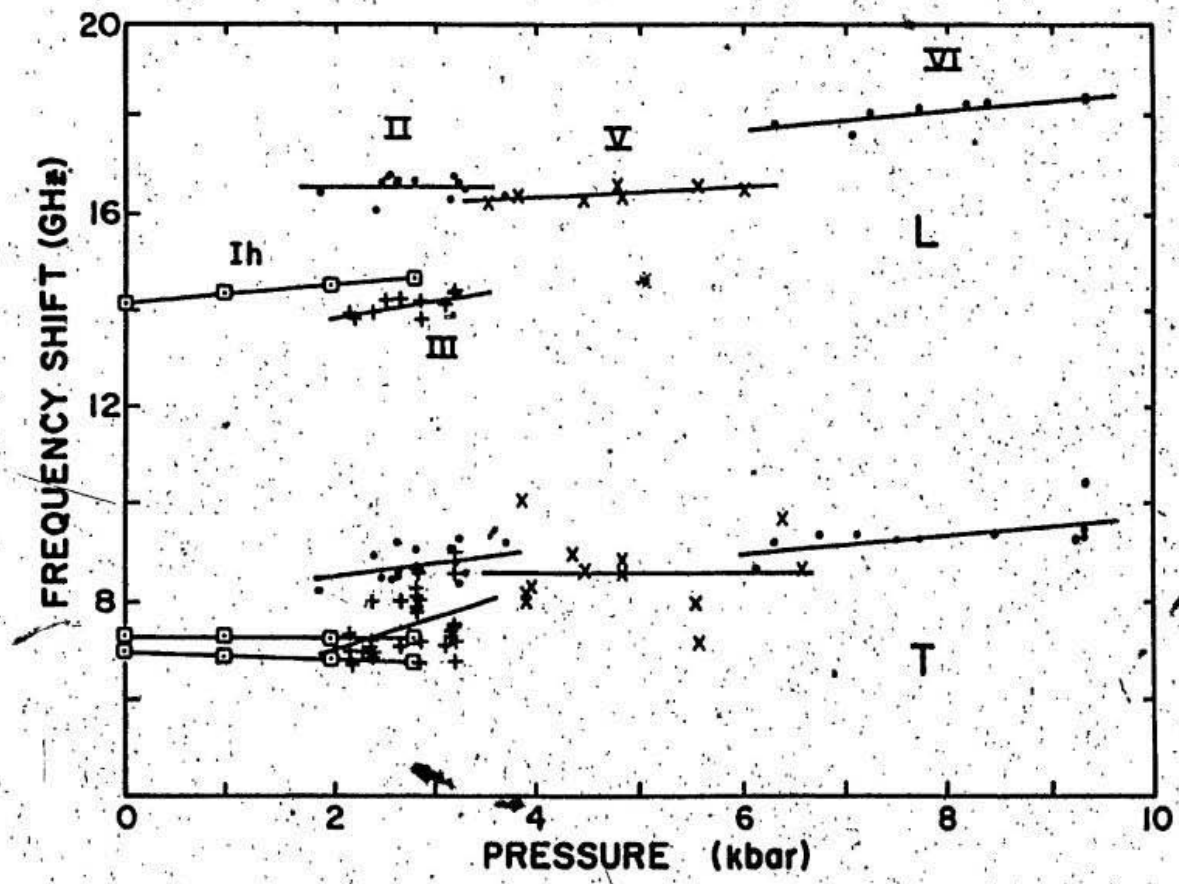
20
16
12
8
FREQUENCY SHIFT (GHz)
0
2
4
6
8
10
PRESSURE (kbar)
VI
II
V
L
Ih
III
T

Figure 4.8

Figure 4.9. Acoustic velocities versus pressure for the various ice phases. L and T designate longitudinal (averaged) and transverse (single-point) velocities. The solid lines represent linear least squares fits, equations (4-14) to (4-17), to the data (x's, dots and crosses) for each high pressure phase. Circles and triangles represent data from Shaw[119] (1986) at -25°C. The boxed data points and best-fit curves shown for ice Ih were obtained from the elastic constants determined in Section 3.4. All of the present velocity data were obtained at -35.5°C, except for ice III, which were obtained at -27.2°C.

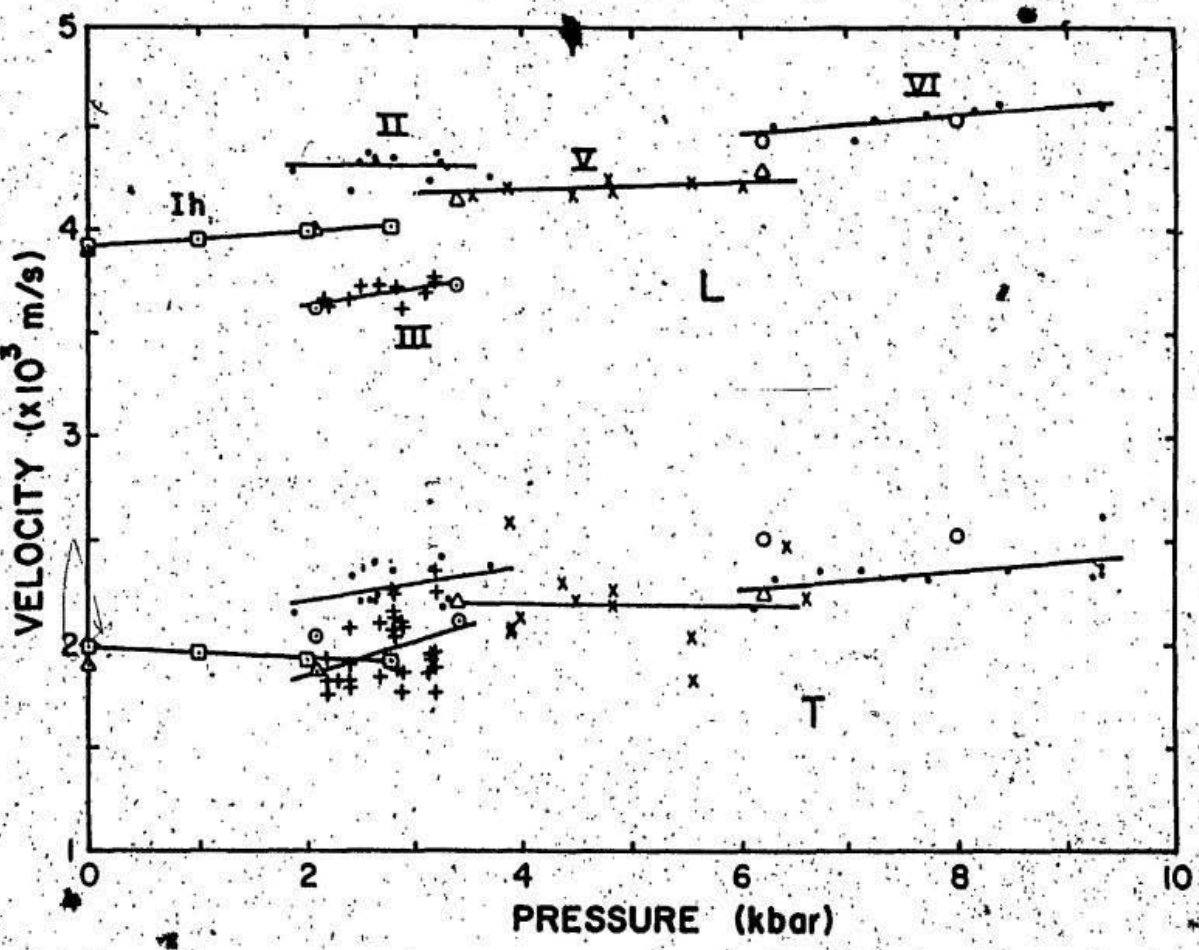
VELOCITY (x10^3 m/s)
PRESSURE (kbar)
Ih
II
III
V
VI
L
T
0
2
4
6
8
10
1
2
3
4
5

Figure 4.9

in the O-H...O-and H-O-H angles. In the Raman spectroscopic studies of Sukarova et al.,[147] it was suggested that hydrogen bonds shortened and strengthened within any given ice phase, as pressure was increased, up until the point of a phase transformation, which seemed to lengthen and proportionally weaken the bonds. The number of bonds per unit volume necessarily increases with the abrupt increase in density which accompanies a phase transition. 2. The angular relationships between the molecules within the ice which determine whether, and to what extent, the O-H...O bond deviates from linearity. Any deviation from the ideal tetrahedral arrangement of molecules will lead to some bond bending which in turn reduces the stiffness of the ice. 3. Whether the ice phase is proton ordered or not. The stiffnesses of the hydrogen bonds of a given ice structure seem to be greater if the protons are ordered, that is, if each proton remains fixed at one site rather than having some probability of being located at more than one site. The reason for this apparent phenomenon in ice is unclear and the present work makes no attempt to give a detailed molecular interpretation.

The different ice phases studied here can be classified according to the above considerations. The ices II, III, V, and VI are all composed of distorted tetrahedrons where the O-H...O bond angles deviate considerably from linearity, since the O-O-O angles vary from the ideal tetrahedral angle of ~109°. The ranges of O-O-O angles within the structures of ice II, ice III, ice V and ice VI are 80°-128°, 92°-144°, 84°-128° and 76°-128° respectively. Because the ranges are comparable, the dependence of acoustic velocity on density might be expected to be similar for all these ices. Ice II, however, would be an exception, and therefore in a separate class, because it is proton

ordered, whereas the other ices are disordered. Ice Ih is also disordered, however its molecules are arranged very close to the ideal tetrahedral structure so that all of its hydrogen bonds are linear.

Three classes serve to distinguish these five ices. Class 1 encompasses those ices which are proton disordered with near linear hydrogen bonds. Ice Ih belongs to this class. The ices III, V, and VI belong to Class 2, which are disordered ices which have O-H...O bonds that deviate from linearity by comparable degrees. Class 3 contains proton ordered ices which have nonlinear hydrogen bonds. Ice II belongs to Class 3.

Birch has suggested,[148,149] and demonstrated in ultrasonic experiments on various rocks, that the density and velocity of compressional waves are linearly related for solids of constant mean atomic weight, where the mean atomic weight is defined as the sum of the atomic weights divided by the number of atoms. As a test of this hypothesis, the density of ice Ih was plotted against the velocity of longitudinal waves in polycrystalline aggregates. The average velocities were determined from the elastic constants of ice Ih at various pressures using the averaging procedure described in Section 3.6. The linear correlation was excellent. The equation relating the density to the longitudinal velocity is given by,

$$\bar{V}_L = .457 + 3.749\,\rho \qquad (4\text{-}10)$$

where the velocity is in km/s and density is in g/cm^3.

The same test was then applied to the longitudinal velocity results of Shaw[119] for aggregates of ice III and ice V. Shaw's data were used because those experiments were conducted on large

polycrystalline samples which exhibited little scatter in the longitudinal velocities, whereas the present results had more scatter. The density and velocity within each phase again exhibited linear behaviour, but with somewhat different slopes. These results prompted a similar test to see if a linear trend was present even when phase transformations occurred. The longitudinal wave velocities from the present work, corresponding to the pressure at the midpoint of the three sets of density data for the ices III, V, and VI, which are Class 2 ices, were plotted against the associated densities, and again a good fit was obtained. All three points were situated to within 1% of the line to which they were least squares fitted (Figure 4.10). The linear relationship was expressed by,

$$\bar{V}_L = -1.400 + 4.390\,\rho \qquad (4\text{-}11)$$

where the velocity and density have units of km/s and g/cm^3 respectively.

Another way of stating (4-11) is to write,

$$\bar{V}_L = a + b\rho = a + cN \qquad (4\text{-}12)$$

where a, b and c are constants, and N denotes the number of hydrogen bonds per unit volume. The velocity is proportional to N. For any given solid phase the number of bonds per unit volume increases as pressure is increased by shortening of the bonds. When a phase transition occurs from one ice to another of the same class, the bond number density N changes proportionally with the mass density, not by bond length changes, but rather as a consequence of the new more closely packed crystal structure.

Figure 4.10. Averaged longitudinal velocity versus density for the various ice phases. The solid line represents a linear least squares fit to the velocities of the Class 2 ices. The data point for ice VII was obtained by Polian and Grimsditch[11] (1983) at -20°C. The velocity for ice Ih was taken from the data for Mendenhall ice in Section 3.6.

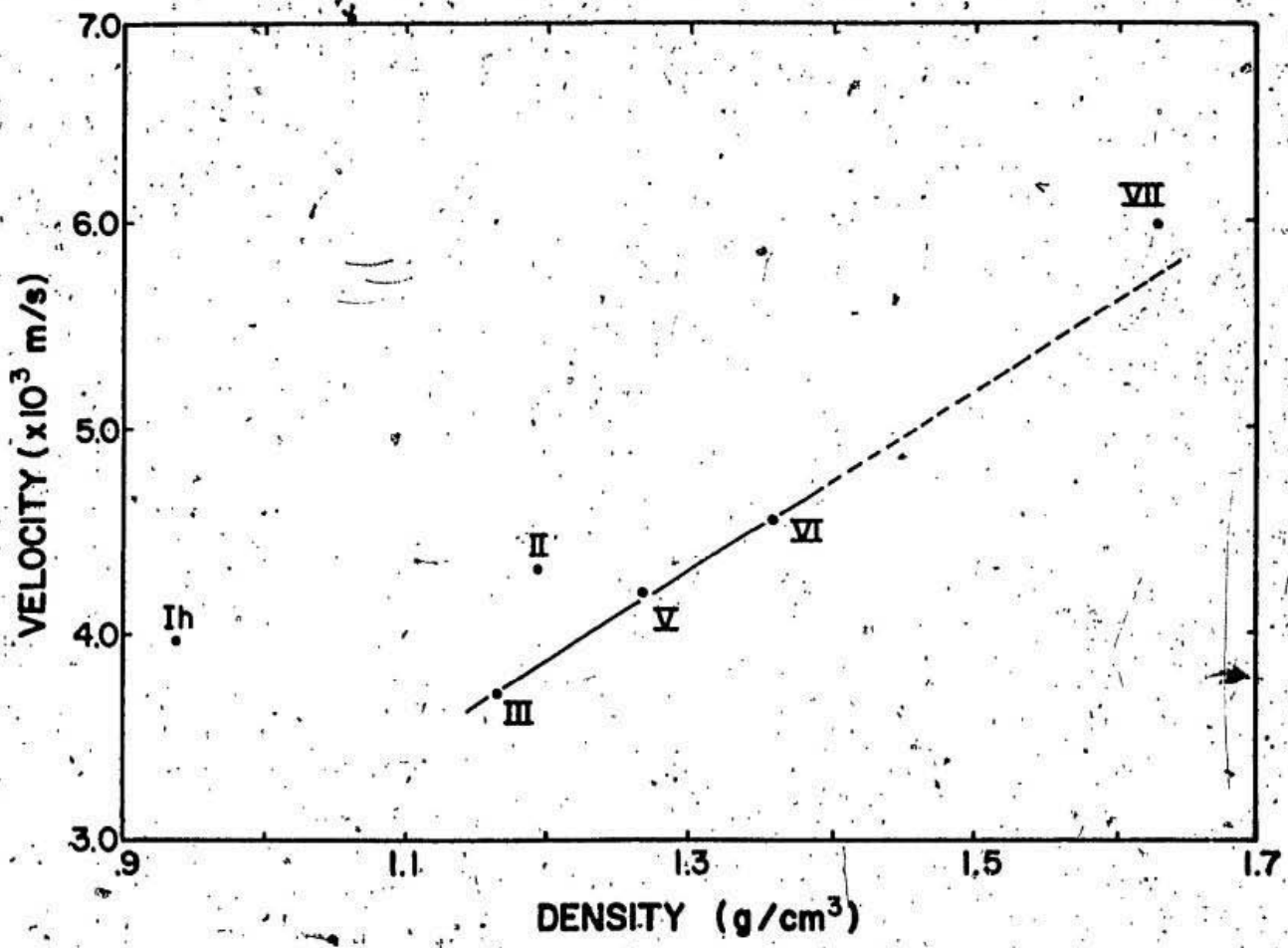
7.0
6.0
5.0
4.0
3.0
VELOCITY (x10^3 m/s)
.9
1.1
1.3
1.5
1.7
DENSITY (g/cm^3)
Ih
II
III
V
VI
VII

Figure 4.10

The ices III, V, and VI are of the same category, Class 2, and apparently abide by the velocity-density relationship suggested by Birch. The failure of ice II, a Class 3 phase, to fall on the same line connecting the velocities of these ices is explained by the fact that ice II is proton ordered , which implies that it has stiffer hydrogen bonds than if it were disordered. Its velocity would therefore be expected to lie somewhere above the line, which it does. Ice Ih is a proton disordered phase, however, its O-H...O bonds are near linear and consequently stronger than if the bonds were distinctly nonlinear. It belongs to Class 1. Of all the ices studied here, ice Ih has the shortest hydrogen bonds, which would also tend to make them strong. These two features of ice Ih lead to the expectation that its longitudinal velocity would lie well above the velocity-density line of ices III, V, and VI, which it does.

To further test the validity of expressions (4-11) and (4-12) and the proposed classification scheme, more velocity data on other ice phases would be required. Unfortunately, no velocity studies have been conducted on ice IV, which is the only other Class 2 ice, though there are velocity data on ice VII from the Brillouin spectroscopic studies of Polian and Grimsditch.[116] Ice VII is also a disordered phase, with O- H...O bonds that are linear. This puts it in Class 1, however, some distinction has to be made between this ice and ice Ih because the hydrogen bonds of ice Ih are short whereas those of ice VII are long by comparison. Therefore Class 1 will refer to disordered ices with short linear bonds, to which ice Ih belongs, and Class 1_b refers to disordered ices which have moderate-to-long linear bonds, such as ice VII. The velocity for ice VII would be expected to lie above the line

defined by expression (4-11), since this phase would have stronger hydrogen bonds. The increase in bond strength due to ordering, however, may in fact be counterbalanced somewhat because the bonds are quite long, so that the velocity may be close to the velocity-density line of the Class 2 ices. The velocity result for ice VII at ~25 kbar, from the experiments of Polian and Grimsditch,[116] was ~4% higher than the corresponding value given by expression (4-11), even though the studies were performed at a temperature which was 55°C higher than the present work. Higher temperatures yield lower velocities so that the experimental value obtained by Polian and Grimsditch would be higher still if measured at the temperature of the present work, -35.5°C. This confirms the prediction that ice VII should have a velocity which lies above, and probably close to, the velocity-density line of Class 2 ices.

It is interesting to note that ice IV belongs to Class 2 and has a density comparable to that of ice V. If the classification scheme is accurate then it is possible that ice IV may have been produced at times during these experiments and gone undetected because no noticable change occurred in the velocity results during the light scattering experiments or in the sample volume during the density experiments on ice V.

Ice VIII belongs to yet another class of structures, those which are proton ordered with linear hydrogen bonds, designated as Class 4. Ice Ic, though disordered, has short and linear O-H...O bonds, similar to ice Ih. In fact ice Ic and ice Ih belong to Class 1_a. Ice IX and Ice II also belong to one class, Class 3. Ice VIII would be expected to lie well above the velocity-density line given by (4-11), as would Class 1_a

ices like ice Ih and ice Ic. Furthermore, if the scheme holds true, the velocities for ice Ih and ice Ic should be comparable since the densities are almost the same. The velocity of ice IX would be expected to lie above the velocity-density line of Class 2 ices and slightly lower than the velocity of ice II because its density is lower. No velocity data exist on ice Ic, ice IX, or ice VIII, however, thermal conductivity measurements have been made by Ross et al.[146]

For comparison with the velocity data of Figure 4.10, the thermal conductivity-versus-density data of Ross et al.,[146] corresponding to a temperature of 240 K, have been reproduced in Figure 4.11. Some of the points for the low temperature phases have been extrapolated, of course. A straight line has been fitted to the Class 2 ice conductivities. Clearly, the two figures (Figure 4.10 and 4.11) are remarkably similar. There is very good qualitative agreement in the inter-phase relationships for conductivity and velocity for ices Ih, II, III, V, VI, and VII.

The thermal conductivity may be written as,

$$\lambda \approx \sum c_i v_i l_i \qquad (4\text{-}13)$$

where λ denotes thermal conductivity, c is the heat capacity, v is the velocity of sound and l denotes the mean free path for mode i. Since the pattern of longitudinal velocities is qualitatively reflected in the thermal conductivity data it is clear that the product of the heat capacity and the mean free path do not change significantly, or at least vary proportionally with v, from phase to phase. This implies that the main parameter governing the thermal conductivity, for the ices studied in this thesis, is the acoustic velocity. In particular,

Figure 4.11. Thermal conductivity versus density for nine ice phases at 240 K. The thermal conductivity values for phases Ic, VII and IX were obtained by extrapolation in temperature. The density for ice Ic was taken from [150], the density for ice VII (ice VIII was assumed to have the same value) from [116] and the density of ice IX was assumed to be the same as the present value for ice III. Thermal conductivities for all the phases were taken from Ross et al.[146] (1977).

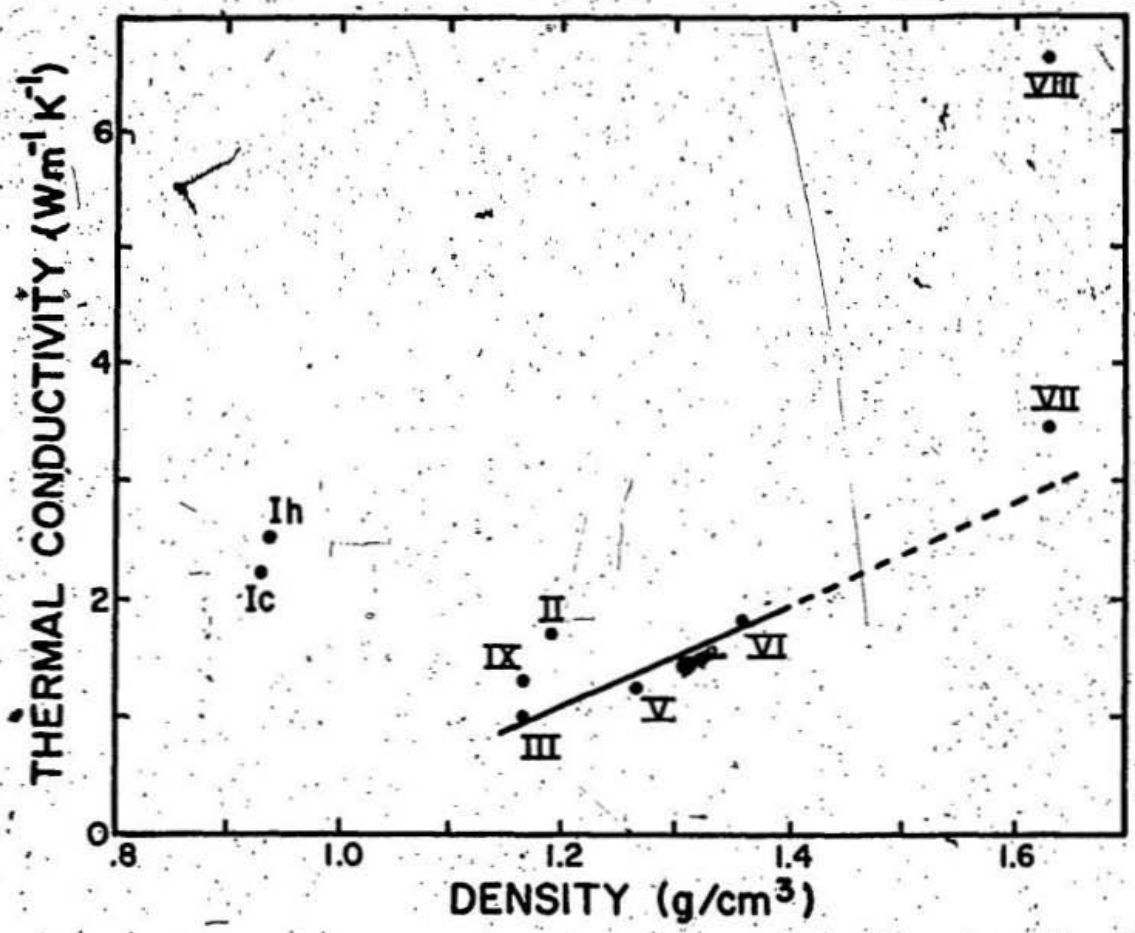
THERMAL CONDUCTIVITY (Wm⁻¹K⁻¹)
DENSITY (g/cm³)
0
2
4
6
.8
1.0
1.2
1.4
1.6
Ih
Ic
II
III
IV
V
VI
VII
VIII
IX

Figure 4.11

it indicates that λ varies directly as v in ice. This interesting result can be exploited to obtain reasonable estimates for acoustic velocities for other ice phases, to further test the classification scheme, if thermal conductivity data are available.

The thermal conductivity of ice VIII[146] is well above the conductivity-density line of the Class 2 ices, so it is expected that v for ice VIII will lie well above the velocity-density line of this class. This agrees with the classification scheme which predicts that ice VIII will have a velocity considerably higher than the Class 2 ices. Similarly, the conductivity, and hence velocity, for ice Ic are comparable to ice Ih. This was also predicted by the classification scheme. The temperature extrapolated conductivity of ice IX lies between the conductivity-density line of the Class 2 ices and ice II. A similar relationship can be expected for the velocities, and again agrees with the classification scheme.

The fact that the thermal conductivity of ice VIII lies well above that of ice VII, where the only difference according to the scheme is that one is ordered and the other is not, and also that ice II is only moderately higher than ice III for the same reason, implies that proton ordering has a more dramatic effect on acoustic velocity and thermal conductivity in ices that have linear hydrogen bonds.

Tables 4.7 and 4.8 contain crystallographic data on most of the ice phases. Table 4.8 also includes the classification of each phase according to the classification scheme presented here. Assuming that the velocity-density slopes of the different classes are similar, the different classifications can be ranked from highest to lowest velocity as follows. Classes 1_a and 4 are 1st rank, Classes 1_b and 3 are 2nd

TABLE 4.7

STRUCTURAL DATA, AND CLASSIFICATION ACCORDING TO THE PRESENT SCHEME, FOR THE POLYMORPHS OF ICE

Phase	Class	Distance of Nearest Neighbours (Å)†	O-O-O angles (deg.)†	Hydrogen Positions	References
Ih	1_a	2.74	109±0.2	Disordered	Peterson and Levy[151] (1957)
Ic	1_a	2.75 at -130°C	109.[illegible]	Disordered	Shimaoka[152] (1960), Bertie et al.[82] (1963)
II	3	2.75-2.84	80-128	Ordered	Kamb et al.[153] (1974)
III	2	2.76-2.80	87-14[illegible]	Disordered	Arnold et al.[154] (1971)
IV	2	2.79-2.92	88-128	Disordered	Engelhardt and Kamb[85] (1981)
V	2	2.76-2.87	84-128	Disordered	Hamilton et al.[155] (1969)
VI	2	2.80-2.82	76-128	Disordered	Kamb[86] (1965)
VII	1_b	2.95	109.5	Disordered	Weir et al.[156] (1965)
VIII	4	2.96 (hydrogen bonded) 2.80 (non-bonded neighbours) 3.15 (non-bonded distant neighbours)	≈109.5	Ordered	Kamb and Prakash (unpublished)
IX	3	2.76-2.80	87-140	Ordered	La Placa et al.[157] (1973)

† Reduced to values at atmospheric pressure and -163°C unless otherwise noted. Included mainly for comparison.

TABLE 4.8

STRUCTURAL DATA ON THE POLYMORPHS OF ICE

Phase	Crystal System	Space Group	Unit Cell Dimensions(Å)†	Number of Molecules in a Unit Cell	Number of Nearest Neighbours
Ih	Hexagonal	$P6_3/mmc$	a_0=4.50 c_0=7.32	4	4
Ic	Cubic	Fd3m	a_0=6.35	8	4
II	Rhombohedral	$R\bar{3}$	a_0=7.79 α=111.3°	12	4
III	Tetragonal	$P4_12_12$	a_0=6.73 c_0=6.83	12	4
IV	Rhombohedral	$R\bar{3}c$	a_0=7.60 α=70.1°	16	4
V	Monoclinic	A2/a	a_0=9.22 b_0=7.54 c_0=10.35 β=109.2	28	4
VI	Tetragonal	$P4_2/nmc$	a_0=6.72 c_0=5.79	10	4
VII	Cubic	Pn3m	a_0=3.43	2	8*
VIII	Tetragonal	$I4_1/amd$	a_0=4.80 c_0=6.99	8	8*
IX	Tetragonal	$P4_12_12$	a_0=6.73 c_0=6.83	12	4

† Reduced to values at atmospheric pressure and -163°C. Included mainly for comparison.
* Four of the nearest neighbours are hydrogen-bonded to the central molecule.

rank and Class 2 ices are 3rd rank. Table 4.9 summarizes the classification scheme and assigns the appropriate rank to each class.

4.5 Comparison with Previous Studies

The only other Brillouin scattering work performed on high pressure phases of ice was that of Polian and Grimsditch.[90,116] Their value for the compressional wave velocity of ice VI[116] was in excellent agreement, to within 1%, with the present result.

Recently, ultrasonic velocity studies have been conducted by Shaw[119] on ices Ih, III, V, and VI. The experiments were performed on pressurized polycrystalline aggregates at -25°C. Average longitudinal and shear acoustic velocities were measured in the pressure range 0 kbar to 8 kbar using the pulse transmission method. For comparison, data points from Shaw's results have been included in the graphic depiction of the present velocity data (Figure 4.9). Straight lines have been least squares fitted to the averaged longitudinal shifts/velocities and also to the unaveraged single-point transverse data. They are given below.

ICE II (4-14)

$$\bar{\Omega}_L(P) = (16.5213 + .0080 \times P)\ \text{GHz}$$
$$\bar{V}_L(P) = (4.3233 - .0060 \times P)\ \text{km/s}$$
$$\Omega_T(P) = (7.9653 + .2728 \times P)\ \text{GHz}$$
$$V_T(P) = (2.0850 + .0669 \times P)\ \text{km/s}$$

ICE III (4-15)

$$\bar{\Omega}_L(P) = (13.1030 + .3654 \times P)\ \text{GHz}$$
$$\bar{V}_L(P) = (3.4610 + .0853 \times P)\ \text{km/s}$$
$$\Omega_T(P) = (5.6966 + .6705 \times P)\ \text{GHz}$$
$$V_T(P) = (1.5065 + .1705 \times P)\ \text{km/s}$$

TABLE 4.9

ICE POLYMORPH CLASSIFICATION AND HIGHEST TO LOWEST VELOCITY RANK

Class	Rank	Ice Phases
1_a	1	Ih, Ic
1_b	2	VII
2	3	III, IV, V, VI
3	2	II, IX
4	1	VIII

$$\bar{\Omega}_L(P) = (15.8792 + .1130 \times P)\ \text{GHz}$$
$$\bar{V}_L(P) = (4.1075 + .0203 \times P)\ \text{km/s}$$
ICE V (4-16)
$$\Omega_T(P) = (8.5881 + .0040 \times P)\ \text{GHz}$$
$$V_T(P) = (2.1976 + .0006 \times P)\ \text{km/s}$$

$$\bar{\Omega}_L(P) = (16.5051 + .2074 \times P)\ \text{GHz}$$
$$\bar{V}_L(P) = (4.1931 + .0456 \times P)\ \text{km/s}$$
ICE VI (4-17)
$$\Omega_T(P) = (7.8139 + .1977 \times P)\ \text{GHz}$$
$$V_T(P) = (1.9871 + .0463 \times P)\ \text{km/s}$$

Where $\bar{V}_L$ denotes the longitudinal velocity, at pressure P(kbar), for the line fitted to the averaged data points and V_T is the transverse velocity for the line fitted to the unaveraged data points.

Even though averaged transverse velocities were not obtained at any of the individual pressures within the phase regions of the high pressure polymorphs, there is good reason to believe that the midpoints of the lines, at least, do actually represent reasonably accurate transverse wave velocities for isotropic ice aggregates. Two features of the data support this assumption. First of all, bearing in mind the range of transverse velocities observed in single crystals of ice Ih, it was noted that a roughly comparable range of values was exhibited in the present transverse data for all ices. This degree of scatter would seem to imply that the full range of possible values was adequately represented. Secondly, the transverse data appear to be fairly uniformly distributed above and below the least squares lines. This indicates that the range of possible transverse velocities is also evenly represented, so that the averaged velocities taken near the midpoints of the lines are very likely free of any significant bias

towards high or low values.

As Figure 4.9 indicates, the agreement between the present results and those of Shaw[119] for longitudinal average velocities is excellent, considering the very different experimental techniques used. Shaw's data for longitudinal acoustic waves falls within 1% of the averaged values determined for the various ices in this work. There was some disagreement, however, between the two sets of transverse data. Shaw's transverse velocities at zero pressure were definitely low compared to values obtained in most other ultrasonic studies (e.g. Proctor[106] and Brockamp and Querfurth[104]), and were certainly low compared to the values obtained from Brillouin scattering experiments.[126] As has already been pointed out in the discussion of the results on single crystals of ice Ih (Section 3.5), measuring techniques which employ ultrasonic transducers often suffer from error related to the coupling of the transducers to the samples. Transverse acoustic measurements are much more affected by this problem than longitudinal measurements, especially when the sample and/or the transducers are subjected to pressure. Shaw's ice specimens were encased in lead foil and placed between steel endplugs, to which the transducers were attached. To account for the offset time associated with the acoustic pulses travelling through the steel plugs, Shaw put the plugs face to face, without a sample in between, and determined the endplug travel time offset for the whole pressure range. There could be no guarantee, however, that the steel-lead-ice coupling, which was quite different from the steel-steel coupling, would not alter the offset for shear wave transmission. It is conceivable that even the different textures of the various ice polymorphs could influence the nature of the

acoustic coupling for shear waves. This may account for the discrepancies observed between Shaw's data and the present results for transverse acoustic waves.

One suggestion as to how difficulties of this nature could be overcome in ultrasonic experiments is that samples of various lengths be used, so that the true offset for any pressure could be obtained from the intercept of the plot of (travel time) versus (sample length). Though perhaps more time consuming, this method would yield more accurate absolute shear wave velocities.

Tables 4.10 and 4.11 represent a synopsis of the present data, and how it compares with Shaw's results. The adiabatic (constant entropy) bulk modulus, B^S, for both sets of data was calculated from the well known expression,

$$B^S = \rho(\bar{V}_L^2 - {}^4/_3 \bar{V}_T^2) \qquad (4\text{-}18)$$

where ρ denotes density (given according to equations (4-2) to (4-6) from the density determination work), and $\bar{V}_L$ and $\bar{V}_T$ are the average longitudinal and transverse acoustic wave velocities respectively. Given the uncertainties associated with the velocities of the two acoustic modes, the expected uncertainty in the bulk modulus given by (4-18) is ~5%. The isothermal (constant temperature) bulk modulus, B^T, from the present density data, was determined using the expression,

$$B^T = \rho \, dP/d\rho \qquad (4\text{-}19)$$

where P denotes pressure.

The adiabatic shear modulus, μ, was calculated from the following expression,

TABLE 4.10

COMPARISON OF THE PRESENT RESULTS ON THE ICE POLYMORPHS WITH RECENT ULTRASONIC DATA

		PRESENT STUDY (-35.5°C)				SHAW[119] (1986) (-25°C)		
Phase	Pressure (kbar)	Average Velocity (km/s)		Bulk Modulus ($\times 10^4$ bar)		Average Velocity (km/s)		Bulk Modulus ($\times 10^4$ bar)
	P	$\bar{V}_L$ ±1.5%	$\bar{V}_T$ ±3.5%	B^S ±5%	B^T	$\bar{V}_L$	$\bar{V}_T$	B^S
Ih	1.40	3.97	1.96	9.96	9.61	3.96	1.88	10.25
II	2.83	4.31	2.28	13.89	14.39	--	--	--
III	2.76	3.70	1.98	9.87	9.60	3.67	2.07	8.90
V	4.80	4.20	2.20	14.19	13.86	4.21	2.23	13.84
VI	7.77	4.55	2.35	18.14	18.48	4.52	2.53	15.88

Notes 1. B^S and B^T denote adiabatic (constant entropy) bulk modulus and isothermal (constant temperature) bulk modulus. $\bar{V}_L$ and $\bar{V}_T$ refer to average longitudinal and shear wave velocities respectively. B^T values are based on the density data of the present work, whereas the B^S values are derived from the following expression,

$$B^S = \rho(\bar{V}_L^2 - 4/3\,\bar{V}_T^2)$$

where ρ denotes density.

2. The results quoted for Shaw[119] are based on linear interpolations of his data.

TABLE 4.11

COMPARISON OF THE PRESENT RESULTS ON THE ICE POLYMORPHS WITH RECENT ULTRASONIC DATA

		PRESENT STUDY (-35.5°C)		SHAW[119] (1986) (-25°C)	
Phase	Pressure (kbar)	Density (g/cm³) ±.1%	Shear Modulus (x10⁴ bar) ±7%	Density (g/cm³)	Shear Modulus (x10⁴ bar)
Ih	1.40	.937	3.6	.934	3.3
II	2.83	1.193	6.2	--	--
III	2.76	1.166	4.6	1.148	4.9
V	4.80	1.267	6.1	1.248	6.2
VI	7.77	1.360	7.5	1.336	8.5

Note: The shear modulus, μ, is defined as the product of the density, ρ, and the square of the average shear velocity:

$$\mu = \rho \overline{V_T^2}$$

$$\mu = \rho \bar{V}_T^2 \qquad (4\text{-}20)$$

where the expected uncertainty is ~%.

The bulk modulus determined according to (4-19) is very sensitive to error in the slope of density-versus-pressure, for any particular phase, and for this reason would not be considered accurate at all points along the density expressions (4-2) to (4-6), which were obtained from least square fits to the density data. However, the value determined at the midpoint of a given set of density data, for any particular phase, should yield a reasonably accurate estimate for the isothermal bulk modulus. In the present experimental results, the validity of this assumption, and also the reliability of the present averaged shear wave velocities, could be checked by comparing the bulk modulus obtained using the velocity data in expression (4-18) with the values obtained using the density data in conjunction with equation (4-19).

The pressures at which the calculations were carried out, quoted in the tables, correspond to the pressures at the midpoints of the density data sets for ice II, III, V, and VI. The pressure associated with ice Ih is the average of the pressures which were used during the determination of the elastic constants, rather than the mid pressure of the density data. The density expression (4-2) for ice Ih is deemed to be more accurate at this higher pressure because of possible error in the pressure reading, at zero pressure, due to nonlinear O-ring friction behaviour in the pressure intensifier. If the zero pressure data points are left out when the least squares fitting procedure is applied to the density data for ice Ih, an expression is obtained,

similar to (4-2) which yields a value for the isothermal bulk modulus at the true midpoint of the density data, which is close to that quoted for ice Ih in Table 4.10.

The consistency of the present bulk moduli obtained using the density data, as compared with that using the velocity data, is impressive. The two expressions (4-18) and (4-19) yield results that agree to within 5% for all ices studied. The best agreement is between the values for ice VI, which are within 2% of each other.

In general there is reasonable agreement, ~3-10%, between Shaw's[119] values for the bulk and shear moduli, and the present values. The discrepancy is larger (~15%), however, in the results for ice VI. All of the discrepancies are attributable to a small extent, ~1%, to the different densities that were used. Shaw used the values of Bridgman,[79] whereas a completely separate set of experimentally determined densities was used for the present analysis. By far the greatest source of discrepancy is in the values for the average shear wave velocities. This ranges from ~2-8%, where the greatest discrepancy is associated with ice VI. The consistency of the present bulk moduli results for ice VI suggests that the shear wave data are perhaps more accurate than Shaw's. Furthermore when 5 points of Bridgman's[79] density data for ice VI, centered at 7.85 kbar, are least-squares quadratically fitted to the pressure, the resulting expression for the density can be used to compute the bulk modulus. The value obtained at 7.77 kbar is 17.66 x 10^4 bar. Though Bridgman's data should certainly not be considered as the final word on ice density, this value for the bulk modulus does agree more with the present results than with Shaw's.

4.6 Brillouin Scattering Experiments on Low Temperature Ices

All of the ice phases accessible with the present high pressure apparatus have been studied. Phases which occur at much lower temperatures, such as ice Ic, IX, VIII, and amorphous ice, cannot be investigated since the high pressure cell was not designed for these temperatures. A completely different apparatus, however, has been constructed to study ices at liquid nitrogen temperatures and zero pressure.

A quenching process, whereby polycrystalline samples of various ices are formed at high pressure and then cooled with liquid nitrogen and recovered at zero pressure, has been developed and employed regularly at NRC. The intention was to ship quenched specimens of various low temperature phases, including ice Ic, from Ottawa to this lab in a liquid nitrogen bath so that Brillouin experiments could be carried out. Velocity data on ice Ic would be of interest not only because comets probably contain significant amounts of this phase (and also amorphous ice), but also because the results would provide a particularly suitable test for the classification scheme, which predicts that the velocity of acoustic waves in ice Ic will be comparable to that of ice Ih, since they are both Class I_a ices and have similar densities. Data on other low temperature phases would also be useful for testing the classification scheme.

The apparatus is shown in Figure 4.12. Essentially it consisted of a liquid nitrogen reservoir (F) encased in an evacuated chamber. This was fed by a larger reservoir (A) situated above it which could be easily topped up with liquid nitrogen when necessary. Attached to the lower reservoir was a thermally conducting brass cylinder (H) which had

Figure 4.12. Cryostat for Brillouin scattering experiments on low temperature ices: A, outer liquid nitrogen reservoir; B, thin stainless steel reservoir wall ; C, O-ring vacuum seal ; D, cryostat housing ; E , thermally insulating vacuum space; F, inner liquid nitrogen reservoir; G, stainless steel tube to allow passage of the laser beam to minimize signal noise due to stray reflections within the cryostat; H, thermally conducting brass housing for sample mount; I, fused quartz window; J, spring loaded brass plate with center hole for laser beam passage; K, Beryllium copper protective casing around ice sample; L, polycrystalline ice sample; M, hole in brass bottom plate of the sample mount for passage of the laser beam; N, fused quartz window; O, laser beam.

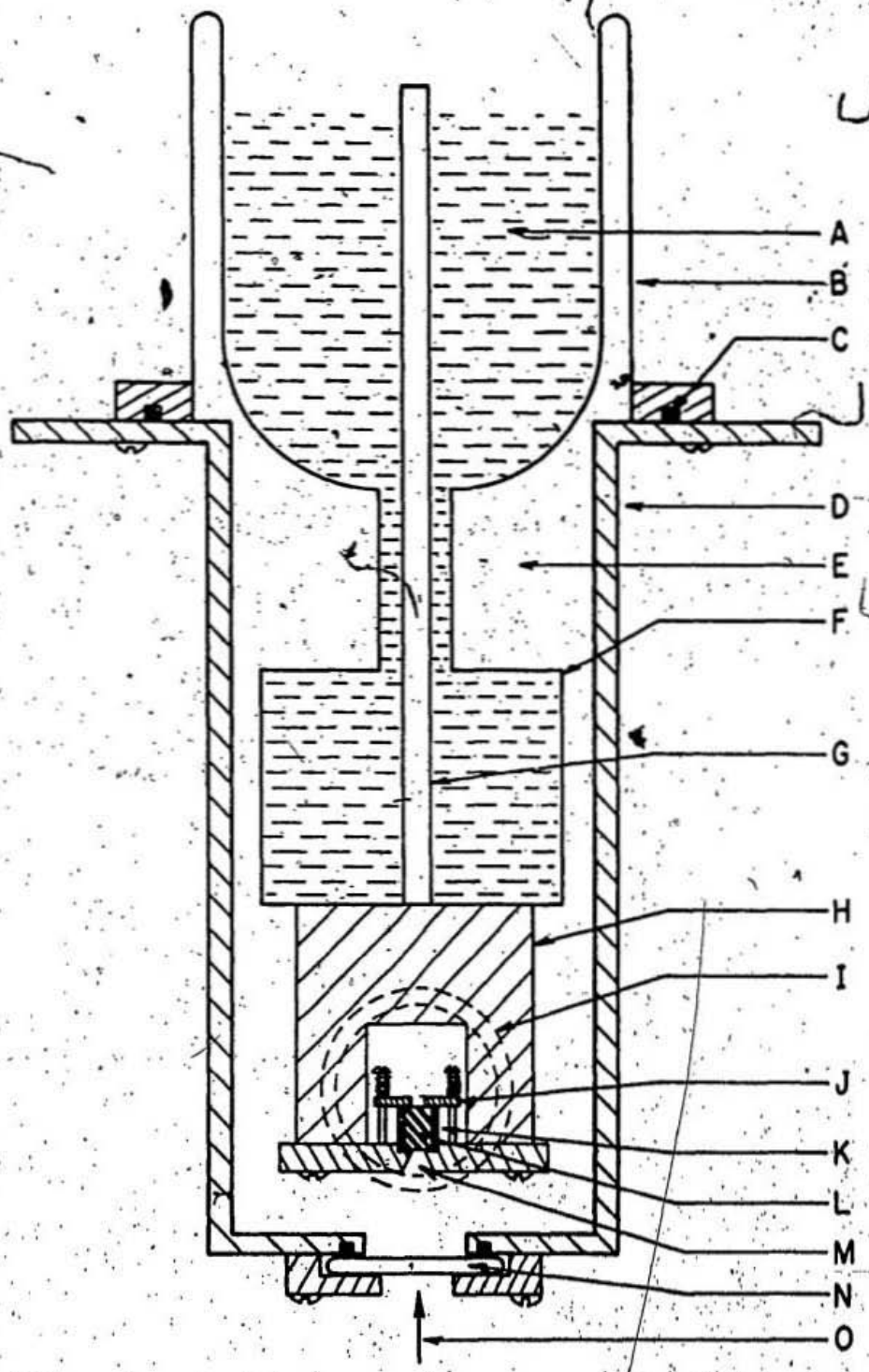

Figure 4.12

two channels cut into its wall to facilitate an unobscured optical path normal to the cylinder's axis. A circular brass plate was bolted to the bottom of the cylinder. Another smaller plate (J) was bolted and spring loaded to the center of the top of this plate. Roughly cubical specimens are produced at NRC inside angular 3 sided channels of beryllium copper so that a top, bottom and side face of the cubical samples are exposed. The intention was to have the angular channel (K), and ice specimen (L), rest at the top center of the bottom plate and be kept snugly in place by the smaller spring loaded plate above it. Small holes (M) were drilled through both plates to allow the laser beam to enter the bottom of the sample and exit through the top. After leaving the sample the beam passes on to the end of a long sealed tube (G) to minimize the spectral noise from backscattered light. Two quartz windows (I) were placed on opposing sides of the cryostat. One permitted the passage of scattered light to the optical detection system. The other was to be used primarily for quickly placing samples in the device. This window rested on an O-ring and was held in place by atmospheric pressure outside the cryostat. One other window (N) was situated at the bottom of the cryostat and served as the entrance for the laser beam (O).

A sample is inserted into the apparatus by first breaking the vacuum inside the cryostat and backflushing with dry N_2. The window, normally held on by atmospheric pressure only, falls away from the O-ring it rests on. The sample, gripped in plastic tweezers and kept in liquid N_2, is then plucked from the bath and quickly inserted through the window opening of the cryostat. It is placed at the center of the bottom plate under the spring loaded plate, which has been previously

propped up with a bent piece of copper wire. A slightly recessed slot, machined into the top of the plate, guides the sample to the exact position over the laser beam entry hole and prevents the specimen from moving sideways. When the sample is in place the tweezer grip is released and as the tweezers are withdrawn from the cryostat they catch hold of the copper wire which supports the spring loaded plate and pull it out also, so that the plate comes to rest on the sample. Then the quartz window is held against the O-ring and the cryostat is evacuated. This insertion procedure was run through with mock samples of ice Ih, for practice, and took ~5 seconds. Rapid sample transfer is necessary to prevent low temperature phases from heating and transforming to ice Ih. The speed of transfer and dry N_2 atmosphere also prevent specimens from fogging up.

Before making arrangements to have any specimens shipped to M.U.N. it was necessary to go to the NRC facility in Ottawa and determine whether the samples were of adequate optical quality for the light scattering experiments. This trip was recently undertaken (Oct. 28, 1986) and a specimen of amorphous ice was inspected. The optical quality of this specimen was representative of that which is consistently attained for most of the low temperature phases produced using the quenching technique. Ice Ic specimens turn out to be of poorer quality than other phases. According to neutron diffraction experiments, conducted by NRC, the quenched samples of crystalline phases are made up of very tiny crystallites (~.1 mm diameter), which make them suitable for obtaining averaged values for the acoustic velocities. All of the quenched samples are riddled with tiny cracks and voids.

When the amorphous ice specimen was placed in an evacuated chamber at ~77 K, similar to the environment provided by the apparatus described above, it became clear that the sample was a poor candidate for Brillouin scattering experiments. Its surface had a frosty appearance and it was only marginally translucent because of the tiny internal voids and cracks. When an argon ion laser beam was focused into the specimen the light was scattered wildly and very little seemed to pass directly through the bulk sample. These observations ruled out using the low temperature cell with its present design (Figure 4.12). The optical quality of the same specimen improved dramatically when it was immersed in liquid nitrogen. The nitrogen filled all the tiny cracks and voids in the sample and greatly reduced the specimen's frosty appearance and hence appeared to provide a reasonable refractive index match. The laser beam passed through fairly readily, though slightly scattered and somewhat spread out. It was difficult to ascertain if the spreading out of the beam was caused by the rough surface (which had only been crudely prepared with makeshift tools) of the specimen or whether it was the result of the imperfections of the bulk sample.

The conclusion drawn from the observations made at NRC was that Brillouin scattering experiments are possible on the low temperature phases as long as the specimens are immersed in liquid nitrogen. It is likely that longitudinal velocity measurements can be made, and possibly tranverse measurements, if the surfaces of the specimens are carefully prepated. A different apparatus, however, or at least major modifications to the present apparatus, would be required to conduct experiments with the samples immersed in a liquid nitrogen bath. This

other work was not deemed feasible at this time.

4.7 Concluding Remarks

In the present work Brillouin spectroscopy has proven to be an effective method for studying the elastic properties of the various solid phases of water. Data from Brillouin experiments at several pressures, coupled with orientational information supplied by a unique c-axis determination device, have been used to obtain, for the first time, the pressure dependences of the complete set of elastic constants for ice Ih throughout its full range of phase stability at -35.5°C.

It is impossible to produce single crystal samples of the other phases with the present apparatus, and consequently the full set of elastic constants for any of these ices could not be obtained. However, longitudinal and transverse acoustic velocities have been determined for isotropic polycrystalline aggregates of ice II, III, V and VI. The densities of the ices have also been measured; a new technique was developed whereby the variation of sample volume with pressure was measured in the pressure range 0 - 10 kbar.

The general features of the present velocity data have been interpreted on the basis of a proposed classification scheme which is founded on a knowledge of the hydrogen-bonding. Additional acoustic velocity data on other ice polymorphs would be useful to check the validity of the proposed scheme, in particular, velocity data for ice VIII and ice IX could be used to test the proposed effect of proton ordering on acoustic velocities. The scheme may be useful for estimating acoustic velocities (and thermal conductivities) in ice phases for which no data presently exist.

It was found that the thermal conductivities of the various solid ice phases depend directly on their acoustic velocities.

The feasibility of Brillouin scattering experiments on low temperature ice polymorphs has been studied and it was concluded that such samples would have to be housed in a cryostat enabling them to be completely immersed in liquid nitrogen. The refractive index match would render the specimens reasonably transparent, as is necessary for Brillouin spectroscopy.

REFERENCES

1. B.J. Yoon, K. Morokuma and E.R. Davidson. J. Chem. Phys. 83, 1223 (1985).

2. M.G. Sceats and S.A. Rice. J. Chem. Phys. 72, 3236 (1980).

3. M.D. Morse and S.A. Rice. J. Chem. Phys. 76, 650 (1982).

4. J.R. Reimers, R.O. Watts and M.L. Klein. Chem. Phys. 64, 95 (1982).

5. R.W. Impey, M.L. Klein and J.S. Tse. J. Chem. Phys. 81, 6406 (1984).

6. G. Nielson and S.A. Rice. J. Chem. Phys. 80, 4456 (1984).

7. G. Nielson and S.A. Rice. J. Chem. Phys. 82, 1058 (1985).

8. J.S. Tse, M.L. Klein and I.R. McDonald. J. Phys. Chem. 87, 4198 (1983).

9. J.S. Tse, M.L. Klein and I.R. McDonald. J. Chem. Phys. 81, 6124 (1984).

10. J.S. Rowlinson. Trans. Faraday Soc. 47, 120 (1951).

11. A. Ben-Naim and F.H. Stillinger. In Structure and Transport Processes in Water and Aqueous Solutions. Edited by R.A. Horne. Wiley-Interscience, New York. 1972.

12. F.H. Stillinger and A. Rahman. J. Chem. Phys. 60, 1545 (1974).

13. H.L. Lemberg and F.H. Stillinger. J. Chem. Phys. 62, 1677 (1975).

14. H. Kistenmacher, H. Popkie and E. Clementi. J. Chem. Phys. 58, 5627 (1973).

15. H. Kistenmacher, H. Popkie, E. Clementi and R.O. Watts. J. Chem. Phys. 60, 4455 (1974).

16. R.O. Watts. Chem. Phys. 26, 367 (1977).

17. P. Barnes. In Progress in Liquid Physics. Edited by C.A. Croxton. Wiley, New York. 1978.

18. D. Hall and M.K. Wood. Acta Crystallogr. B41, 169 (1985).

19. R.W. Impey, M.L. Klein and I.R. McDonald. J. Chem. Phys. 74, 647 (1981).

20. R.W. Impey, P.A. Madden and I.R. McDonald. Mol. Phys. 46, 513 (1982).

21. P.W. Deutsch, B.N. Hale, R.C. Ward and D.A. Reago. J. Phys. Chem. 87, 4309 (1983).

22. T.A. Weber and F.H. Stillinger. J. Phys. Chem. 87, 4277 (1983).

23. O. Matsuoka, E. Clementi and M. Yoshimine. J. Chem. Phys. 64, 1351 (1976).

24. H.J.C. Berendsen, J.P.M. Postma, W.V. van Gunstern and J. Herman. In Intermolecular Forces. Edited by B. Pullman. Reidel, Dordrecht. 1981.

25. W.L. Jorgensen. J. Chem. Phys. 77, 4156 (1982).

26. W.L. Jorgensen, J. Chandrasekhar, J.D. Madura, R.W. Impey and M.L. Klein. J. Chem. Phys. 79, 926 (1983).

27. M. Grimsditch, A. Rahman and A. Polian. In Proceedings of the IX AIRAPT Conference, Albany. 1983.

28. A. Rahman, F.H. Stillinger and H.L. Lemberg. J. Chem. Phys. 63, 5223 (1975).

29. S. Miyazima, T. Tanaka and A.R. McGurn. Prog. Theor. Phys. 73, 1268 (1985).

30. K.S. Schweizer and F.H. Stillinger. J. Chem. Phys. 80, 1230 (1984).

31. V.E. Schneider and E.E. Tornau. Chem. Phys. 98, 41 (1985).

32. V.G. Vaks and V.I. Zinenko. Solid State Commun. 39, 643 (1981).

33. J.W. Huas and T. Tanaka. Phys. Rev. B16, 2148 (1977).

34. J. Ho-Ting-Hun and J. Oitmaa. Phys. Rev. B20, 3940 (1979).

35. I.A. Ryzhkin. Phys. Stat. Sol. 86, 87 (1984).

36. S.K. Trikha and S.C. Jain. Phys. Stat. Sol. 63, 163 (1981).

37. A.H.A. Penny. Proc. Cambridge Phil. Soc. 44, 423 (1948).

38. T.M. Haridasan and J. Govindarajan. Chem. Phys. Left. 4, 11 (1969).

39. B. Renker and P.V. Blanckenhagen. In Physics of Ice; Proceedings of the International Symposium on Physics of Ice, Munich, Germany. Edited by N. Reihl, B. Bullemer and H. Engelhardt. Plenum Press, New York. 1969. p. 287.

40. L.A. Lliboutry. Traite de Glaciologie. Paris, Masson et Cie. 2, 538 (1964-65).

41. O. Mishima, D.D. Klug and E. Whalley. J. Chem. Phys. 78, 6399 (1983).

42. E. Whalley and G.E. McLaurin. J. Opt. Soc. Am. A 1, 1166 (1984).

43. F.L. Whipple. Astrophys. J. 111, 375 (1950).

44. J. Klinger. Science 209, 271 (1980).

45. H. Patashnick, G. Rupprecht and D.W. Schuerman. Nature 250, 313 (1974).

46. G.J. Consolmagno. J. Phys. Chem. 87, 4204 (1983).

47. P.H. Hepburn. J. Br. Astron. Assoc. 33, 244 (1923).

48. R.N. Clark and P.D. Owensby. Icarus 46, 354 (1981).

49. D. Morrison, D.P. Cruikshank, C.B. Pilcher and G.H. Rieke. Astron. J. 207, 213 (1976).

50. U. Fink, H.P. Larson, T.N. Gautier and R.R. Trefers. Astroph. J. 207, 63 (1976).

51. S.W. Squyres. Geophys. Res. Lett. 7, 593 (1980).

52. G.J. Consolmagno and J.S. Lewis. Icarus 34, 280 (1978).

53. R.T. Reynolds and P.M. Cassen. Geophys. Res. Lett. 6, 121 (1979).

54. E.M. Parmentier and J.W. Head. J. Geophys. Res. 84, 6263 (1979).

55. E.M. Parmentier and J.W. Head. In Proc. 10th Lunar Planet. Sci. Conf. 1979. p. 2403.

56. P.M. Cassen, S.J. Peale and R.T. Reynolds. Geophys. Res. Lett. 7, 987 (1980).

57. P.M. Cassen, S.J. Peale and R.T. Reynolds. In Satellites of Jupiter. Edited by D. Morrison. The University of Arizona, Tuscon. 1982. p. 93.

58. C.F. Yoder. E.O.S. 42, 939 (1981).

59. S.J. Peale, P. Cassen and R.T. Reynolds. Icarus 43, 65 (1980).

60. E.S. Gaffney and D.L. Matson. Icarus 44, 511 (1980).

61. E.S. Gaffney. AGU Spring Meeting. 1986.

62. J.P. Poirier. Nature 299, 683 (1982).

63. J. Klinger. J. Phys. Chem. 87, 4209 (1983).

64. B. Kamb. Science 150, 205 (1965).

65. B. Kamb and A. Prakash. Acta Crystallogr. 24, 1317 (1968).

66. P.V. Hobbs. Ice Physics. Oxford University Press, London. 1974.

67. F. Rinne. Math.-Phys. Kl 69, 57 (1917).

68. A. St.John. Proc. Natn. Acad. Sci. U.S.A. 4, 193 (1918).

69. D.M. Dennison. Phys. Rev. 17, 20 (1921).

70. K. Kume. J. Phys. Soc. Japan 15, 1493 (1960).

71. K. Kume and R. Hoshino. J. Phys. Soc. Japan 16, 290 (1961).

72. N.N. Korst, V.A. Savel'ev and N.D. Sokolov. Soviet Phys. Sol. St. 6, 965 (1964).

73. D.E. Barnaal and I.J. Lowe. J. Chem. Phys. 46, 4800 (1967).

74. S.W. Rabideau and A.B. Denison. J. Chem. Phys. 49, 4660 (1968).

75. G. Siegle and M. Weithase. In Physics of Ice; Proceedings of the International Symposium on Physics of Ice, Munich, Germany. Edited by N. Riehl, B. Bullemer and H. Engelhardt. Plenum Press, New York. 1969. p. 571.

76. E.F. Burton and W.F. Oliver. Proc. R. Soc. A153, 166 (1935).

77. H. Konig. Z. Kristallogr. 105, 279 (1943).

78. G. Tammann. Annln. Phys. 2, 1 (1900).

79. P.W. Bridgman. Proc. Am. Acad. Arts Sci. 47, 441 (1912).

80. B. Kamb and S.K. Datta. Nature 187, 140 (1960).

81. B. Kamb. Acta Crystallogr. 17, 1437 (1964).

82. J.E. Bertie, L.D. Calvert and E. Whalley. J. Chem. Phys. 38, 840 (1963).

83. B. Kamb and C. Knobler. Acta Crystallogr. 22, 706 (1967).

84. P.W. Bridgman. J. Chem. Phys. 3, 597 (1935).

85. H. Engelhardt and B. Kamb. J. Chem. Phys. 75, 5887 (1981).

86. P.W. Bridgman. J. Chem. Phys. 5, 964 (1937).

87. B. Kamb and B.L. Davis. Proc. Natn. Acad. Sci. U.S.A. 52, 1433 (1964).

88. E. Whalley, J.B.R. Heath and D.W. Davidson. J. Chem. Phys. 45, 3976 (1966).

89. E. Whalley, J.B.R. Heath and D.W. Davidson. J. Chem. Phys. 48, 2362 (1968).

90. A. Polian and M. Grimsditch. Phys. Rev. Lett. 52, 1312 (1984).

91. K.R. Hirsch and W.B. Holzapfel. Phys. Lett. A 101, 142 (1984).

92. W.B. Holzapfel. J. Chem. Phys. 56, 712 (1972).

93a. H. Suga. Solid State Phys. 20, 81 (1985).

93b. A.J. Leadbetter, R.C. Ward, J.W. Clark, P.A. Tucker, T. Matsuo and H. Suga. J. Chem. Phys. 82, 424 (1985).

94. M.J.P. Musgrave. Crystal Acoustics. Holden-Day, San Francisco, 1970.

95. P.H. Gammon. M.Sc. Thesis. Memorial University of Newfoundland. 1978. (Unpublished).

96. N.E. Dorsey. Properties of Ordinary Water-substance. Reinhold Publishing Corporation, New York. 1940.

97. A.H.A. Penny. Proc. Cambridge Phil. Soc. 44, 423 (1948).

98. T.D. Northwood. Can. J. Res., Sec. A, 25, 88 (1947).

99. W. Voigt. Lehrbuch der Kristallphysik. Teubner, Leipzig. 1910.

100. F. Jona and P. Scherrer. Helv. Phys. Acta 25, 35 (1952).

101. R.E. Green and L. MacKinnon. J. Acous. Soc. Am. 28, 1292 (1956).

102. R. Bass, D. Rossberg and G. Ziegler. Z. Phys. 149, 199 (1957).

103. V.V. Bogorodskii. Sov. Phys. Acous. 10, 124 (1964).

104. B. Brockamp and H. Querfurth. Z. Polarforschung 5, 253 (1964).

105. A. Zarembovitch and A. Kahane. Compt. Rend. Hebd. Seance. Acad. Sci. Paris 258, 2529 (1964).

106. T.M. Proctor. J. Acous. Soc. Am. 39, 972 (1966).

107. G. Dantl. Thesis (Dr. rer. nat.) Technischen Hochschule Stuttgart. 1967.

108. G. Dantl. In Physics of Ice: Proceedings of the International Symposium on Physics of Ice, Munich, Germany. Edited by N. Riehl, B. Bullemer and H. Engelhardt. Plenum Press, New York. 1969. p. 223.

109. G. Dantl. Phys. Kondens. Materie 7, 390 (1968).

110. U. Mitzdorf and D. Helmreich. J. Acous. Soc. Am. 49, 723 (1971).

111. A. Ermoleiff. Solid State Commun. 17, 1013 (1975).

112. P.H. Gammon, H. Kiefte and M.J. Clouter. J. Glaciol. 25, 159 (1980).

113. P.H. Gammon, H. Kiefte and M.J. Clouter. J. Phys. Chem. 87, 4025 (1983).

114. B. Brockamp and H. Ruter. Z. Geophys. 35, 277 (1969).

115. A. Reuss. Z. Angew. Math. Mech. 9, 55 (1929).

116. A. Polian and M. Grimsditch. Phys. Rev. B 27, 6409 (1983).

117. P.W. Bridgman. Proc. Am. Acad. Arts Sci. 74, 399 (1942).

118. R.G. Munro, S. Block, F.A. Mauer and G. Piermarini. J. Appl. Phys. 53, 6174 (1982).

119. G.H. Shaw. J. Chem. Phys. 84, 5862 (1986).

120. G.E. Durand and A.S. Pine. IEEE J. Quantum Electronics. QE4, 523 (1968).

121. J.R. Sandercock. RCA Review 36, 89 (1975).

122. B.P. Stoicheff. In Fundamental and Applied Laser Physics. Proceedings of the Esfahan Symposium. Edited by M.S. Feld, A. Javan and N.A. Kurnit. John Wiley and Sons, Inc., New York. 1973. p. 573.

123. B.P. Stoicheff. In Rare Gas Solids. Vol.2. Edited by M.L. Klein and J.A. Venables. Academic Press, New York. 1977. p. 979.

124. H. Kiefte and M.J. Clouter. J. Chem. Phys. 62, 4780 (1975).

125. H. Kiefte and M.J. Clouter. J. Chem. Phys. 64, 1816 (1976).

126. P.H. Gammon. Ph.D. Thesis. Memorial University of Newfoundland. 1981. (Unpublished).

127. P.H. Gammon, H. Kiefte and M.J. Clouter. J. Chem. Phys. 70, 810 (1978).

128. S.F. Ahmad, H. Kiefte and M.J. Clouter. J. Chem. Phys. 69, 5468 (1978).

129. F.A. Jenkins and H.E. White. Fundamentals of Optics. McGraw-Hill, New York. 1957.

130. G.B. Benedek and K. Fritsch. Phys. Rev. 149, 647 (1966).

131. T.R. Butkovich. J. Appl. Phys. 30, 350 (1959).

132. D. Landheer. Ph.D. Thesis. University of Toronto. 1974. (Unpublished).

133. H.B. Huntington. The Elastic Constants of Crystals. Academic Press, New York. 1958.

134. J.F. Nye. Physical Properties of Crystals. Clarendon Press, Oxford. 1957.

135. W.F. Giauque and J.W. Stout. J. Am. Chem. Soc. 58, 1144 (1936).

136. M. Born. Proc. Cambridge Phil. Soc. 36, 160 (1940).

137. R.M. Misra. Proc. Cambridge Phil. Soc. 36, 173 (1940).

138. L.D. Landau and E.M. Lifshitz. Theory of Elasticity. Pergamon Press, London. 1959.

139. L.E. Malvern. Introduction to the Mechanics of a Continuous Medium. Prentice-Hall Inc., Englewood Cliffs, N.J. 1969.

140. P.W. Bridgman. Proc. Am. Acad. Arts Sci. 74, 399 (1942).

141. G.E. Linnert. Welding Metallurgy. Vol.1. 3rd Edition. American Welding Society, New York. 1965.

142. P.W. Bridgman. Proc. Am. Acad. Arts Sci. 73, 74 (1938).

143. K. Yamamoto. Jpn. J. Appl. Phys. 21, 803 (1982).

144. K. Yamamoto. Jpn. J. Appl. Phys. 21, 567 (1982).

145. K. Yamamoto. Jpn. J. Appl. Phys. 19, 1841 (1980).

146. R.G. Ross, P. Andersson and G. Backstrom. High Temp. High Press. 9, 87 (1977).

147. B. Minceva-Sukarova, W.F. Sherman and G.R. Wilkinson. J. Phys. C: Solid State Phys. 17, 5833 (1984).

148. F. Birch. J. Geophys. Res. 65, 1083 (1960).

149. F. Birch. J. Geophys. Res. 66, 2199 (1961).

150. B. Kamb. In Physics and Chemistry of Ice. Edited by E. Whalley, S.J. Jones and L.W. Gold. Royal Society of Canada, Ottawa. 1973. p. 28.

151. S.W. Peterson and H.A. Levy. Acta Crystallogr. 10, 70 (1957).

152. K. Shimaoka. J. Phil. Soc. Japan 15, 106 (1960).

153. B. Kamb, W.C. Hamilton, S.J. La Placa and A. Prakash. J. Chem. Phys. 55, 1934 (1971).

154. G.P. Arnold, R.G. Wenzel, S.W. Rabideau, N.G. Nearson and A.L. Bowman. J. Chem. Phys. 55, 589 (1971).

155. W.C. Hamilton, B. Kamb, S.J. La Placa and A. Prakash. In Physics of Ice: Proceedings of the International Symposium on Physics of Ice, Munich, Germany. Edited by N. Riehl, B. Bullemer and H. Engelhardt. Plenum Press, New York. 1969.

156. E. Weir, S. Block and G. Piermarini. J. Res. Natn. Bur. Stand. 69C, 275 (1965).

157. S.J. La Placa, W.C. Hamilton, B. Kamb and A. Prakash. J. Chem. Phys. 58, 576 (1973).